

RD-R170 670

OBSERVING THE SYNOPTIC STRUCTURE OF TWO MOISTURE BURSTS 1/2

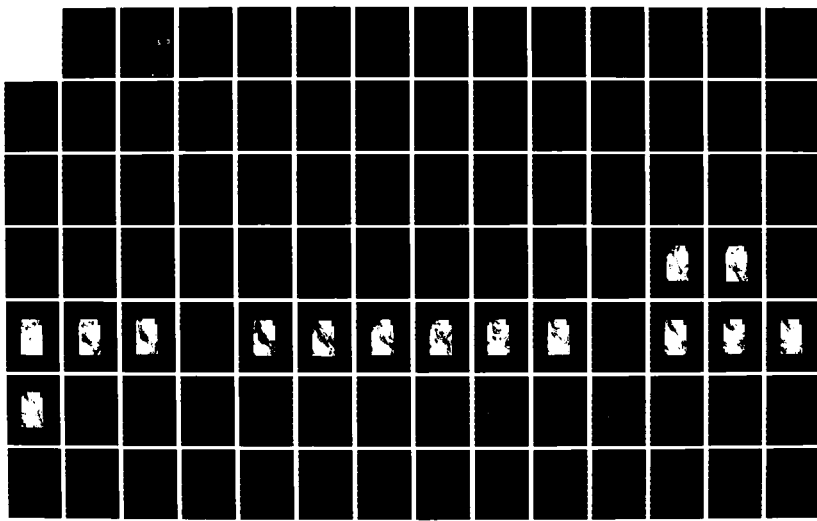
(U) AIR FORCE INST OF TECH WRIGHT-PATTERSON AFB OH

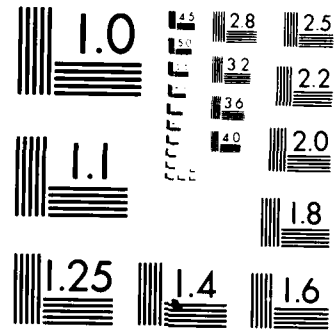
J R SCHAEFER DEC 85 AFIT/CI/NR-86-70T

UNCLASSIFIED

FFG 4/2

ML





MICROCOPY RESOLUTION TEST CHART
NATIONAL BUREAU OF STANDARDS 1963 A

AD-A170 670

FILE COPY

| REPORT DOCUMENTATION PAGE | | | READ INSTRUCTIONS BEFORE COMPLETING FORM |
|--|-----------------------|---|---|
| 1. REPORT NUMBER AFIT/CI/NR 86-70T | 2. GOVT ACCESSION NO. | 3. RECIPIENT'S CATALOG NUMBER | |
| 4. TITLE (and Subtitle) Observing The Synoptic Structure Of Two Moisture Bursts | | 5. TYPE OF REPORT & PERIOD COVERED THESIS/DISSERTATION | |
| | | 6. PERFORMING ORG. REPORT NUMBER | |
| 7. AUTHOR(s) James Royal Schaefer | | 8. CONTRACT OR GRANT NUMBER(s) | |
| 9. PERFORMING ORGANIZATION NAME AND ADDRESS AFIT STUDENT AT: Texas A&M University | | 10. PROGRAM ELEMENT, PROJECT, TASK AREA & WORK UNIT NUMBERS | |
| 11. CONTROLLING OFFICE NAME AND ADDRESS AFIT/NR WPAFB OH 45433-6583 | | 12. REPORT DATE 1985 | 13. NUMBER OF PAGES 145 |
| 14. MONITORING AGENCY NAME & ADDRESS, if different from Controlling Office) | | 15. SECURITY CLASS. (of this report) UNCLAS | 15a. DECLASSIFICATION/DOWNGRADING SCHEDULE |
| 16. DISTRIBUTION STATEMENT (of this Report) APPROVED FOR PUBLIC RELEASE; DISTRIBUTION UNLIMITED | | | |
| 17. DISTRIBUTION STATEMENT (of the abstract entered in Block 20, if different from Report) | | | |
| 18. SUPPLEMENTARY NOTES APPROVED FOR PUBLIC RELEASE: IAW AFR 190-1 <i>Lynn Wolaver</i> LYNN E. WOLAYER 6 AUG 86 Dean for Research and Professional Development AFIT/NR | | | |
| 19. KEY WORDS (Continue on reverse side if necessary and identify by block number) | | | |
| 20. ABSTRACT (Continue on reverse side if necessary and identify by block number) ATTACHED. | | | |

OBSERVING THE SYNOPTIC STRUCTURE OF TWO MOISTURE BURSTS

A Thesis

by

JAMES ROYAL SCHAEFER

Submitted to the Graduate College of
Texas A&M University
in partial fulfillment of the requirements for the degree of

MASTER OF SCIENCE

December 1985

Major Subject: Meteorology

| | |
|---------------------|-------------------------------------|
| Accession For | |
| NTIS GRA&I | <input checked="" type="checkbox"/> |
| DTIC TAB | <input type="checkbox"/> |
| Unannounced | <input type="checkbox"/> |
| Justification | |
| By _____ | |
| Distribution/ _____ | |
| Availability Codes | |
| Dist | Avail and/or Special |
| A-1 | |



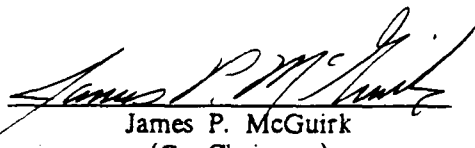
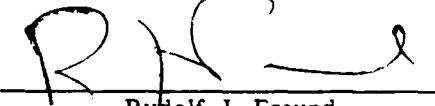
OBSERVING THE SYNOPTIC STRUCTURE OF TWO MOISTURE BURSTS

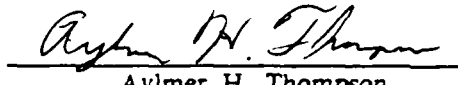
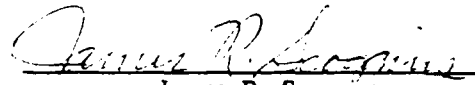
A Thesis

by

JAMES ROYAL SCHAEFER

Approved as to style and content by:


James P. McGuirk
(Co-Chairman)

Rudolf J. Freund
(Member)


Aylmer H. Thompson
(Co-Chairman)

James R. Scoggins
(Head of Department)

December 1985

ABSTRACT

Observing the Synoptic Structure of Two Moisture Bursts. (December 1985)

James Royal Schaefer, B.S., University of Wisconsin, Eau Claire;
B.S., University of Utah

Co-Chairmen of Advisory Committee: Dr. James P. McGuirk
Dr. Aylmer H. Thompson

The moisture burst is characterized by large amounts of cloudiness emanating from tropical regions and often affecting middle-latitude regions. Due to data scarcity, the study of moisture bursts near their origin is difficult. Supplementary data available during the First GARP Global Experiment make such a study feasible.

Through the use of in situ observations and computer-generated model analyses, this thesis presents results of a synoptic case study of two moisture bursts. Satellite-derived data are shown to be useful in this region, although lack of certain satellite radiance channels during the time period precludes their use. The FGGE IIIb model analyses are first proven to be reliable by comparison with satellite observations and are then used extensively.

A significant upper-level trough, with strong subtropical jet stream winds, existed during the origin periods of both bursts. A large northward meridional component to the subtropical jet stream was found on the downstream side of the troughs. There was a low-level easterly wave trough near the origin of the first burst. Associated with at least the first moisture burst, evidence was found suggesting an upper-level cold front near an area of rapid development of the burst.

Most importantly, it was found that these two moisture bursts were not homogeneous masses of clouds, but were composed of several separate cloud masses which combined to form the moisture burst. These cloud masses include elements associated with the intertropical convergence, with a southward moving frontal disturbance, and with convective development between the first two. Additional evidence suggests that the moisture burst is not merely an extension of ITCZ activity into the subtropics. Therefore, it is proposed that the moisture burst is due not to any one, or even two, major features, but is a combination of a number of interrelated elements.

V

ACKNOWLEDGEMENTS

I acknowledge my committee for their excellent support and gentle shoves in the right direction. I thank Dr. James P. McGuirk for his inspirational ideas and especially his humor that was always there when most needed. I would also like to thank Dr. Aylmer H. Thompson for his expert suggestions in the field of synoptic meteorology and his attention to detail. I sincerely thank them for their professionalism and patience.

Special thanks are extended to my wife Karen who had to survive not only the low points of my work, but also the high points. Her support helped to smooth the lows and highs.

I also wish to thank the United States Air Force, Air Force Institute of Technology, and The National Aeronautics and Space Administration for allowing the opportunity to conduct this research.

TABLE OF CONTENTS

| | Page |
|---|------|
| ABSTRACT | iii |
| ACKNOWLEDGEMENTS | v |
| TABLE OF CONTENTS | vi |
| LIST OF FIGURES | viii |
| CHAPTER I INTRODUCTION | 1 |
| CHAPTER II REVIEW OF LITERATURE | 3 |
| a. Data analysis | 3 |
| b. Synoptic phenomena | 5 |
| CHAPTER III DATA EVALUATION | 7 |
| a. Data products available | 7 |
| b. SATEM cross sections | 8 |
| c. Statistical analysis of FGGE IIIb data | 16 |
| 1) Moisture variability | 17 |
| 2) Thermal variability | 27 |
| CHAPTER IV SYNOPTIC ANALYSIS | 37 |
| a. Satellite-derived imagery | 37 |
| b. Wind analyses | 57 |
| c. Temperature changes | 74 |
| d. FGGE IIIb relative humidity depictions | 91 |
| e. Hawaii time sections | 123 |
| CHAPTER V SYNTHESIS AND INTERPRETATION | 130 |
| CHAPTER VI CONCLUSIONS | 140 |
| REFERENCES | 142 |

Table of Contents (Continued)

| | Page |
|----------------|------|
| VITA | 145 |

LIST OF FIGURES

| FIGURE | Page |
|--|------|
| 1 SATEM cross section of temperature distribution for 0000 GMT 21 January 1979. | 10 |
| 2 As in Fig. 1 except for 0000 GMT 23 January 1979. | 11 |
| 3 As in Fig. 1 except for 0000 GMT 24 January 1979. | 12 |
| 4 As in Fig. 1 except for 0000 GMT 25 January 1979. | 13 |
| 5 As in Fig. 1 except for 0000 GMT 26 January 1979. | 14 |
| 6 Grid point temporal standard deviation for FGGE IIIb 1000 mb relative humidity. | 18 |
| 7 As in Fig. 6 except for 850 mb. | 19 |
| 8 As in Fig. 6 except for 700 mb. | 21 |
| 9 As in Fig. 6 except for 500 mb. | 22 |
| 10 As in Fig. 6 except for satellite channel 12 (a moisture channel with the weighting function peaking near the 500 mb surface). | 23 |
| 11 Grid point cross-correlation coefficients of FGGE IIIb 700 mb RH vs. satellite channel 11 (a moisture channel with the weighting function peaking near the 700 mb surface). | 25 |
| 12 As in Fig. 11 except for 500 mb RH vs. satellite channel 12 (a moisture channel with the weighting function peaking near the 500 mb level). | 26 |
| 13 Grid point temporal standard deviations for FGGE IIb 1000 mb temperatures. | 28 |
| 14 As in Fig. 13 except for 850 mb. | 29 |
| 15 As in Fig. 13 except for 700 mb. | 30 |
| 16 As in Fig. 13 except for 400 mb. | 32 |
| 17 As in Fig. 13 except for 300 mb. | 33 |

List of Figures (Continued)

| FIGURE | Page |
|--|------|
| 18 As in Fig. 13 except for satellite channel 15 (a temperature channel with the weighting function peaking near the 700 mb surface). | 34 |
| 19 Grid point cross-correlation coefficients of FGGE IIIb 700 mb temperature vs. satellite channel 15 (a temperature channel with the weighting function peaking near the 700 mb surface). | 36 |
| 20 Unenhanced GOES West IR satellite photograph for 0015 GMT 21 January 1979. | 39 |
| 21 As in Fig. 20 except for 1215 GMT 21 January 1979. | 40 |
| 22 Visual GOES West satellite photograph for 1745 GMT 21 January 1979. | 42 |
| 23 As in Fig. 20 except for 0015 GMT 22 January 1979. | 43 |
| 24 As in Fig. 20 except for 1215 GMT 22 January 1979. | 44 |
| 25 As in Fig. 20 except for 0015 GMT 23 January 1979. | 46 |
| 26 As in Fig. 20 except for 1215 GMT 23 January 1979. | 47 |
| 27 As in Fig. 20 except for 0015 GMT 24 January 1979. | 48 |
| 28 As in Fig. 20 except for 1215 GMT 24 January 1979. | 49 |
| 29 As in Fig. 20 except for 0015 GMT 25 January 1979. | 50 |
| 30 As in Fig. 20 except for 1215 GMT 25 January 1979. | 51 |
| 31 As in Fig. 20 except for 0015 GMT 27 January 1979. | 53 |
| 32 As in Fig. 20 except for 1215 GMT 27 January 1979. | 54 |
| 33 As in Fig. 20 except for 0015 GMT 28 January 1979. | 55 |
| 34 As in Fig. 20 except for 1215 GMT 28 January 1979. | 56 |
| 35 Keys for next 11 figures. | 58 |
| 36 300 mb FGGE IIIb streamline (solid lines) and isotach (dashed lines in ms^{-1}) fields for 0000 GMT 21 January 1979. | 60 |
| 37 As in Fig. 36 except for 0000 GMT 22 January 1979. | 61 |
| 38 As in Fig. 36 except for 0000 GMT 23 January 1979. | 63 |

List of Figures (Continued)

| FIGURE | Page |
|--|------|
| 39 As in Fig. 36 except for 0000 GMT 24 January 1979. | 64 |
| 40 As in Fig. 36 except for 0000 GMT 25 January 1979. | 65 |
| 41 As in Fig. 36 except for 0000 GMT 26 January 1979. | 66 |
| 42 As in Fig. 36 except for 850 mb at 0000 GMT 21 January 1979. | 68 |
| 43 As in Fig. 36 except for 850 mb at 0000 GMT 22 January 1979. | 69 |
| 44 As in Fig. 36 except for 850 mb at 0000 GMT 23 January 1979. | 70 |
| 45 As in Fig. 36 except for 850 mb at 0000 GMT 24 January 1979. | 72 |
| 46 As in Fig. 36 except for 850 mb at 0000 GMT 26 January 1979. | 73 |
| 47 FGGE IIIb 24 h temperature changes at 1000 mb for the period ending 1200 GMT 21 January 1979. | 75 |
| 48 As in Fig. 47 except for the period ending 0000 GMT 22 January 1979. | 76 |
| 49 As in Fig. 47 except for the period ending 1200 GMT 22 January 1979. | 77 |
| 50 As in Fig. 47 except for the period ending 1200 GMT 23 January 1979. | 79 |
| 51 As in Fig. 47 except for the period ending 1200 GMT 24 January 1979. | 80 |
| 52 FGGE IIIb 12 h temperature changes at 300 mb for the period ending 0000 GMT 21 January 1979. | 81 |
| 53 As in Fig. 52 except for the period ending 1200 GMT 21 January 1979. | 82 |
| 54 As in Fig. 52 except for the period ending 0000 GMT 22 January 1979. | 84 |
| 55 As in Fig. 52 except for the period ending 1200 GMT 22 January 1979. | 85 |
| 56 As in Fig. 52 except for the period ending 0000 GMT 23 January 1979. | 86 |

List of Figures (Continued)

| FIGURE | Page |
|--|------|
| 57 As in Fig. 52 except for the period ending 0000 GMT 24 January 1979. | 87 |
| 58 As in Fig. 52 except for the period ending 1200 GMT 24 January 1979. | 88 |
| 59 As in Fig. 52 except for the period ending 0000 GMT 25 January 1979. | 89 |
| 60 As in Fig. 52 except for the period ending 1200 GMT 25 January 1979. | 90 |
| 61a Vertical cross section of FGGE IIIb relative humidity for 0000 GMT 21 January 1979. | 93 |
| 61b Vertical cross sections of FGGE IIIb relative humidity perpendicular to the main track for 0000 GMT 21 January 1979. | 94 |
| 62a As in Fig. 61a except for 1200 GMT 21 January 1979. | 95 |
| 62b As in Fig. 61b except for 1200 GMT 21 January 1979. | 96 |
| 63a As in Fig. 61a except for 0000 GMT 22 January 1979. | 98 |
| 63b As in Fig. 61b except for 0000 GMT 22 January 1979. | 99 |
| 64a As in Fig. 61a except for 1200 GMT 22 January 1979. | 100 |
| 64b As in Fig. 61b except for 1200 GMT 22 January 1979. | 101 |
| 65a As in Fig. 61a except for 0000 GMT 23 January 1979. | 102 |
| 65b As in Fig. 61b except for 0000 GMT 23 January 1979. | 103 |
| 66a As in Fig. 61a except for 1200 GMT 23 January 1979. | 104 |
| 66b As in Fig. 61b except for 1200 GMT 23 January 1979. | 105 |
| 67a As in Fig. 61a except for 1200 GMT 24 January 1979. | 107 |
| 67b As in Fig. 61b except for 1200 GMT 24 January 1979. | 108 |
| 68a As in Fig. 61a except for 0000 GMT 25 January 1979. | 109 |
| 68b As in Fig. 61b except for 0000 GMT 25 January 1979. | 110 |
| 69a As in Fig. 61a except for 0000 GMT 26 January 1979. | 111 |

List of Figures (Continued)

| FIGURE | Page |
|---|------|
| 69b As in Fig. 61b except for 0000 GMT 26 January 1979. | 112 |
| 70a As in Fig. 61a except for 1200 GMT 26 January 1979. | 113 |
| 70b As in Fig. 61b except for 1200 GMT 26 January 1979. | 114 |
| 71a As in Fig. 61a except for 0000 GMT 27 January 1979. | 115 |
| 71b As in Fig. 61b except for 0000 GMT 27 January 1979. | 116 |
| 72a As in Fig. 61a except for 1200 GMT 27 January 1979. | 118 |
| 72b As in Fig. 61b except for 1200 GMT 27 January 1979. | 119 |
| 73a As in Fig. 61a except for 0000 GMT 28 January 1979. | 120 |
| 73b As in Fig. 61b except for 0000 GMT 28 January 1979. | 121 |
| 74 Vertical time section for Hilo, Hawaii for the time period 0000 GMT 20 January to 0000 GMT 24 January 1979. | 124 |
| 75 As in Fig. 74 except for Lihue, Hawaii. | 125 |
| 76 Vertical time section for Hilo, Hawaii for 0000 GMT 20 January to 0000 GMT 24 January 1979. | 126 |
| 77 As in Fig. 76 except for Lihue, Hawaii. | 127 |
| 78 Schematic depictions for upper and lower levels for 0000 GMT 21 January 1979. | 131 |
| 79 As in Fig. 78 except for 1200 GMT 21 January 1979. | 133 |
| 80 As in Fig. 78 except for 0000 GMT 22 January 1979. | 134 |
| 81 As in Fig. 78 except for 1200 GMT 22 January 1979. | 135 |
| 82 As in Fig. 78 except for 0000 GMT 23 January 1979. | 136 |

CHAPTER I

INTRODUCTION

The pattern of large bands of clouds moving out of the equatorial regions and often into the mid-latitudes has been studied for a number of years. It has been called by several different names, but in this work the phenomenon will be referred to as a "moisture burst."

An objective definition of a moisture burst is that of McGuirk *et al.* (1984). The moisture burst is characterized by a continuous band of upper and mid-level clouds at least 2000 km long originating from a source equatorward of 15°N and extending poleward of 15°N. Using this definition, they documented 128 moisture bursts between 160°E and 90°W during the two six-month northern hemisphere cold seasons of 1977-78 and 1981-82. The frequency of occurrence of moisture bursts as a function of longitude is approximately constant west of 120°W and decreases abruptly east of this longitude. In an average month about 11 bursts occur, with at least one burst active about 75% of the time in the Pacific. The Pacific moisture burst often extends over North America and commonly is associated with synoptic and meso-scale disturbances affecting the United States.

The major problem with studying the tropical regions, where moisture bursts originate and grow, is the scarcity of data. This problem was partially solved during the FGGE [First GARP (Global Atmospheric Research Program) Global Experiment] SOP 1 (Special Observing Period 1) when additional observing ships, aircraft dropsonde flights, and other special observations were recorded. This increased data

The style used is that of the Monthly Weather Review.

coverage allowed not only a more detailed analysis than previously possible, but also a means of cross checking the FGGE model analyses.

The major goal of this study is to develop a better synoptic understanding of a moisture burst. The understanding is based on a case study of two moisture bursts which occurred in January 1979. The first moisture burst satisfied the origin definition by 0300 GMT on 21 January 1979. The origin point was at approximately $7^{\circ}\text{N}/155^{\circ}\text{W}$, and during its lifetime the burst extended all the way to the Americas. It continued evolving until about 0000 GMT on the 25th, when it was terminated as a moisture burst due to a break in the continuous clouds south of 15°N . The second burst originated also at about 0000 GMT on the 25th, with the first poleward progression of clouds from a source region at approximately $7^{\circ}\text{N}/144^{\circ}\text{W}$. This burst terminated at around 1200 GMT on 28 January 1979.

A survey of past synoptic work on related tropical events is used as a starting point for the synoptic study and is presented in Chapter 2. Chapter 3 discusses the applicability of the various data sources that are available through statistical interpretation of various data sets and comparisons with other data sources. The synoptic interpretation sections in Chapter 4 are: satellite interpretation, wind analyses, temperature changes, relative humidity (RH) depictions, and radiosonde time sections. Chapter 5 combines the features and ideas presented in the individual synoptic sections to develop a synoptic overview of the two moisture bursts using schematic diagrams.

The final chapter summarizes findings and lists areas still requiring more study on the nature of these two moisture bursts.

CHAPTER II

REVIEW OF LITERATURE

a. Data analysis

The main limitation in any synoptic study of tropical areas has been the limited amount of reliable data. This limit on observational data means that heavy reliance on computer generated analyses will be helpful for a synoptic study in the tropics. Much work has been done, particularly by the European Center for Medium Range Weather Forecasting (ECMWF), in examining the limitations of computer-generated analyses.

Hollingsworth *et al.* (1985) described the data assimilation system used to produce the FGGE IIIb/ECMWF analyses as an intermittent data assimilation system using a multivariate optimum interpolation analysis and a high resolution model. The ECMWF model produces a forecast which is used as a background field for subsequent analysis. Data are assimilated every six hours and are used to correct and adjust the first-guess forecast field.

Julian (1980) discussed problems in the wind fields related to divergence estimation methods. He pointed out that tropical wind fields appear nearly non-divergent in the analysis due to the use of non-divergent structure functions in the interpolation scheme and to the diabatic origin of most tropical vertical motion. Furthermore, the use of satellite cloud-drift winds in data sparse areas biases the analyses toward areas of strong ascending motion, since these areas possess the most clouds. In a more recent paper, Julian (1984) used areas of divergence as inferred from satellite radiation observations as an input to a wind analysis that he claims is superior to the current ECMWF analysis.

In a study comparing ECMWF analyses with those from the British Meteorological Office, Lorenc and Swinbank (1984) determined that the ECMWF/FGGE IIIb data were inaccurate for statistical studies. They attributed these errors to the smoothing effect of the vertical interpolations in the system, the lack of an adequate diurnal cycle in the model, and the lack of adequate boundary layer resolution in the standard pressure levels used. Using a January 1979 case study for their comparison, they found the height variances in the FGGE IIIb analyses were too small because of damping of tropical activity by the initialization.

The ECMWF has also reported problems even with the ingestion of raw data into the analysis cycle. Hollingsworth *et al.* (1985) pointed out that the ECMWF model did not always directly use satellite high-level cloud-drift winds, but recalculated them using reported temperatures, a definite problem in tropical areas where the thermal wind equation is not an accurate approximation to the actual wind shear.

Due to a coding error, FGGE IIIb analyses contain no moisture input from RAOBS (RAdio OBServations) (R. D. Rosen of AER in Cambridge, MA). The FGGE IIIb analyses also deleted TIROS-N (Television Infrared Observing Satellite) TOVS (Operational Vertical Sounder) moisture observations in the tropics (R. Williams of World Data Center Asheville, NC). Therefore the FGGE IIIb analyses are expected to be weak in handling moisture. This deletion can affect all variables in the analyses.

Several researchers have used these FGGE IIIb analyses to develop synoptic studies of the tropical Pacific. For example, Vincent (1982) used the FGGE IIIb data and also computed several other parameters such as vertical motion and vorticity to study circulation features over the South Pacific during FGGE SOP 1. Huang and Vincent (1983) also used similar parameters to study changes in circulation features over the South Pacific during FGGE SOP 1.

b. Synoptic phenomena

Fujita *et al.* (1969) examined the distribution of the cloud structure in the InterTropical Convergence Zone (ITCZ) and found that cross-equatorial flow and equatorial anticyclones act in concert to form what they called "burst bands." They found that as an equatorial anticyclone forces air to flow across the equator, the reversed Coriolis force displaces the ITCZ band northward as the flow recurves. This northward movement allows an interaction stage with a mid-latitude system such as a cold front. These burst bands may be related to moisture bursts in the meso-scale period of origin.

Anderson and Oliver (1970) used pictures from the earth synchronous satellite ATS-1 (Applications Technology Satellite) to show also the relationship of the upper-level trough to what they called cloud surges. They also used these same satellite pictures to show that a low-level easterly wave is related to the upper-level trough and, therefore, to the cloud surge.

Thepenier and Cruette (1981) speculated that the Atlantic moisture bursts originate as blow-off from cumulonimbus clusters of the ITCZ and are related to the location of upper-level troughs. The band then is carried first by the subtropical jet stream, and then the polar jet stream. The majority of the study by Thepenier and Cruette then deals with the interaction of the burst and mid-latitude disturbances.

Kinenmonth (1981) studied southern hemisphere moisture bursts in relation to rainfall rates in Australia. Davis (1981) using Meteosat to study general circulation, also looked at the tropical-extratropical interaction. These studies showed that moisture bursts exist at many longitudes, and that they may affect the weather in mid-latitudes.

McGuirk and Thompson (1984) examined temperature variation along the west coast of North America as two moisture bursts moved over specific radiosonde stations. They also looked at satellite-derived temperatures and winds over the region of moisture burst origin in the tropical Pacific area. They found a relationship between the triggering of moisture bursts and three elements: 1) upper-level troughs in subtropical latitudes, 2) cross-equatorial flow at 200 mb from the southern hemisphere subtropics, and 3) lower tropospheric disturbances that move into the moisture burst origin region.

Of particular importance to the study of moisture bursts was the work of Thompson *et al.* (1984). They showed that it is possible to combine data from the geostationary GOES (Geostationary Operational Environmental Satellite) (in this case GOES West) and the polar orbiting sun-synchronous TIROS-N (especially the TOVS) to make synoptic scale inferences in the data sparse tropics.

CHAPTER III

DATA EVALUATION

a. Data products available

The data for FGGE SOP 1 consist of traditional observations, satellite information, and computer-generated analyses based on these data.

The actual observations for FGGE SOP 1 are labeled FGGE IIb. The data set consists of aircraft dropsondes, ship reports and ship launched radiosondes, surface reports and radiosondes, satellite cloud-drift winds, infrared temperature reconstructions, and satellite-derived RH depictions. Some limitations apply to these data:

- 1) The wind observations from aircraft dropsondes at times had polarity problems with the instruments and are therefore occasionally missing or in error.
- 2) Although the satellite cloud-drift winds are considered to represent certain levels, the clouds tracked are not necessarily at that level. This discrepancy occasionally results in confusion in regions where there is strong vertical shear between the actual cloud level and the assumed represented level. Also the clouds do not necessarily move with the prevailing wind at any given level.
- 3) The specific applicability to this study of SATEMs (SAtellite TEMperatures) is discussed in Section b of this chapter.

The computer-derived analyses are labeled FGGE IIIb. They include height fields, temperature fields, wind fields, and moisture patterns. These data are available on a $1\frac{7}{8}^{\circ}$ by $1\frac{7}{8}^{\circ}$ gridded field. For this study the field was modified to a $3\frac{3}{4}^{\circ}$ by $3\frac{3}{4}^{\circ}$ gridded field. In addition to standard horizontal analyses, a three-dimensional depiction was created whereby the information can be

displayed in a two dimensional array of vertical cross sections. This technique is used for the FGGE IIIb RH field, and is described and interpreted in Section 4d.

The applicability of the FGGE IIIb moisture and temperature fields is discussed in Section 3c.

In addition to the FGGE data sets, other products are used, including visible and infrared (enhanced and unenhanced) satellite imagery, satellite film loops, and NOAA (National Oceanographic and Atmospheric Administration) operational analyses.

Extensive use is made of the various forms of satellite imagery available, especially the film loops. A detailed analysis of the satellite imagery is accomplished in Section 4a.

b. SATEM cross sections

To study the origin areas of the two moisture bursts, alternate sources of data must be investigated. The first to be investigated are SATEM temperature cross sections. The cross sections constructed lie roughly along the west coast of North America. This cross section location was chosen because both bursts cross this area, and there is a reasonable number of radiosonde stations for comparison. A precise correlation between radiosondes and SATEMs was impossible because distances between individual soundings and SATEM locations were sometimes greater than 400 km.

The SATEMs are layer averaged temperature profiles based on TIROS-N satellite data. The cross sections were created by drawing a straight line of approximate best fit between the radiosonde stations and then selecting satellite soundings within approximately 330 km of the line. The location on the cross section was then determined by drawing a line from the SATEM location perpendicular to the section

line. The dates available during the period of interest are 21, and 23 to 26 January 1979. On 22 January satellite data were unavailable. Figs. 1-5 are the analyzed cross sections. The time for all dates is considered 0000 GMT, but the individual SATEMs vary from approximately 2000 GMT to 0000 GMT.

Fig. 1 shows that, on the 21st, below 200 mb there is a general trend toward cooler temperatures to the north. Above 200 mb, the opposite holds true with coolest temperatures to the south. The most notable feature is a rather sharp temperature drop and then rise over the region near 30° , particularly between 600 and 200 mb. Moving northward at the 350 mb level the temperature decreases 4°C and then within 200 km increases 4°C before again decreasing 2°C in about 100 km. Fig. 2 on the 23rd shows an overall pattern similar to that of Fig. 1. The horizontal temperature changes are spread out over a greater linear distance on the 23rd and are located to the south of, and somewhat lower than the similar pattern found on the 21st.

By the 24th (Fig. 3), the region of significant horizontal temperature change is less pronounced, and is largely confined to levels below 400 mb. This region continues moving to the south, suggesting it is a meteorological, rather than instrumental, phenomenon. Fig. 4 shows the region of temperature change continuing to move slowly southward. In the area near $17^{\circ}\text{N}/108^{\circ}\text{W}$ there is a fairly sharp drop in temperatures, especially near the surface.

Fig. 5 shows only one area of abrupt temperature change. Near $25^{\circ}\text{N}/112^{\circ}\text{W}$ the 850 mb temperature changes 4°C in about 200 km. Other than this fluctuation, the gradients are slight, and only show the general pattern similar to all time periods.

The general pattern of the SATEM cross sections agrees with the radiosonde cross sections (not shown). Both reflected the warmer temperatures to the south below

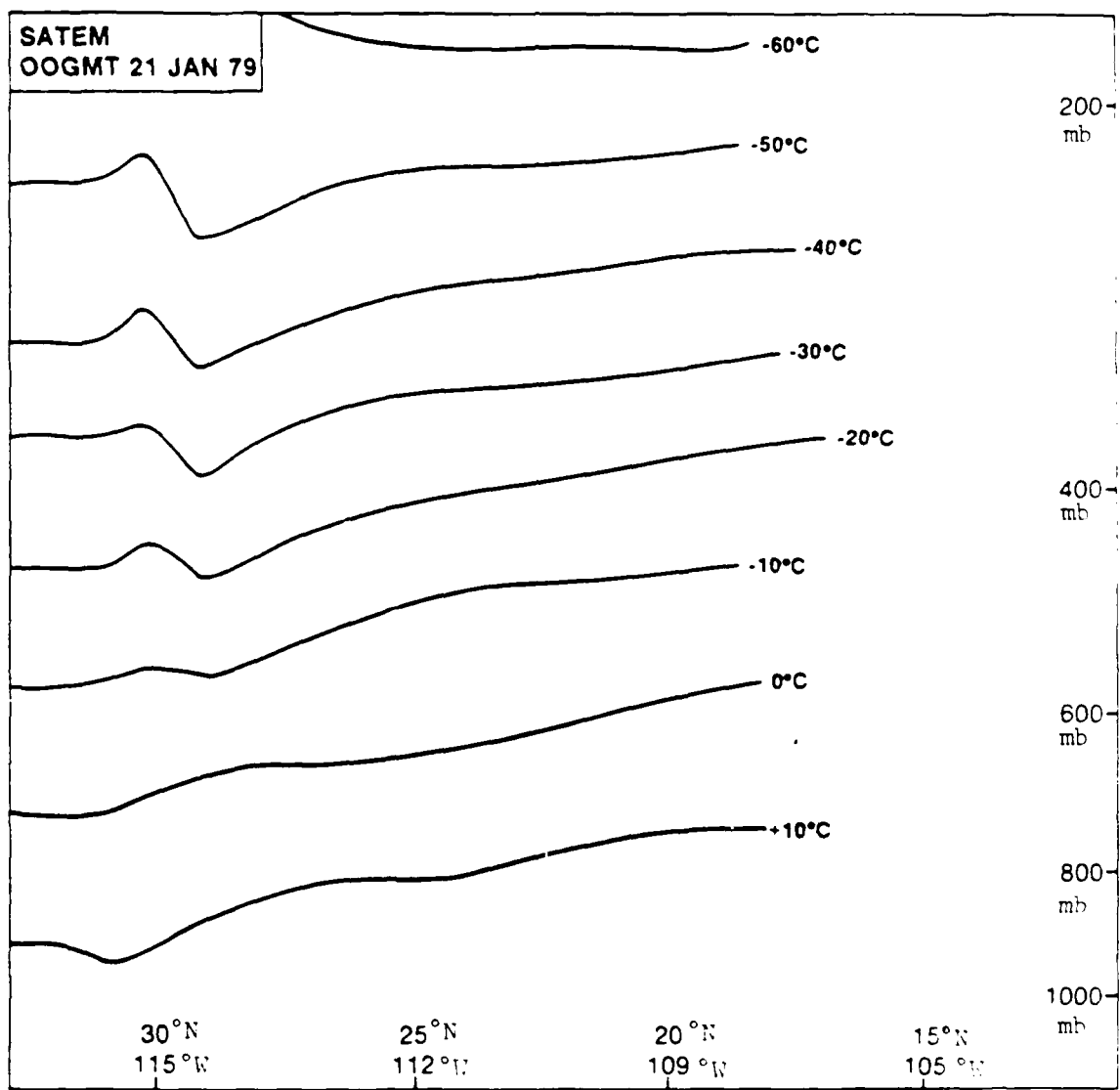


Fig. 1. SATEM cross section of temperature distribution for 0000 GMT 21 January 1979.

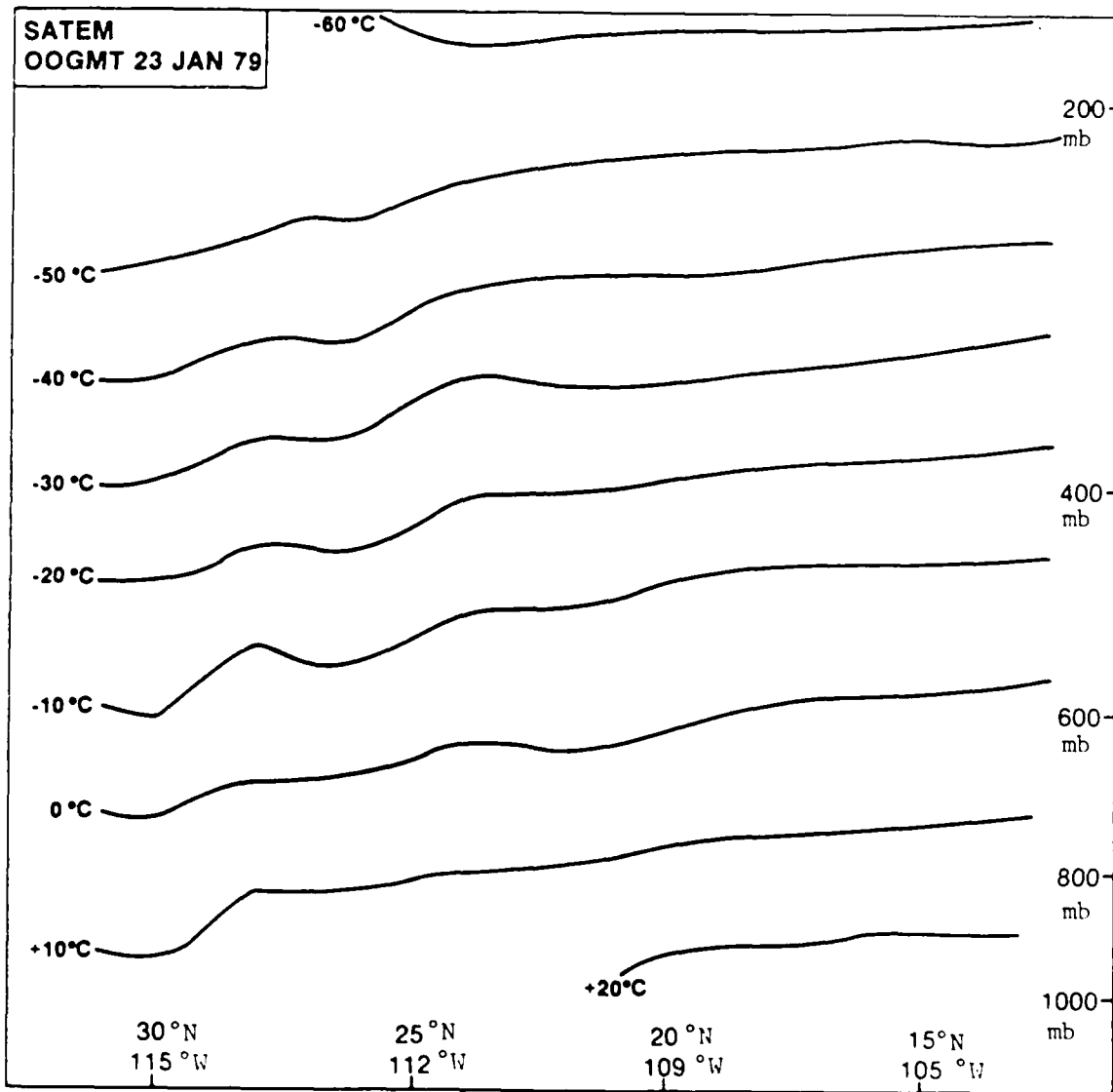


Fig. 2. As in Fig. 1 except for 0000 GMT 23 January 1979.

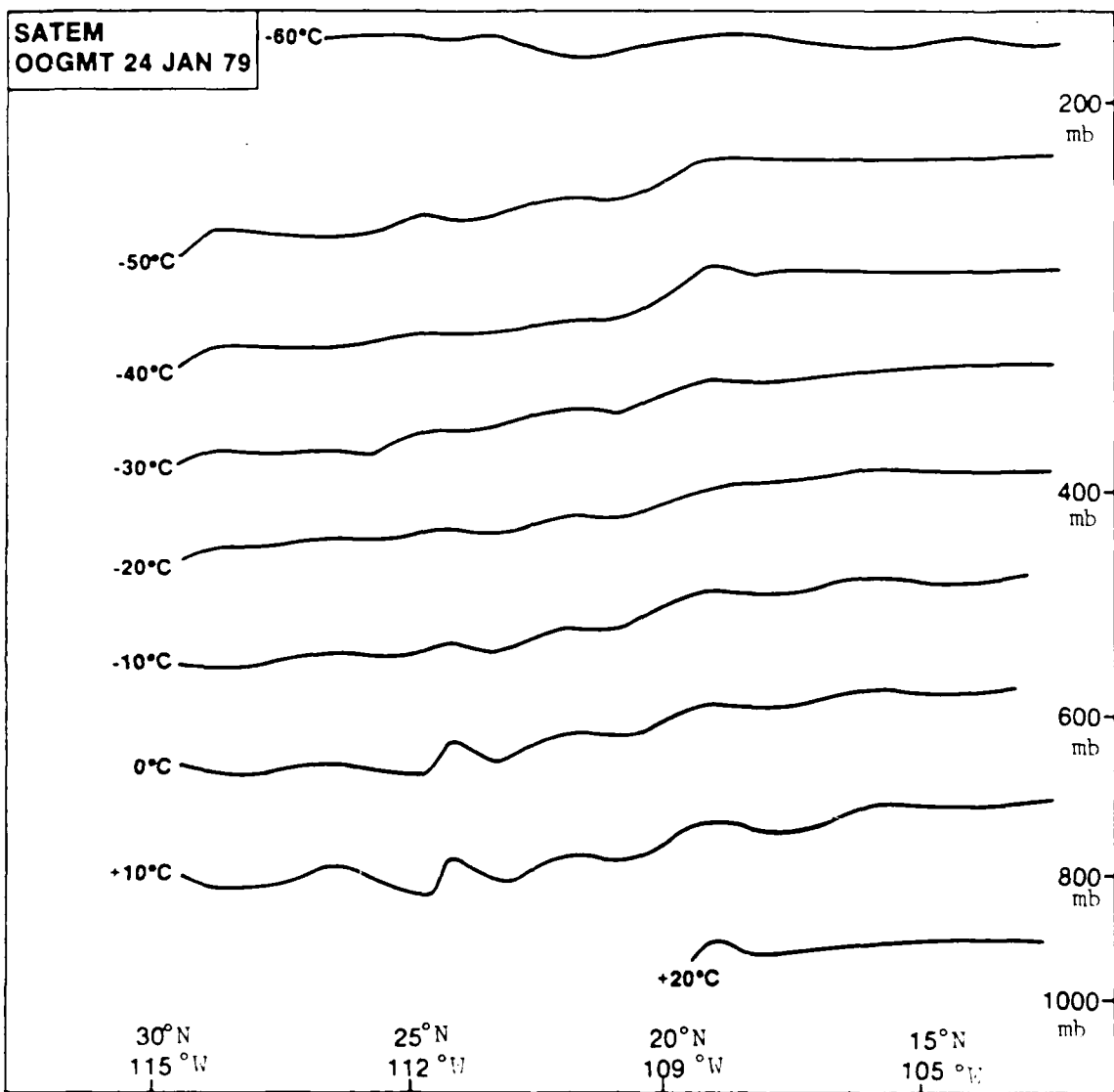


Fig. 3. As in Fig. 1 except for 0000 GMT 24 January 1979.

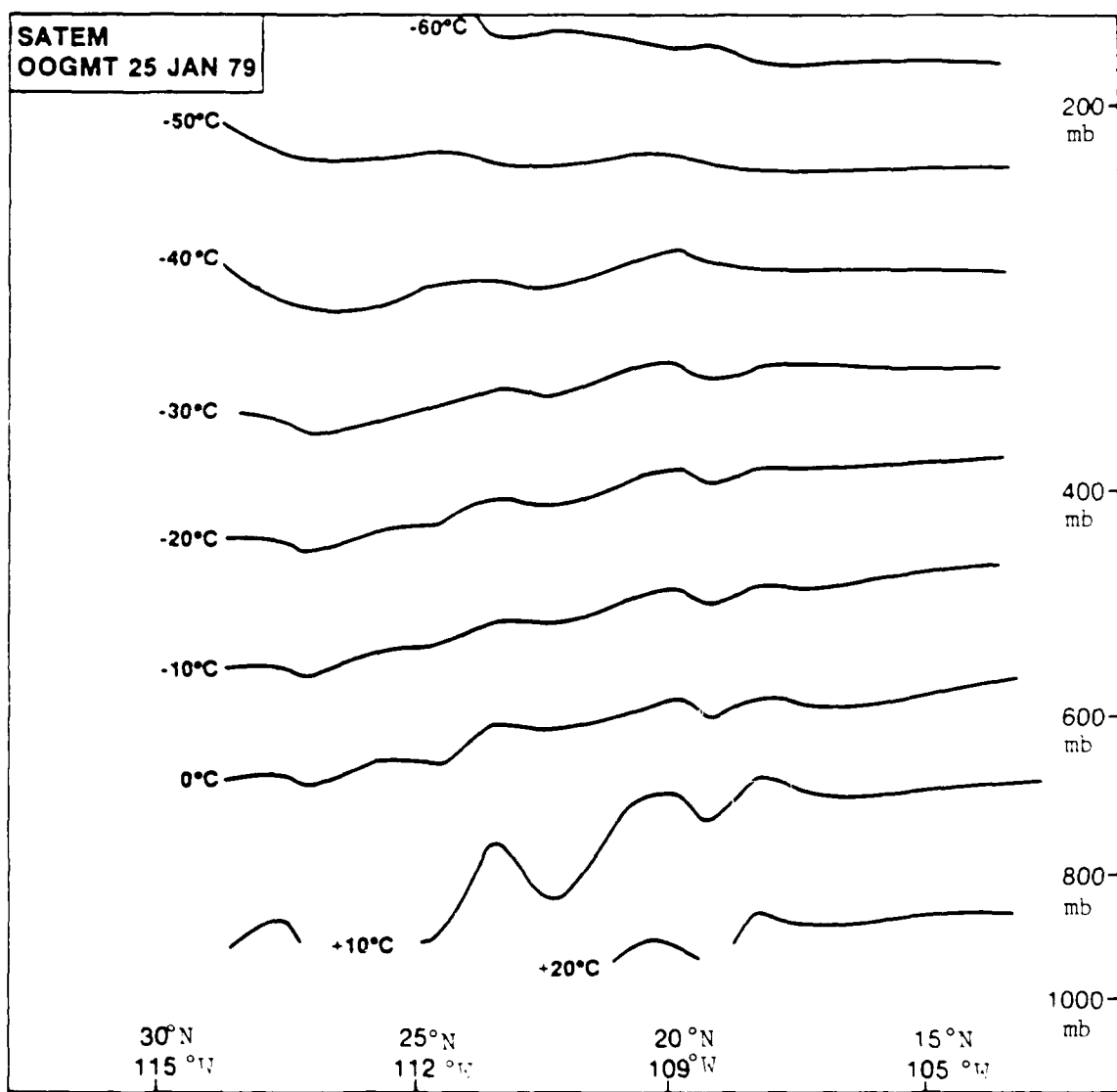


Fig. 4. As in Fig. 1 except for 0000 GMT 25 January 1979.

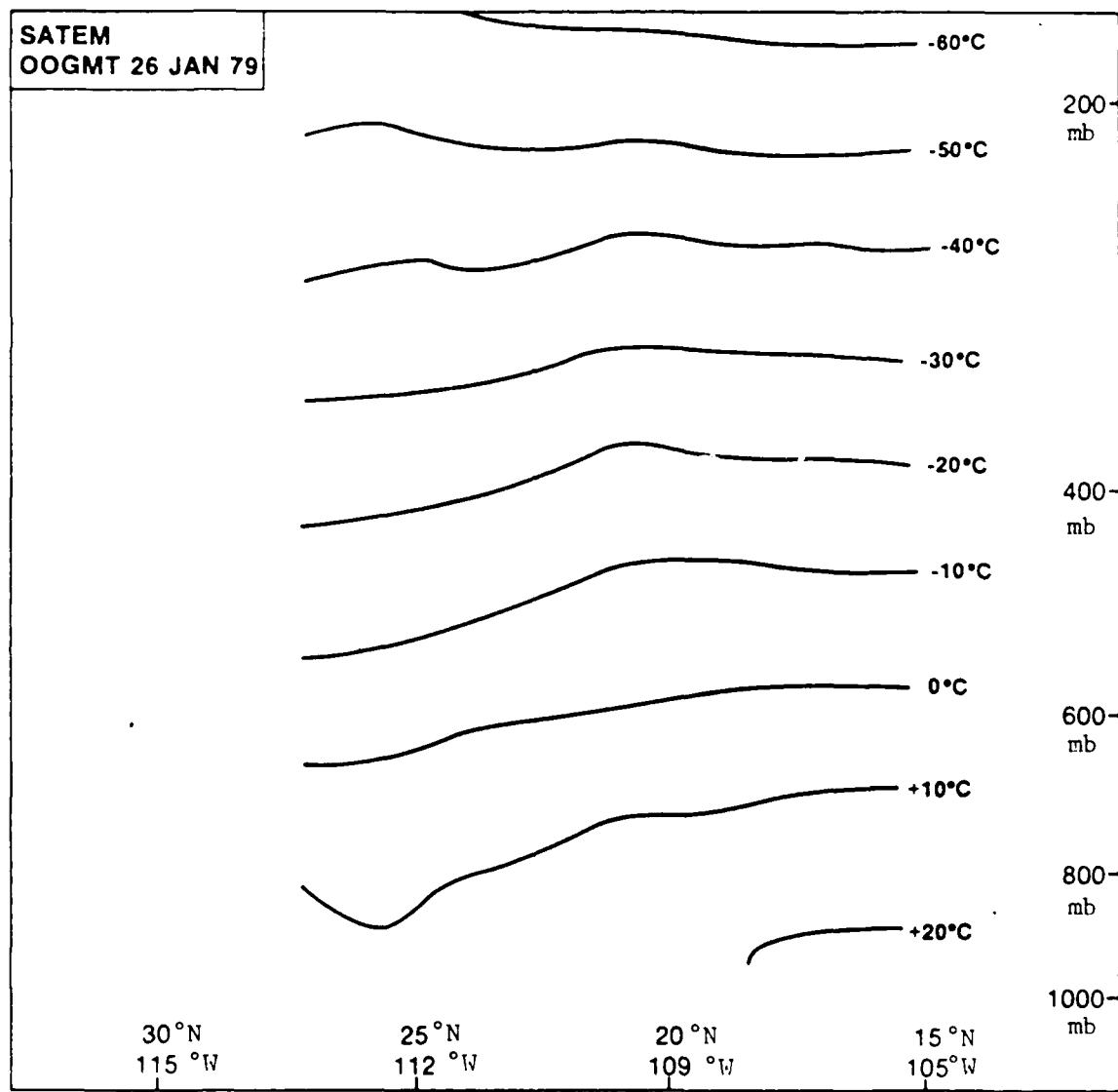


Fig. 5. As in Fig. 1 except for 0000 GMT 26 January 1979.

about 200 mb, and cooler temperatures to the south above about 200 mb. The layer average temperatures in the SATEM cross sections did not show any of the various inversions present in the radiosonde cross sections. The horizontal temperature gradients found on the SATEM sections are not obvious on the radiosonde sections in the same general locations.

The remainder of this section is an examination of possible reasons for the temperature changes, discussed in the figure descriptions, and of possible uses for SATEMs in data sparse areas.

The locations of the SATEMs were plotted geographically to investigate possible sounding contamination. The sounding locations did not correspond to coastline crossings (one possible form of contamination (Staelin *et al.*, 1975)). The location maps were compared with IR imagery and it was found that they were not correlated with any cloud signal or contamination, such as where one location was clear and another cloudy.

A plot of the SATEM locations suggests a possible explanation for the apparent strong and irregular gradients present in the sections. The linear cross sections used for the SATEM soundings considered the distance between soundings in only one plane. Therefore, some of the seemingly sharp temperature differences did not necessarily imply a correspondingly large temperature gradient, but merely reflected the temperature change over the large distances normal to the cross section. This does not create the cross section temperature gradients, but merely intensified the horizontal temperature gradients that are present on the cross sections. This problem is especially evident in Fig. 4 where the apparent linear distance of the sharp temperature fluctuations around $22^{\circ}\text{N}/110^{\circ}\text{W}$ is only about 80 km, whereas the actual distance is about 650 km.

The locations of these temperature gradients were then plotted on the corresponding FGGE IIIb gridded temperature data charts for the appropriate times and levels (not shown). The temperatures and temperature gradients would only match the FGGE IIIb temperatures by shifting the FGGE IIIb analyses approximately 2° westward (about 220 km). This shift resulted in a reasonable correlation between the SATEM data and the FGGE IIIb data. The 220 km is within the grid scale for the FGGE IIIb data. This correspondence also explains the lack of agreement between the SATEM and radiosonde cross sections. The temperature gradients are mostly east-west gradients and are therefore reflected in the SATEMs due to the linear problems, and not reflected in the mainly north-south radiosonde cross sections.

The FGGE IIIb model makes extensive use of the SATEM information in deriving the temperature analyses, and have been shown to agree reasonably well within the grid scale. The use of mean layer temperatures in the SATEM data will not identify inversions and small scale horizontal temperature gradients, but they do demark the location of high amplitude large synoptic scale temperature gradients. The FGGE IIIb temperature charts already do this and have better data coverage. Also, the SATEMs are missing in the area of concern for the 21st and 22nd, the origin period of the first moisture burst. Therefore it was decided that even though there are uses for SATEM cross sections, they were not used in this study.

c. Statistical analysis of FGGE IIIb data

Many scientists already have studied the usefulness of the FGGE IIIb analyses (see Chapter 2), but in order to investigate the applicability to this study, where data sparsity is an especially serious problem, several statistical methods were employed.

To check the validity of the FGGE IIIb RH analyses two methods were used. For the first temporal standard deviations were computed for FGGE IIIb RH and a TIROS-N satellite moisture channel with a weighting function peaking near 700 mb. The temporal standard deviations were computed to investigate the ability of both the model and the satellite channel data to vary in time. To compare the FGGE IIIb RH analyses with the satellite-derived data several cross-correlation coefficient mapping were accomplished. Similar temporal standard deviation and cross-correlation coefficient analyses were done for FGGE IIIb temperatures and appropriate satellite channels.

The temporal standard deviations and cross-correlation coefficients were calculated over the nine day period of 21-29 January 1979, on a $3.75^\circ \times 3.75^\circ$ latitude/longitude grid, and then analyzed. The satellite-derived data are expressed as effective brightness temperatures; the FGGE IIIb temperatures are in $^{\circ}\text{C}$ and the FGGE IIIb RH are in percent from 0-100%.

1) Moisture variability

Fig. 6 is the mapping of the nine day temporal standard deviation for 1000 mb RH. There is little temporal variability over the ocean regions. There are three small areas of standard deviation greater than 20%; one is over the ocean along the equator between 93°W and 100°W . The other two areas are over North America along the path of the moisture bursts. Of course, little temporal variation should be expected at 1000 mb because of the near proximity of the ocean surface as an ever-present source, except for the northeast corner of the area.

Fig. 7 shows the temporal standard deviation analysis for 850 mb RH. The same three areas remain, although slightly larger in amplitude and in extent. There are

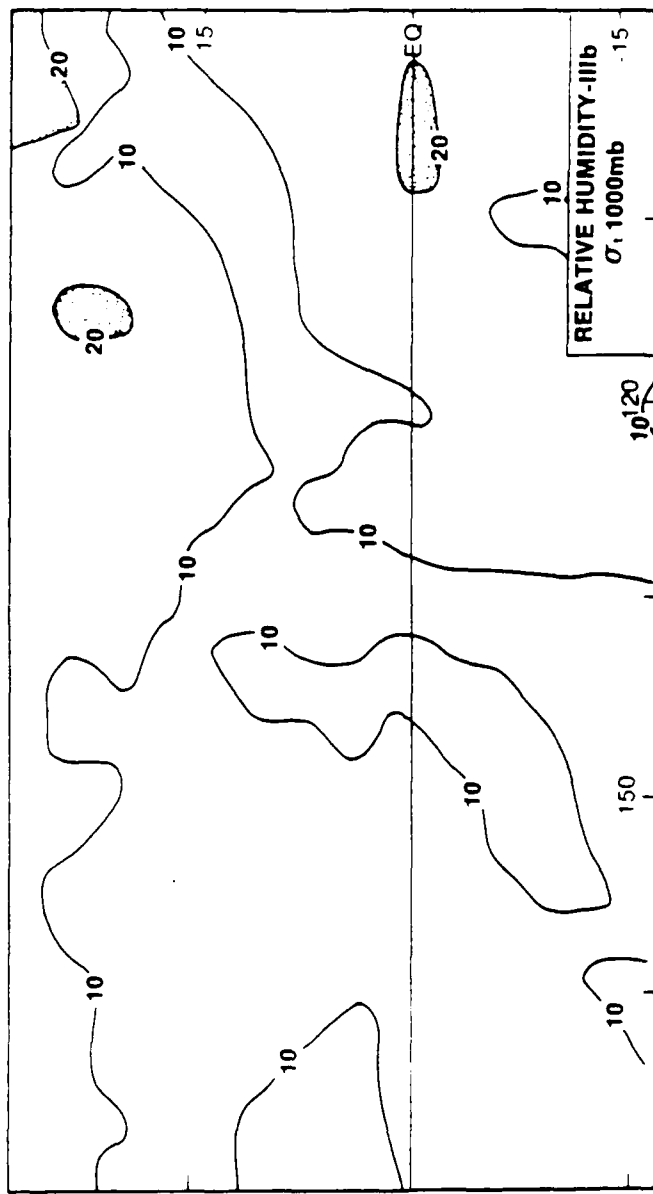


Fig. 6. Grid point temporal standard deviation for FGGF IIIb 1000 mb relative humidity.
Time period is 0000 GMT 21 January to 0000 GMT 29 January 1979. Units are % R.H.

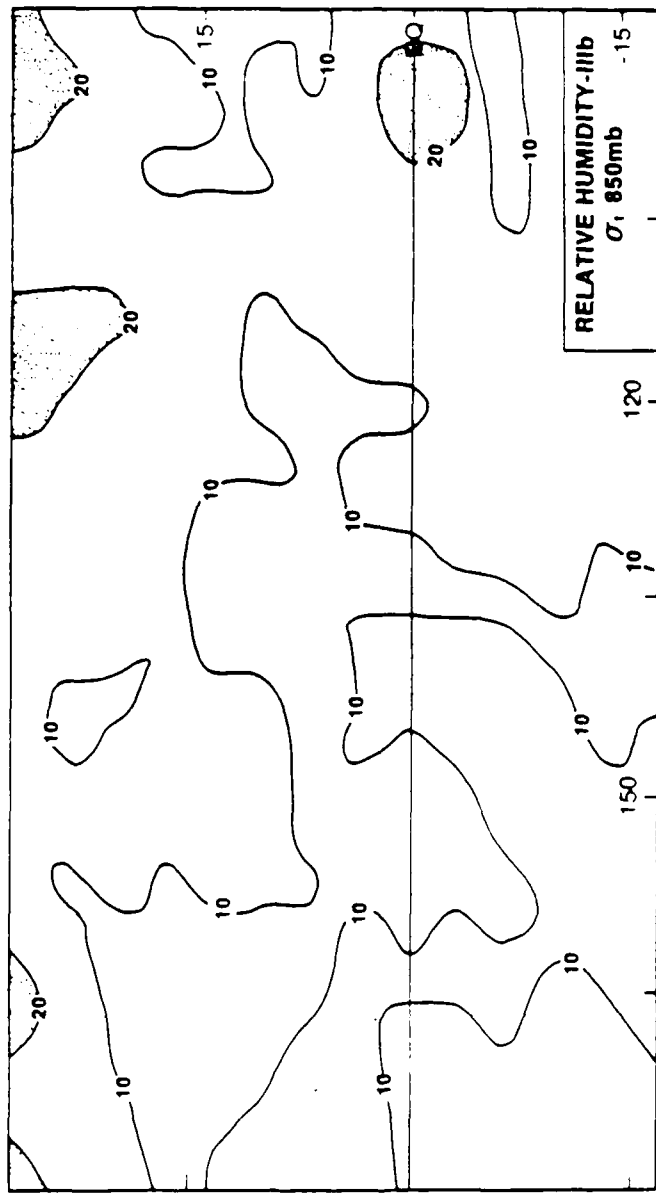


Fig. 7. As in Fig. 6 except for 850 mb.

also two small areas of greater than 20% standard deviation to the northwest of Hawaii at $30^{\circ}\text{N}/168^{\circ}\text{W}$ and $30^{\circ}\text{N}/180^{\circ}\text{W}$. The origin regions of the two moisture bursts continue to have low standard deviations.

At 700 mb (Fig. 8) the temporal standard deviation exceeds 30% in only one area and the spatial pattern changes dramatically. This region of high variability is located at $19^{\circ}\text{N}/146^{\circ}\text{W}$ and is within an almost continuous region of greater than 20% standard deviation that reflects the approximate path of the first moisture burst from $3^{\circ}\text{N}/175^{\circ}\text{W}$ to $30^{\circ}\text{N}/90^{\circ}\text{W}$ (the extent of the mapping). South of 20°N the path of the second burst is not marked by high variability at this level.

The analysis of temporal standard deviation at 500 mb (Fig. 9) shows an even larger area of deviations exceeding 30% along the path of the first burst, and also extending eastward into the region of the second burst. The region of deviations above 20% does encompass virtually the entire second burst. In addition to the high variability along the burst axis, there is a region of larger variability along the South Pacific Convergence Zone (SPCZ) which extends into the southern hemisphere at 150°W (Huang and Vincent, 1983). At 400 mb (not shown) the pattern is the same, although the area of significant variation is even larger and the amplitudes increase slightly as well.

Fig. 10, which shows the temporal standard deviation for satellite channel 12 reveals a pattern north of the Equator which is similar to that of Fig. 9. The area of maximum deviation is shifted slightly southeast and seems to represent both bursts. Also, along the equator east of 120°W , the satellite data show little variability, whereas the FGGE IIIb data suggests significant variation. The satellite data show relatively larger variability in the ITCZ near the dateline than does the FGGE IIIb analyses.

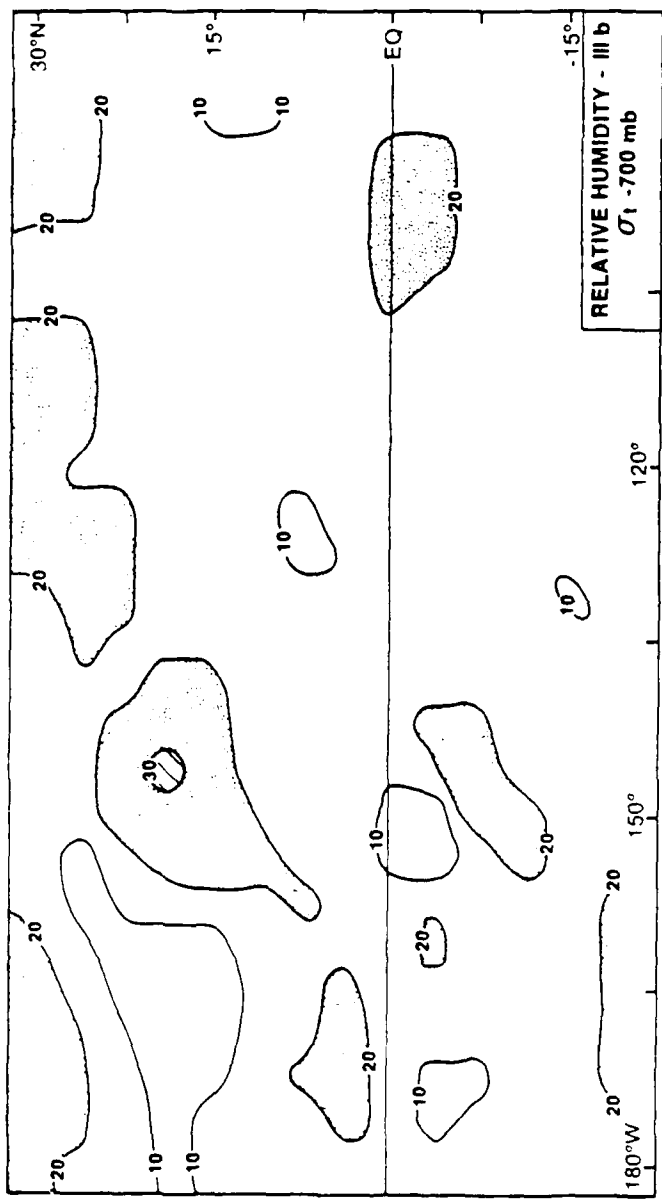


Fig. 8. As in Fig. 6 except for 700 mb.

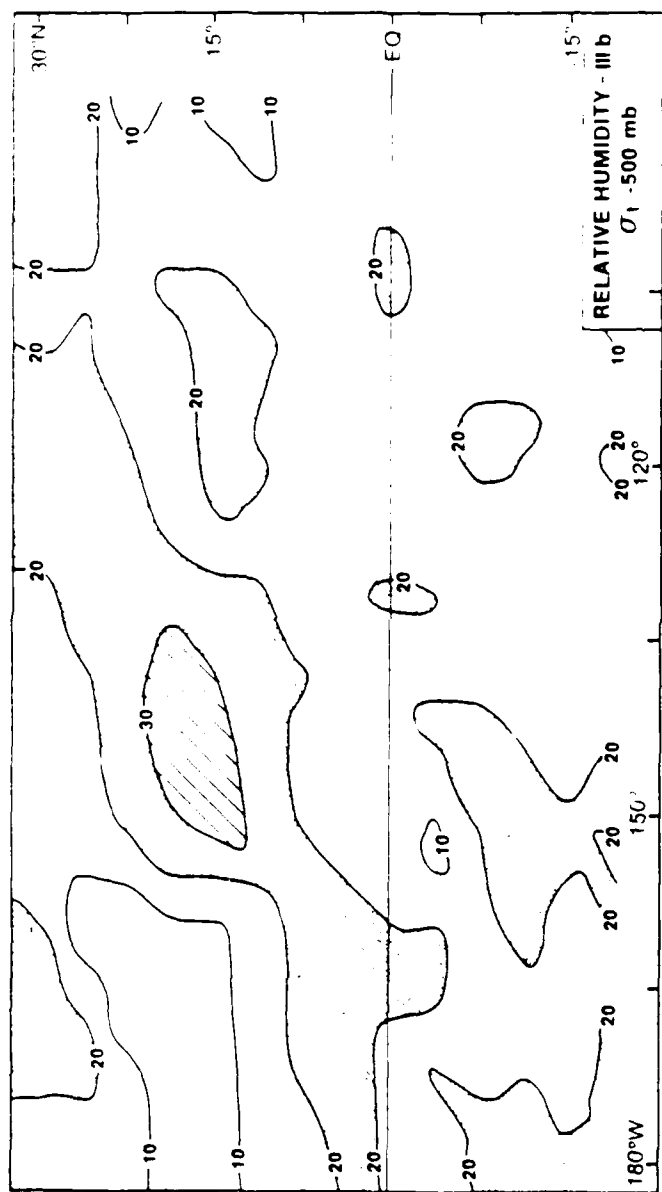


Fig. 9. As in Fig. 6 except for 500 mb.

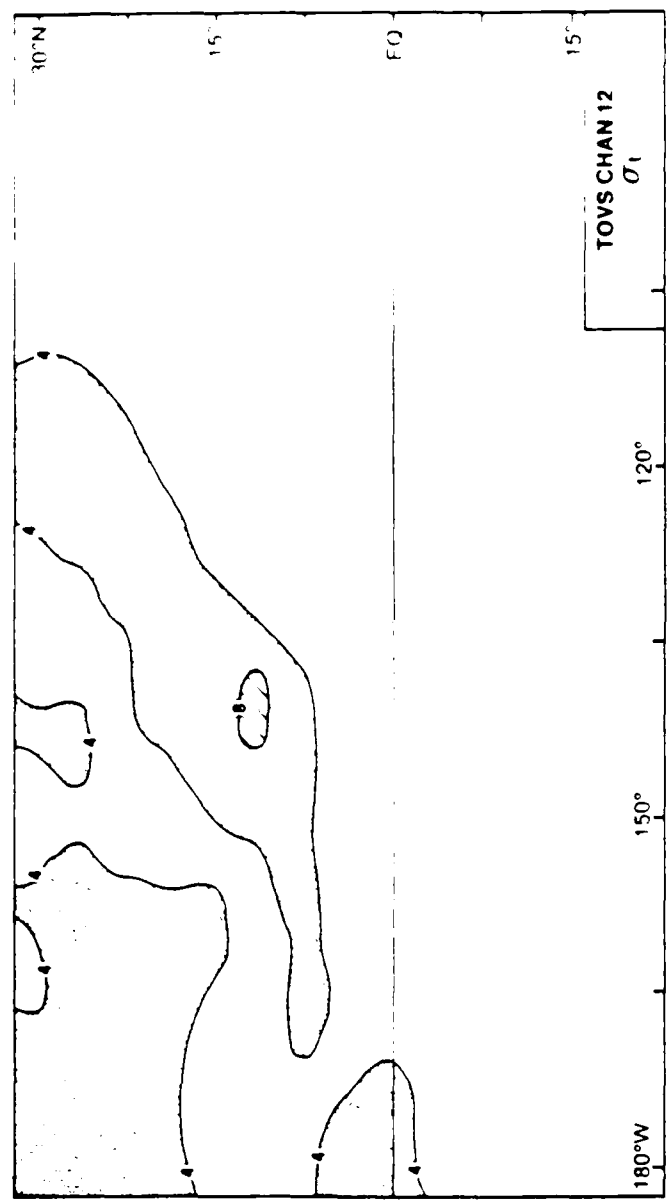


Fig. 10. As in Fig. 6 except for satellite channel 12 (a moisture channel with the weighting function peaking near the 500 mb surface). The isolines are standard deviation of brightness temperature in $^{\circ}\text{C}$.

The cross-correlation coefficient mapping of FGGE IIIb 700 mb RH versus satellite channel 11 brightness temperature (Fig. 11) shows an area of good correlation in the region of the first burst. This region is also where the FGGE IIIb RH had large variability (Fig. 8). Because the satellite moisture channel data are presented as brightness temperature (which increases when the RH goes down and vice versa), the negative correlations are expected. The region just to the north and west of the burst axis is an area of low correlation. This area corresponds to an even larger area of poor correlation at 500 mb (see Fig. 12), which extends into the burst origin region where both the satellite channel data (Fig. 10) and the FGGE IIIb standard deviation mapping (Fig. 9) show significant variability.

Because the FGGE IIIb model did not contain any moisture input above the surface, there was concern that there would be little pattern over the tropical oceans where low level moisture has little variability compared to mid-latitude continental regions. Significant variability in moisture content was found, especially at upper levels, along the burst axes. The FGGE IIIb model must be dynamically transporting moisture up from lower levels. This moisture is transported upward and/or advected into the moisture burst region. The temporal standard deviation analyses do not indicate the timing of this transport of moisture; they show only that moisture does vary. The analyses also show that not only is the moisture burst region moist, but the moisture is also highly variable.

The cross-correlation mapping for 500 mb (Fig. 12) shows the timing and/or pattern variability is different between the FGGE IIIb and satellite channel in the origin region of the first burst. A simple t-test results in a 90% confidence limit of approximately -0.4. Because of the way the analysis is initialized, in data sparse areas, the individual grid point values will not be independent; thus, the t-test

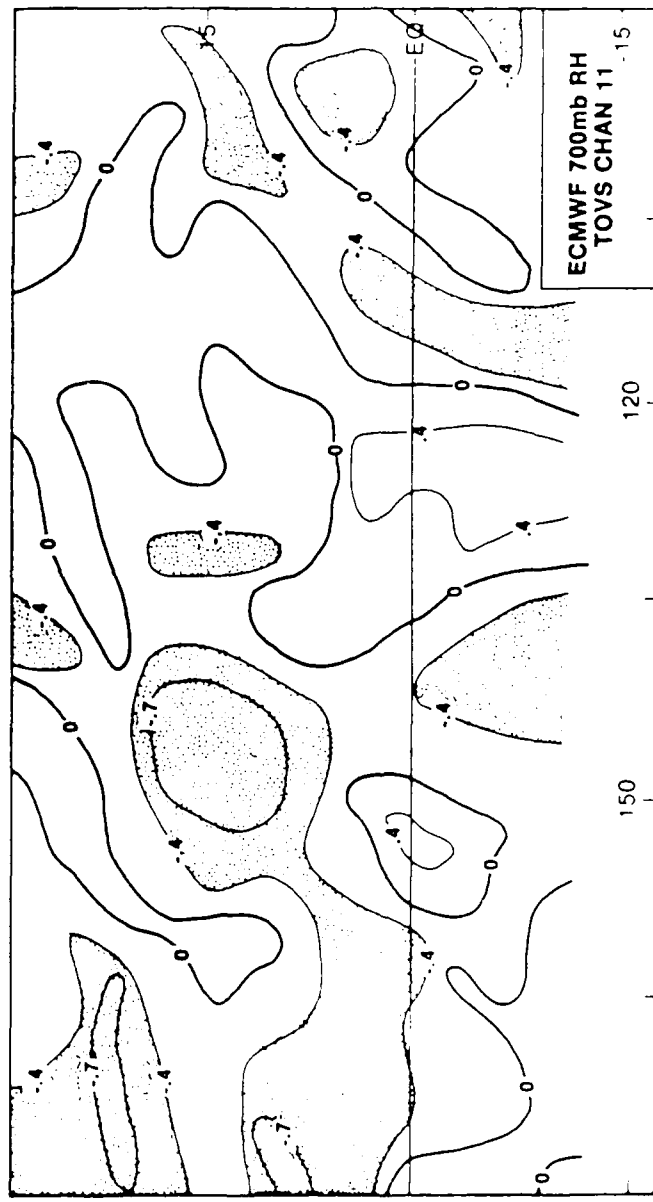


Fig. 11. Grid point cross-correlation coefficients of FGGE IIIb 700 mb R H vs. satellite channel 11 (a moisture channel with the weighting function peaking near the 700 mb surface). The time period is 0000 GMT 21 January 1979 to 0000 GMT 29 January 1979.

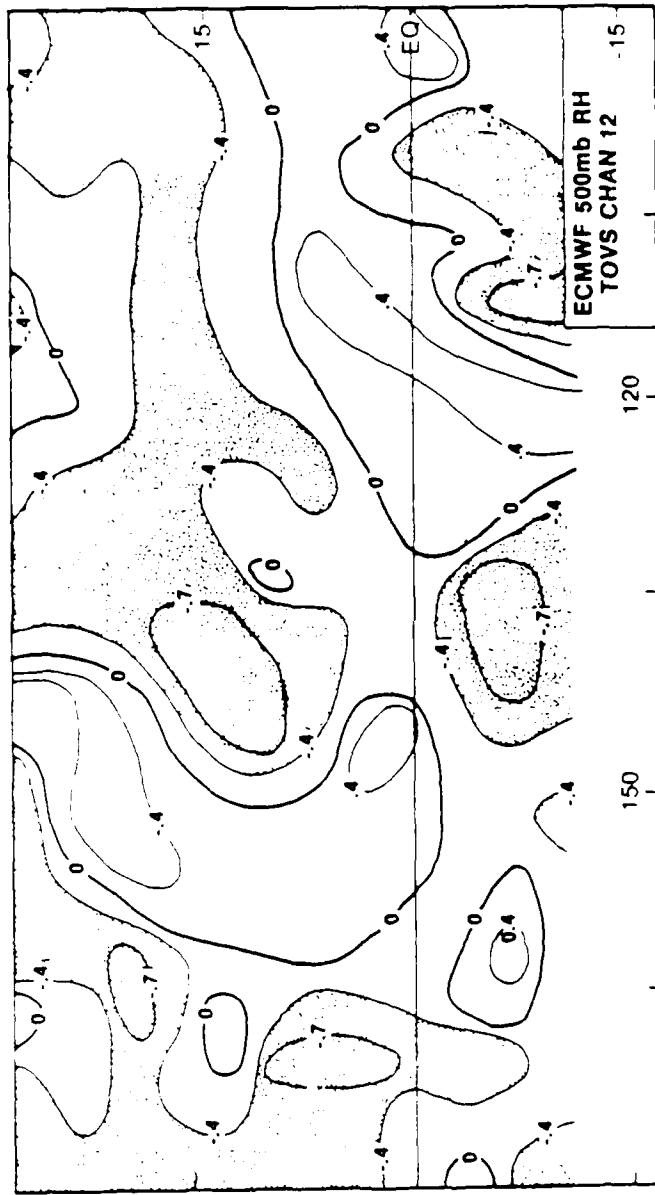


Fig. 12. As in Fig. 11 except for 500 mb R.H. vs. satellite channel 12 (a moisture channel with the weighting function peaking near the 500 mb level).

probably overestimates statistical significance. The same figure also reveals that the areas of higher correlation correspond generally to regions of higher moisture variation (therefore at least occasionally high moisture). McGuirk and Thompson (1985) made a comparison of FGGE IIIb moisture with co-located radiosonde data and found that there was good agreement between ECMWF analyses and satellite observations in areas of greater than 50% RH and poorer agreement in regions of lesser relative humidity. The important synoptic point in these RH standard deviation mappings is the increasing variability with height in the burst region. There is little variability in the low levels; the variability increases to a peak at 400 mb of almost 30% at about $19^{\circ}\text{N}/140^{\circ}\text{W}$ in the burst axis. Coupled to the amplitude of the variation is the pattern definition along the burst axis; this is another important synoptic point.

2) Thermal variability

Fig. 13 is the 1000 mb temporal standard deviation for FGGE IIIb analyzed temperature. There are two areas of significant variability. The region in the northeast corner is over the North American continent where larger variation is expected. The other area is over the eastern Pacific centered at approximately $23^{\circ}\text{N}/120^{\circ}\text{W}$; this region is within the approximate path of both bursts. This high variability extends southwestward to the equator at about 145°W , slightly east of the origin of the first burst, but the 2°C line extends to the region of the origin of the first burst. The variation is low (less than 1°C) near Hawaii. At 850 mb (Fig. 14) the pattern is similar, although the area of significant variability around $15^{\circ}\text{N}/145^{\circ}\text{W}$ has shrunk considerably. The corresponding analysis at 700 mb (Fig. 15) continues this trend of lesser variability all along the burst axes. There is a

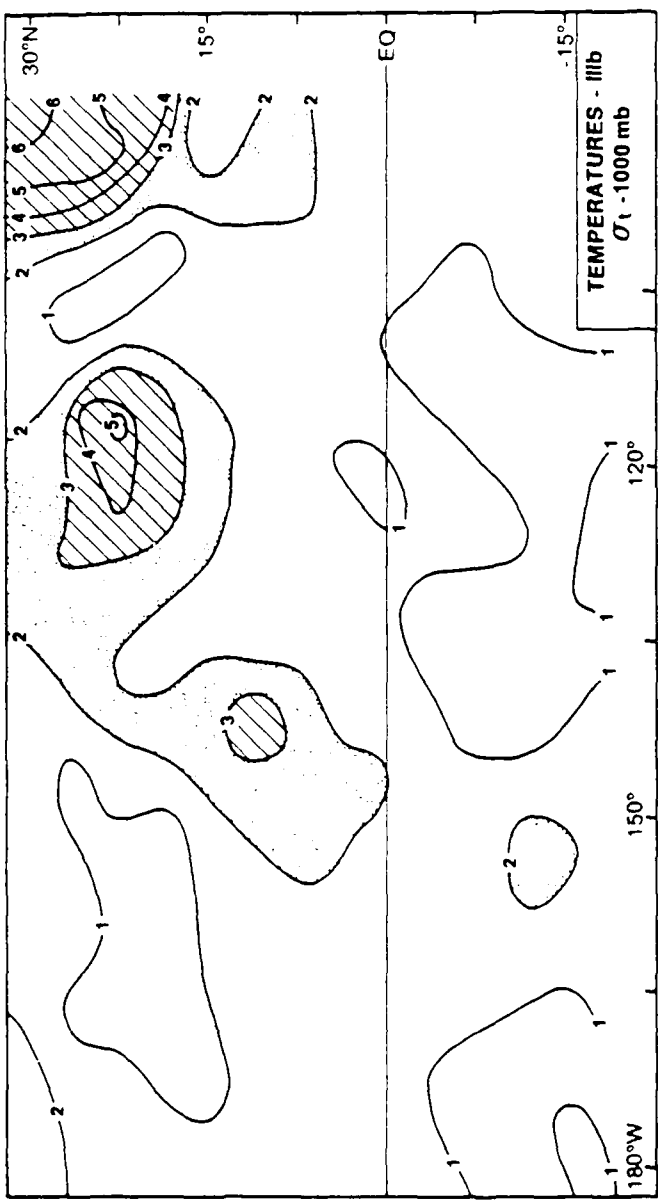


Fig. 13. Grid point temporal standard deviations for FGGE IIb 1000 mb temperatures. The time period is 0000 GMT 21 January 1979 to 0000 GMT 29 January 1979. Units are $^{\circ}\text{C}$.

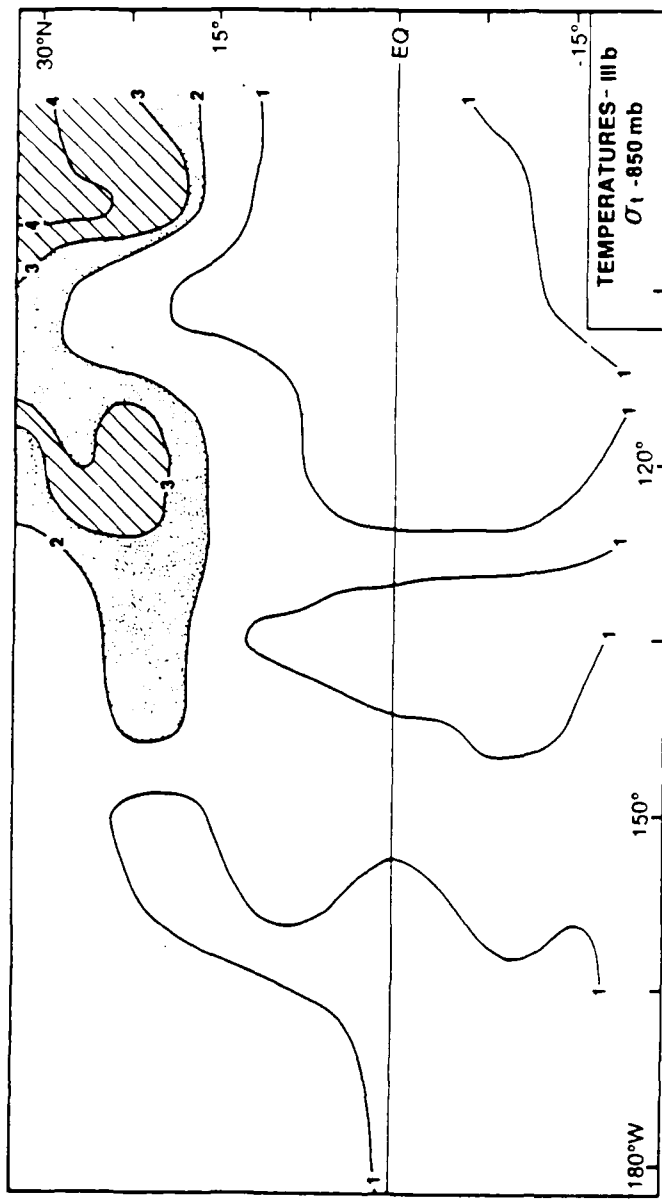


Fig. 14. As in Fig. 13 except for 850 mb.

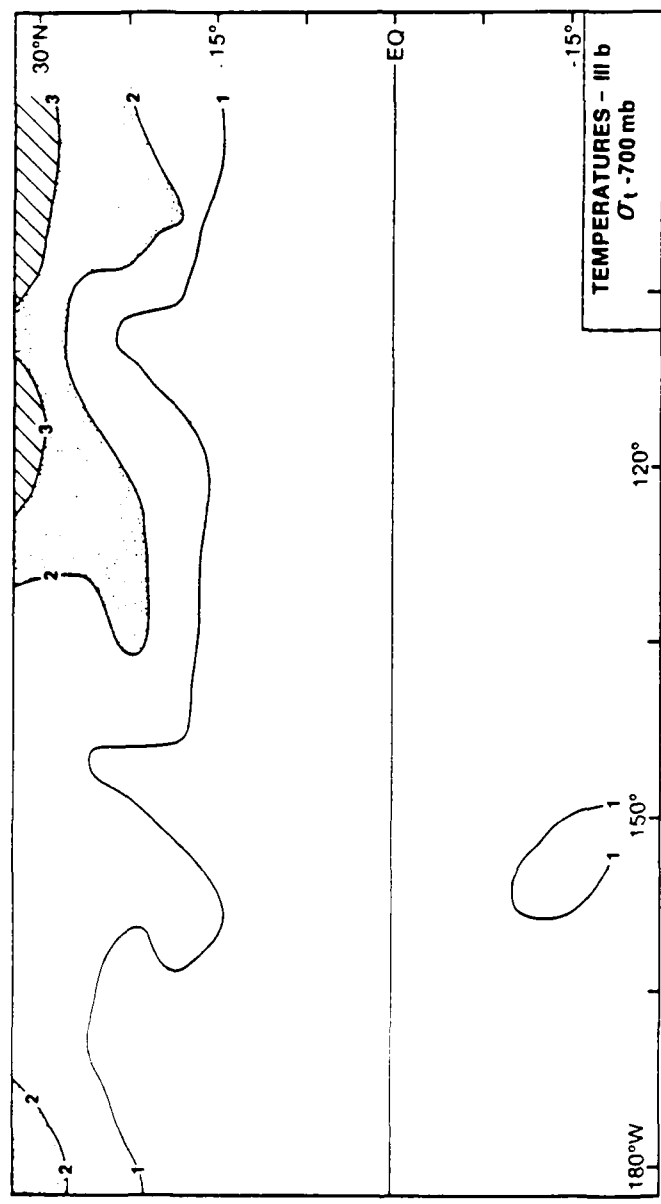


Fig. 15. As in Fig. 13 except for 700 mb.

small area of standard deviation greater than 2°C in the northwest corner of the analysis. This same area grows and values increase at 500 mb (not shown). The variability along the burst axes is no longer apparent south of 15°N . The 400 mb analysis (Fig. 16) shows continued increase of variability in the northwest with one value exceeding 4°C . The area of greater than 2°C has enlarged, and is nearly continuous across the region north of 25°N . There is a region of local maximum variability along the north-central area of the chart that has expanded meridionally, rather than contracted, with increasing height. It is interesting to note that the moisture burst area and to the northwest (shown in Section 4b to be a trough region) is a region of high variability while the equatorial region has low variability.

At 300 mb (Fig. 17) the northwestern area of high variability is even larger. There is a region greater than 3°C centered approximately at $20^{\circ}\text{N}/155^{\circ}\text{W}$ which extends into the area of the first burst.

Significant variation appeared at all levels over the continental area of the northeast corner of the analyses. In the lower layers this variability could be due to larger temperature variation over continents, but in the upper levels surface effects cannot account for all of this variation. Increased radiosonde data, available to the FGGE IIIb analyses scheme over the continents, probably accounts for some of this increased variability in the upper levels.

The analyses of temporal standard deviation for satellite channel 15 (Fig. 18) shows a pattern similar that of the FGGE IIIb 700 mb temperature standard deviation analysis (Fig. 15). There is an area of deviation greater than 2°C in the northeast corner of the mapping over the continent. There is also an area of deviation greater than 2°C at about $20^{\circ}\text{N}/120^{\circ}\text{W}$, that is in the path of the moisture burst. There is little pattern in the origin areas of the moisture bursts.

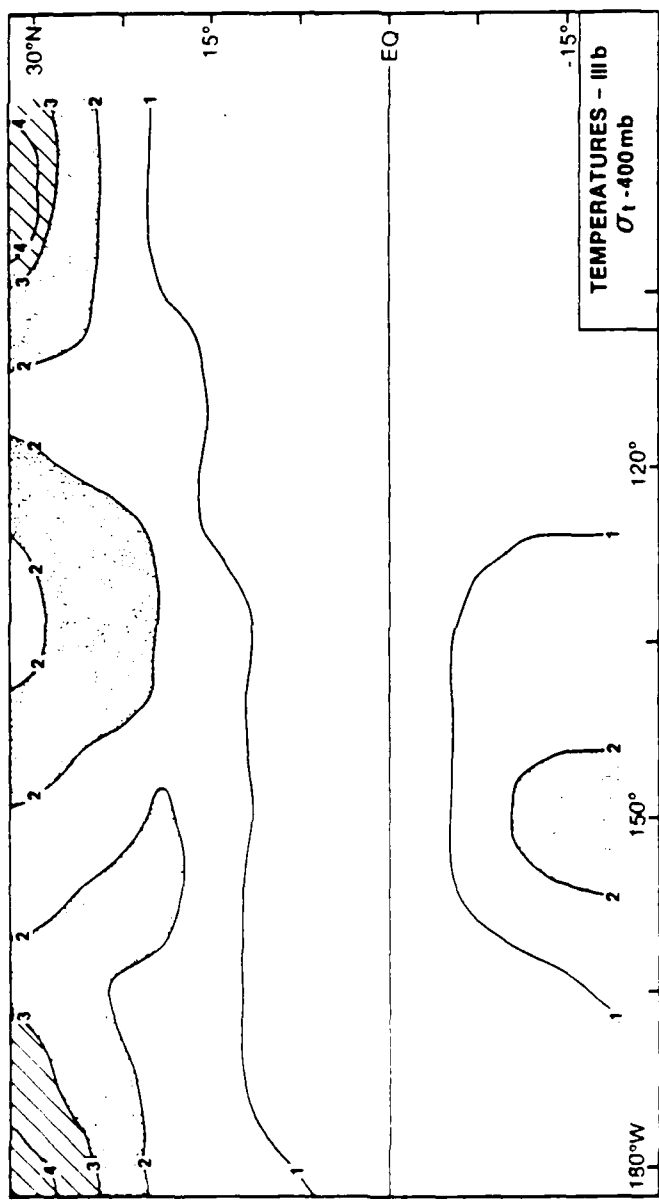


Fig. 16. As in Fig. 13 except for 400 mb.

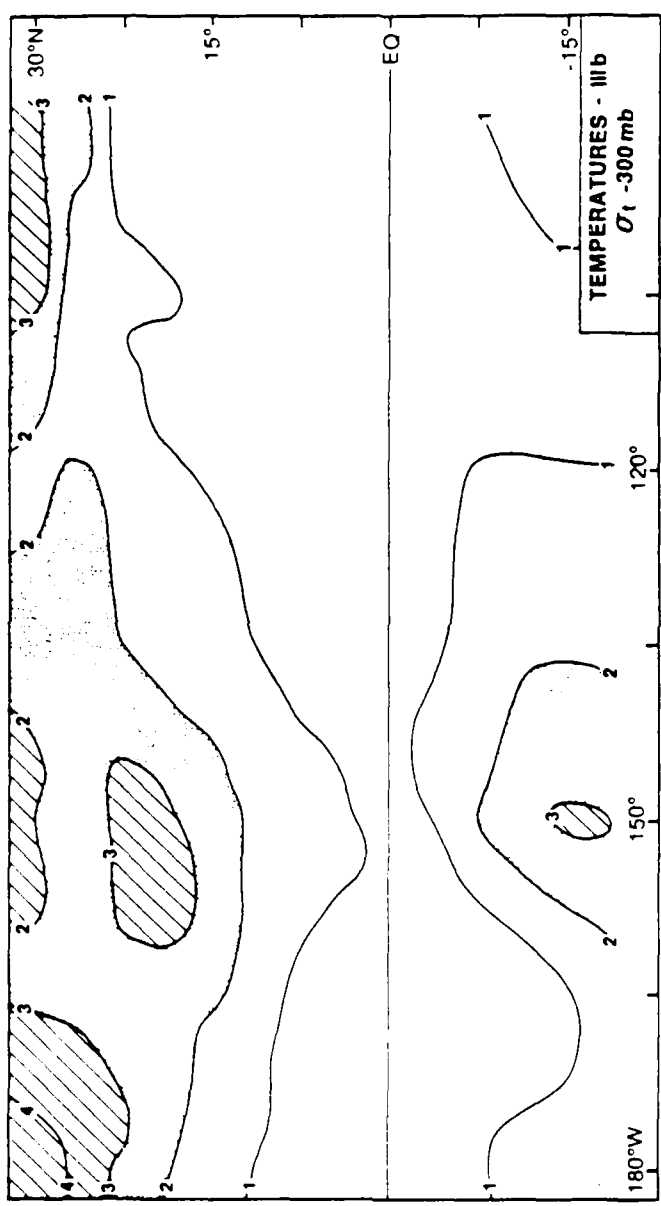


Fig. 17. As in Fig. 13 except for 300 mb.

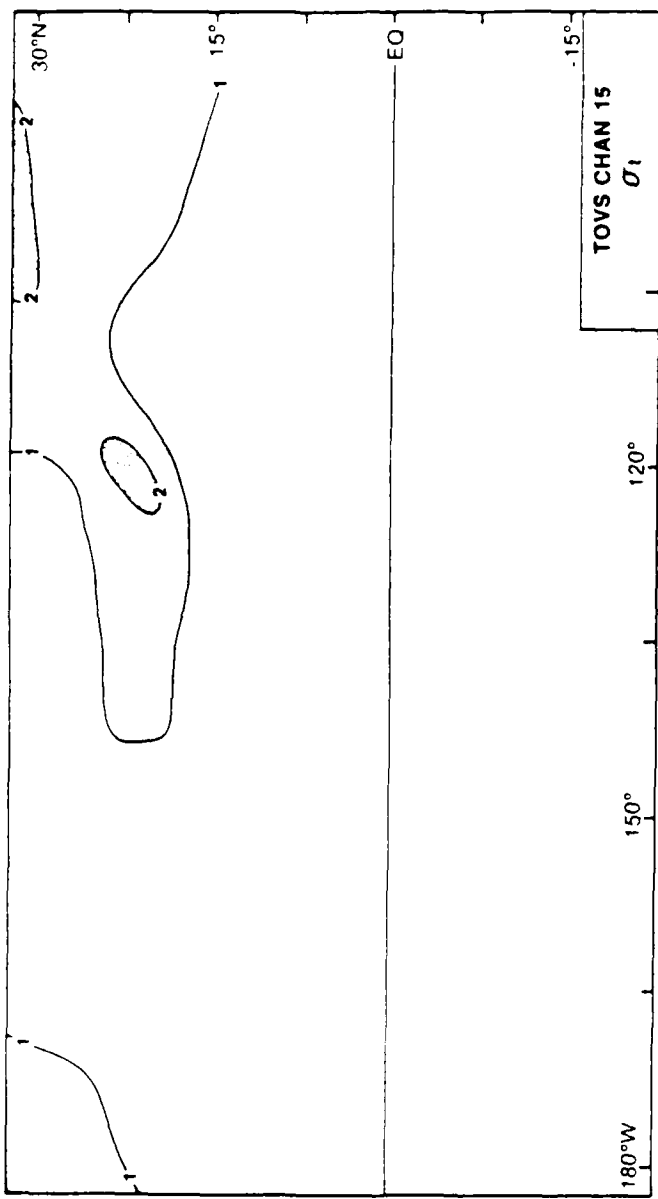


Fig. 18. As in Fig. 13 except for satellite channel 15 (a temperature channel with the weighting function peaking near the 700 mb surface).

Cross-correlation coefficients analysis for FGGE IIIb 700 mb temperature versus satellite channel 15 (Fig. 19) generally show good correlation. The pattern is almost random, showing that there are not any favored locations for good correlation. Therefore there seems to be no synoptic bias.

The temporal standard deviations point to the temperature fluctuating within the burst at the low levels and to the northwest of the burst at upper levels. The variability at 70 mb may be related to the upper-level troughs intruding into tropical regions; typically, these troughs are associated with moisture bursts, as pointed out by Anderson and Oliver (1970), Thepenier and Cruette (1981), and Smith *et al.* (1985). The temperature variability in the upper levels is addressed in Sections c and e in Chapter 4.

The FGGE IIIb data sets seem to reflect the patterns of moisture and temperature variability. There also is good agreement with the satellite data sets for temperature and moisture, at least in the wet regions. The FGGE IIIb analyses still lack the detail needed for small synoptic scale or mesoscale studies, but they seem able to represent larger synoptic scale features, in spite of the lack of in situ observations. These data sets will therefore be used, with a certain degree of confidence, in cases where conventional data are scarce, yet a relatively dense field of data is needed. It is important to realize, however, that the FGGE IIIb analyses may not be precise, particularly in regions experiencing rapid change.

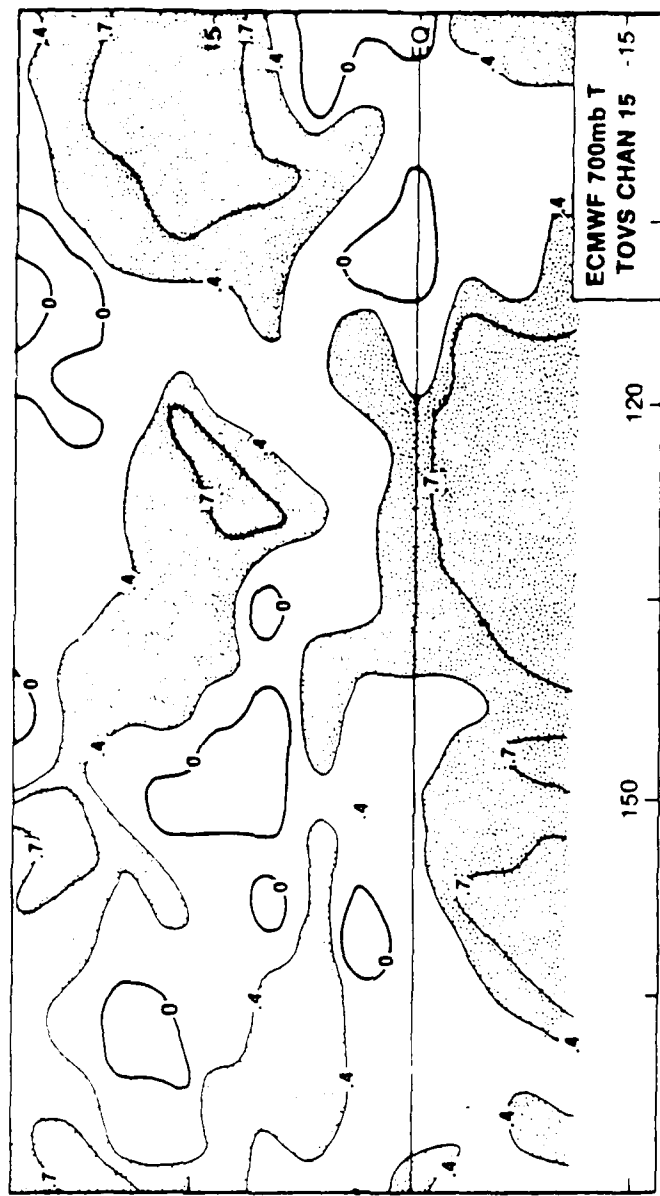


Fig. 19. Grid point cross-correlation coefficients of FGGE IIIb 700 mb temperature vs. satellite channel 15 (a temperature channel with the weighting function peaking near the 700 mb surface).

CHAPTER IV

SYNOPTIC ANALYSIS

The previous chapter discussed the various data sources, and investigated the applicability of several of the available data sets. In this chapter data are used to aid in a synoptic investigation of the two moisture bursts.

a. Satellite-derived imagery

This section on interpretation of satellite-derived pictures of the eastern Pacific Ocean during the period of concern is based primarily on various satellite imagery as enumerated in Chapter 3. The only imagery used as figures are black and white IR and visual photographs. At times, several of the features discussed will not be as apparent as they are in the other forms of imagery which cannot be reproduced in the thesis format (color-enhanced IR, and high time resolution film loops).

On 20 January 1979 at 0000 GMT (not shown) clouds of a previous moisture burst (already terminated as a moisture burst) remain located from the United States southwestward to the equator at about 160° W. Associated with this previous moisture burst is a low pressure system just off the west coast of the United States. Convective activity in the burst origin region is occurring along the ITCZ between the equator and 12° N, from 160° W westward to the dateline. A second, and stronger, low pressure system, confirmed in NOAA operational analysis, is centered at approximately 45° N/ 154° W with a cold front extending to just northwest of the Hawaiian Islands. The clouds associated with this front do not extend southward of 25° N/ 155° W; therefore, accurate placement of the front at its southern end is difficult.

By 1200 GMT on the 20th (not shown), the previous moisture burst is weaker, although there are still virtually unbroken clouds almost to the equator at 155°W . The northern Pacific low pressure system contains a band of scattered clouds stretching as far south as Hawaii. This cloud band is not entirely evident on the still pictures, but shows up well on IR film loops. These clouds are possibly related to the cold front intruding into the tropics. This feature will be further discussed in Section 4e. The area between this front and the old burst (about 900 km wide) contains only scattered cumulus. In the southern hemisphere tropics, there is a large band of convective activity in a line almost north-south along 150°W as far north as 5°N , and there is evidence in the motion of the clouds of some south-to-north cross-equatorial moisture flow. This feature is discussed by Huang and Vincent (1983), who computed flow as high as 15 ms^{-1} from the SPCZ to the northern hemisphere in this region.

An area of weak convective activity, detached from the northern cold front by 0000 GMT on the 21st (Fig. 20), lies just to the east-northeast of Hawaii at point A. East of Hawaii at $20^{\circ}\text{N}/145^{\circ}\text{W}$ (point B), a region of low clouds has developed, with cloud tops becoming higher. A narrow band of scattered low clouds extends southwestward from this area to the ITCZ directly south of Hawaii. The cloud band associated with the northern cold front has passed over the Hawaiian Islands and a narrow cloud free area has formed in the vicinity of the frontal zone (point C). Once again, these features are not overwhelmingly evident on the still pictures but they show up well on the film loops.

By 1200 GMT on the 21st (Fig. 21) the largest area of cloudiness running from south of Hawaii almost to 130°W satisfies the necessary requirements to be classified a moisture burst (Smith *et al.*, 1985). The film loops confirmed that the moisture

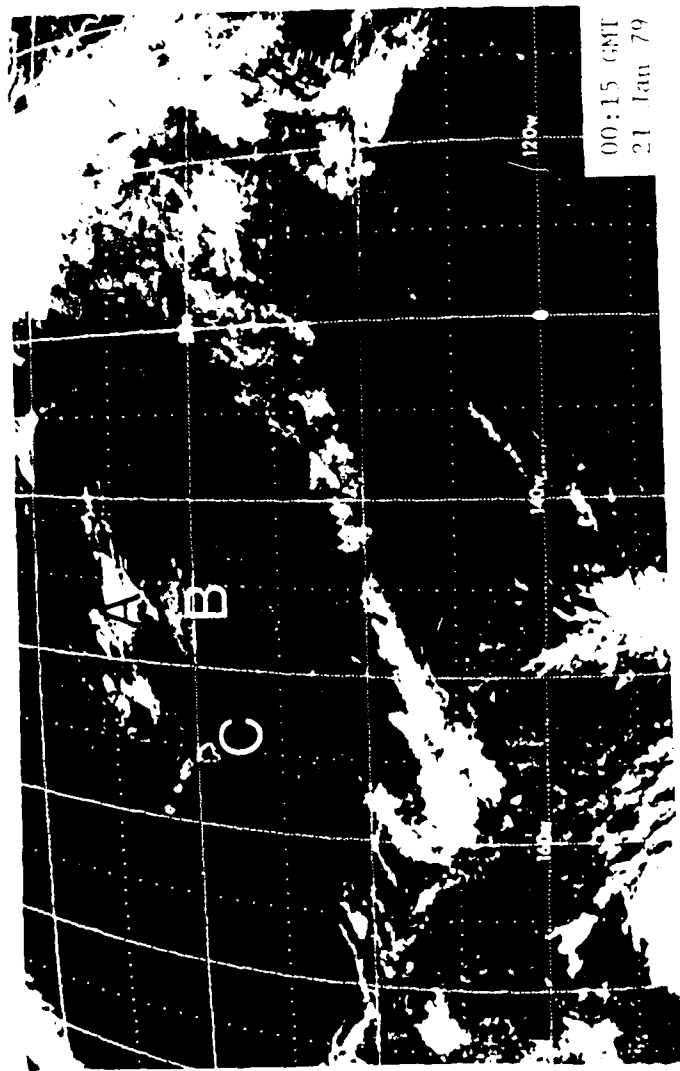


Fig. 20. Unenhanced GOES West IR satellite photograph for 0015 GMT 21 January 1979.
See text for explanation of the letters.

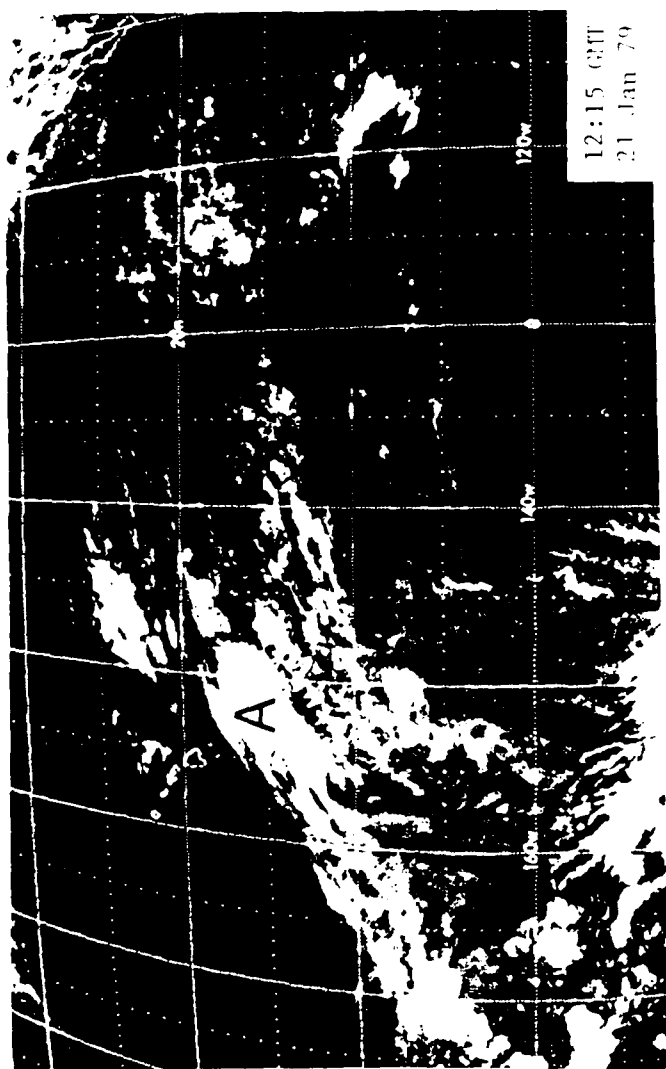


Fig. 21. As in Fig. 20 except for 1215 GMT 21 January 1979.

burst initiated at approximately 0300 GMT. The majority of the cloudy area is composed of rapidly forming cirrus near 400 mb (as determined from GOES enhanced IR imagery) along the northwest edge of the moisture burst at area A. The visual satellite photo for 1745 GMT on the 21st (Fig. 22) shows that the cirrus is probably thin with a limited amount of small cumulus or stratocumulus below (point A). This cloud patch formed much too quickly to be totally advected into the area. It would have required wind speeds of over 90 ms^{-1} to be advected into the area. This area of cirrus, combined with the western edge of the previous burst and the area of convection just to the east-northeast of Hawaii (point B) forms the moisture burst. It is emphasized that this burst may initiate nearly simultaneously in three different locations and with three different cloud morphologies. The sharp poleward edge of the cirrus shield indicates the approximate location of the subtropical jet (Anderson *et al.*, 1969).

The eastern and northern portion of the burst is an area of deep convection at 0000 GMT on the 22nd (Fig. 23). The northern part, marked A, is very active with strong convection. This is the region where the jet stream seems to turn to a nearly zonal direction. The western portion of the cloud cover is still predominantly thin cirrus with some trade cumulus below, with a possible convective line at point B, well separate from the cloud mass at A.

By 1200 GMT on the 22nd (Fig. 24) the majority of the burst appears to have become convectively active. The strongest activity is still associated with the eastern area (point A), but even the western area (point D), has become convectively active. To the east of the active region where the burst curves anticyclonically and the flow becomes nearly zonal (point C), the clouds become mostly thin cirrus. The streaky pattern is jet streaks and the leading edges of these propagated 1500 km in the 12 h preceding 1200 GMT on the 22nd; they extend nearly to Baja California.

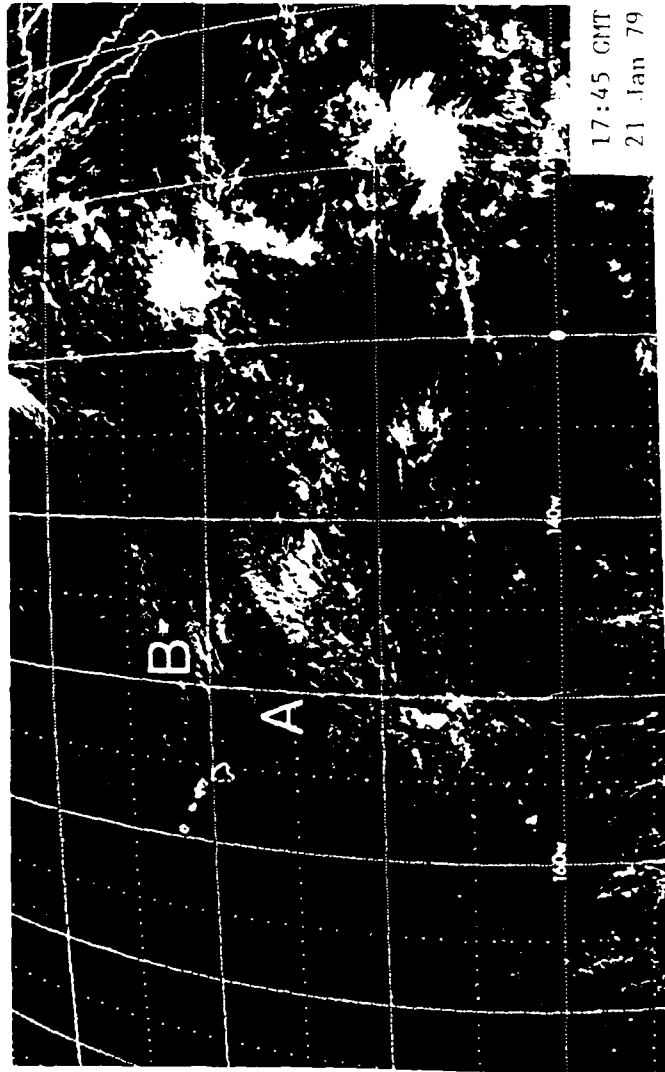


Fig. 22. Visual GOES West satellite photograph for 1745 GMT 21 January 1979.

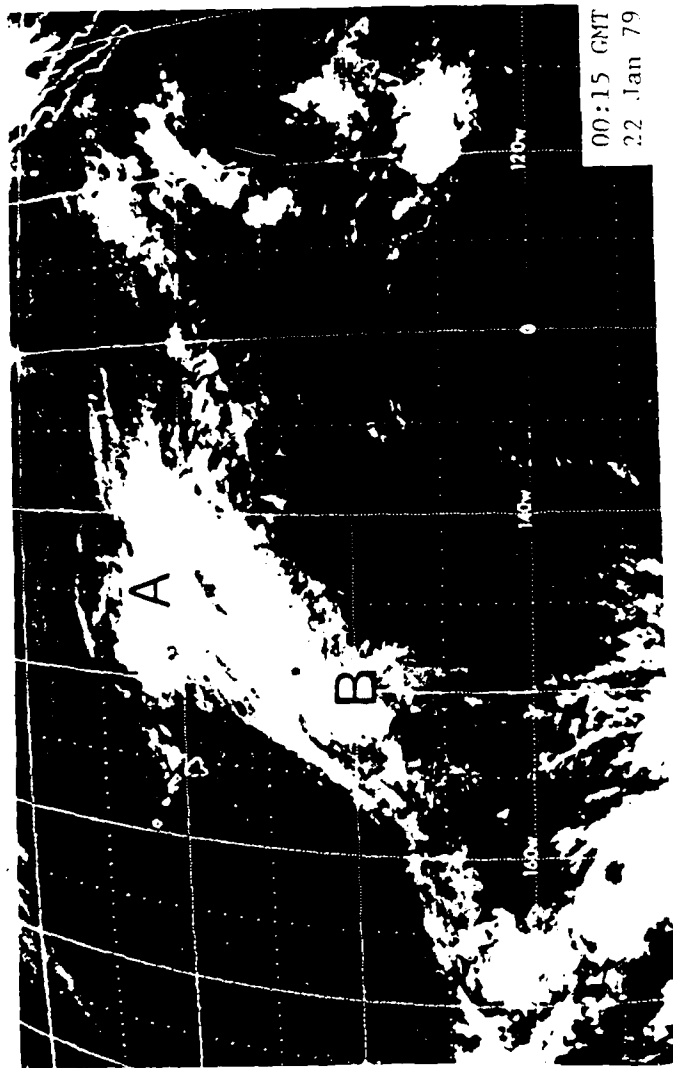


Fig. 23. As in Fig. 20 except for 0015 GMT 22 January 1979.

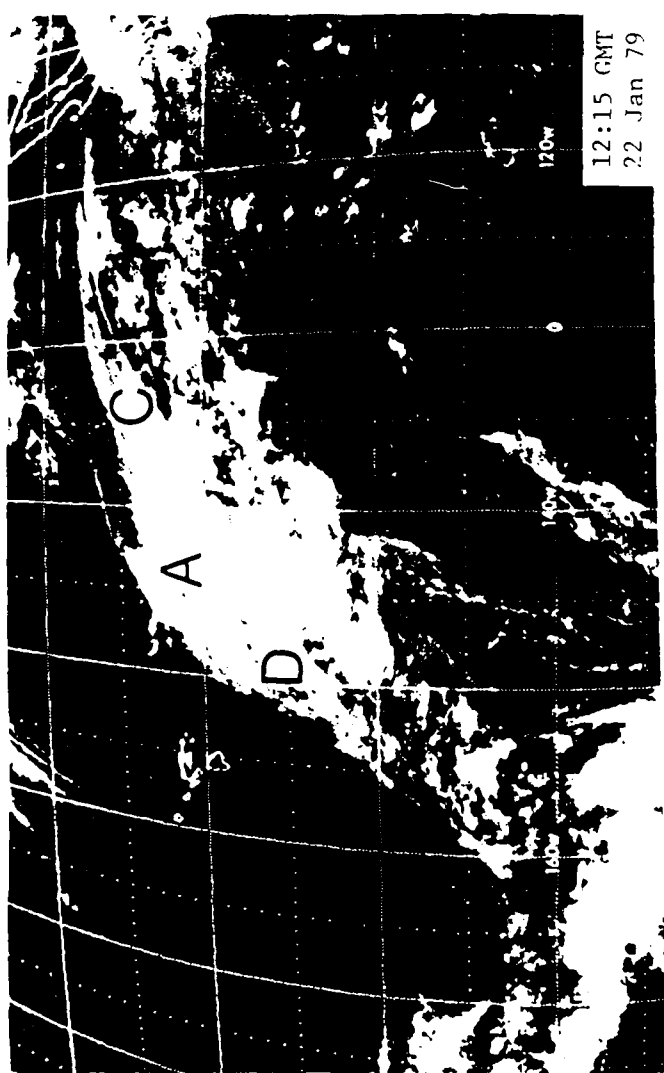


Fig. 24. As in Fig. 20 except for 1215 GMT 22 January 1979.

The northern region (point A) is still dominated by cirrus at 0000 GMT on the 23rd (Fig. 25). A strong convective region has reformed at $7^{\circ}\text{N}/153^{\circ}\text{W}$ (point B); cloud tops extend above 300 mb; this convection was present at burst initiation (Fig 20), but had been absent for nearly 48 hours. This convection weakens to the north.

More activity generates at $10^{\circ}\text{N}/150^{\circ}\text{W}$ (point B) by 1200 GMT on the 23rd (Fig. 26). The cirrus in the northern portion of the burst (point A) has combined with widespread cloudiness over the low pressure center off the coast of the Americas.

A region of cloudiness, dominated by cumulus, redevelops southeast of Hawaii by 0000 GMT on the 24th (point A, Fig. 27). The large convective region at about $4^{\circ}\text{N}/153^{\circ}\text{W}$ has persisted (point B).

The southern convective region weakens noticeably by 1200 GMT on the 24th (Fig. 28). This weakening also shows up as the burst cloud mass begins to break up and lose cohesion along the axis. The cloudiness southeast of Hawaii (point A) has grown slightly, and may be associated with a possible cold front from a second polar low moving into the northeastern Pacific. The indication of the jet stream on the satellite imagery is not well defined, which could be due to either the jet stream weakening, or drier air in the jet stream region.

By 0000 GMT on the 25th (Fig. 29) the convection in the burst has virtually stopped and the first burst has terminated, by definition, as a moisture burst. Although there is still some isolated activity, the burst has broken up. The cloudy area to the southeast of Hawaii is moving eastward slowly.

The cloudy area to the southeast of Hawaii has drifted east to $17^{\circ}\text{N}/142^{\circ}\text{W}$ and combined with the remnants of the burst by 1200 GMT on the 25th (point A, Fig. 30). The burst regained some intensity due to a line of convection, located at 8°N

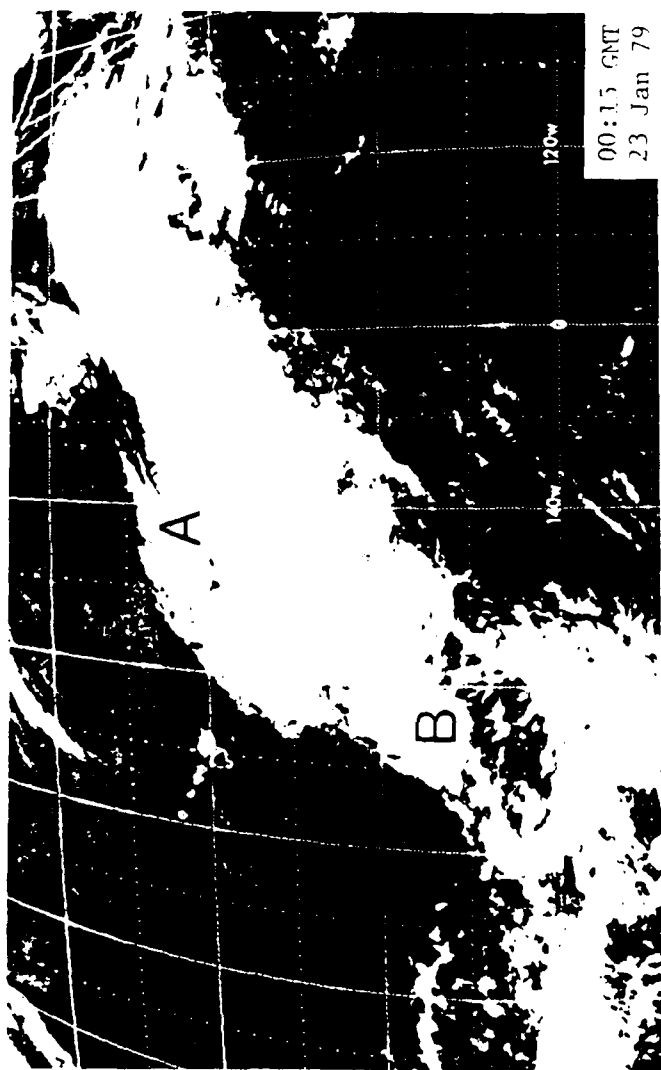


Fig. 25. As in Fig. 20 except for 0015 GMT 23 January 1979.

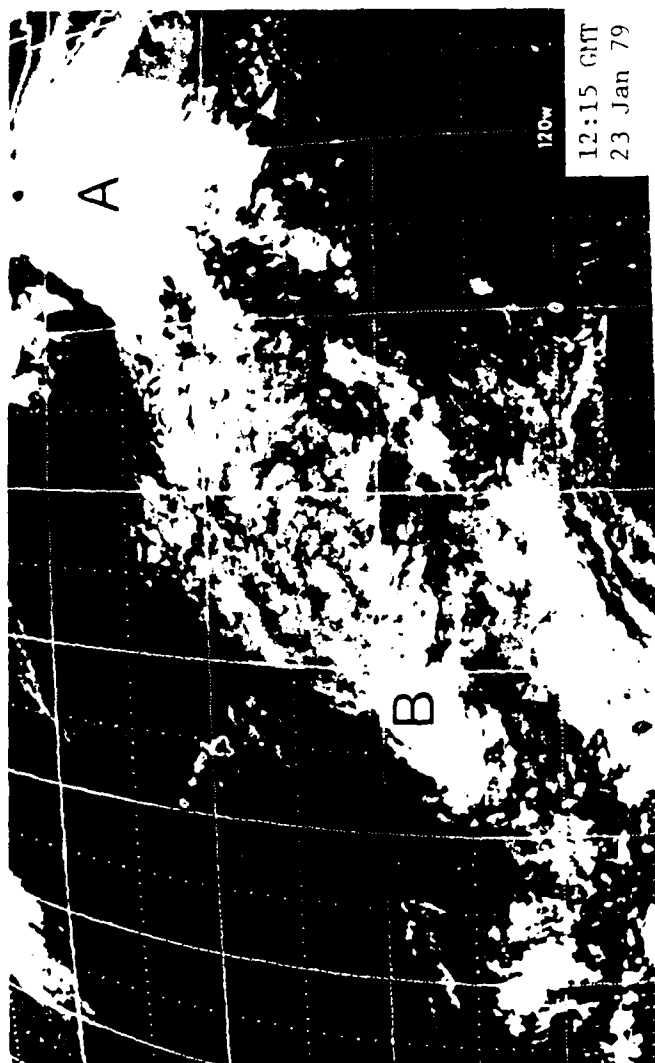


Fig. 26. As in Fig. 20 except for 1215 GMT 23 January 1979.

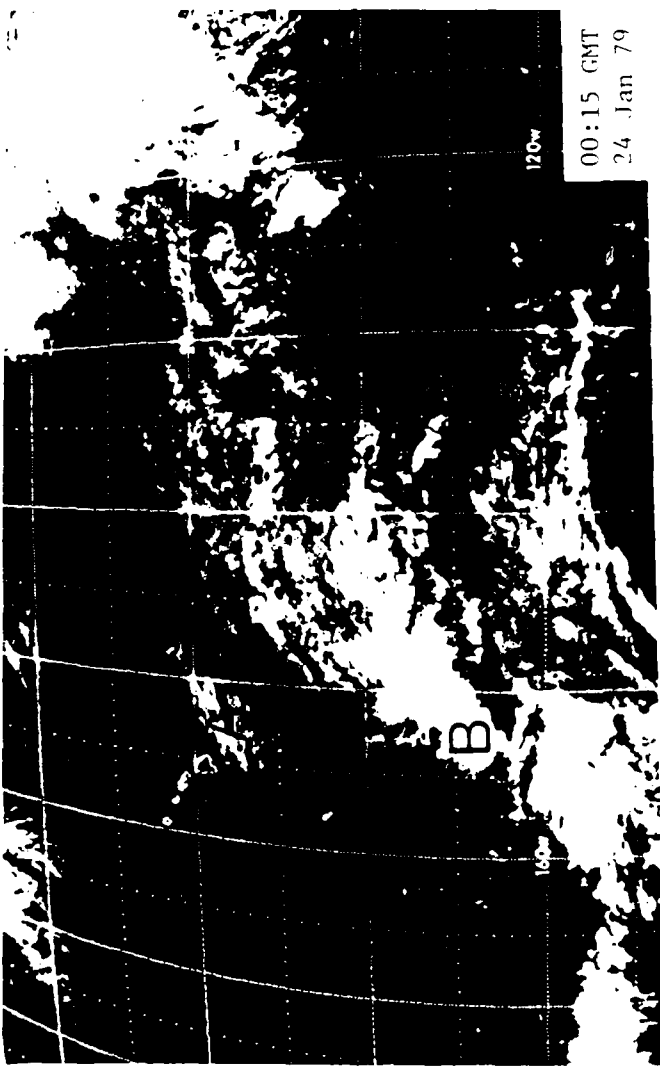


Fig. 27. As in Fig. 20 except for 0015 GMT 24 January 1979.

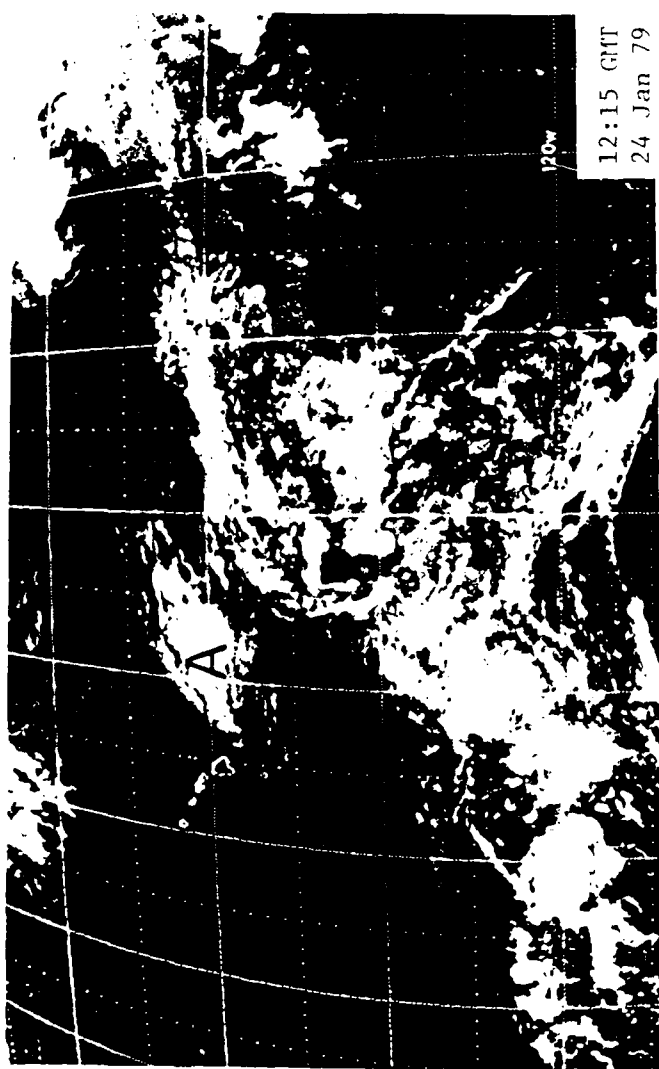


Fig. 28. As in Fig. 20 except for 1215 GMT 24 January 1979.

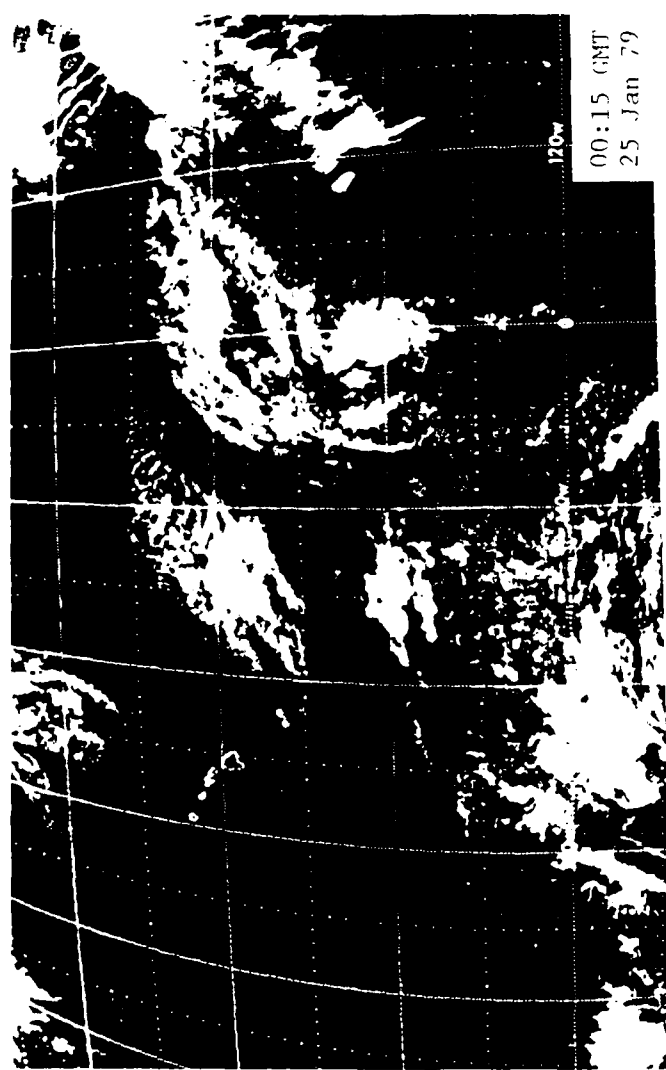


Fig. 29. As in Fig. 20 except for 0015 GMT 25 January 1979.

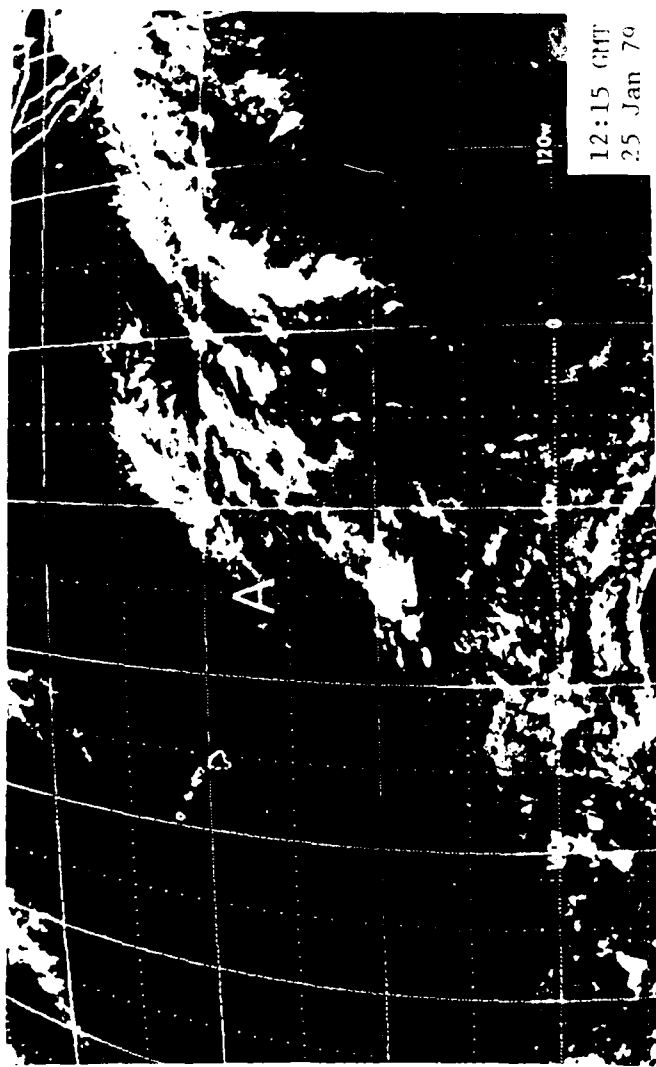


Fig. 30. As in Fig. 20 except for 1215 GMT 25 January 1979.

between 140°W to 150°W . The burst has regained some cohesion, a new convective source region, and is now the second burst.

Thirty-six hours later, a relatively small area of strong convection has developed at $8^{\circ}\text{N}/140^{\circ}\text{W}$ at 0000 GMT on the 27th (Fig. 31). This area is rather typically short-lived and is gone by 1200 GMT on the 27th (Fig. 32). The moisture burst now has about a 40° counterclockwise turning in the region where the source was previously located. This turning suggests a wind shift at this location, possibly associated with a trough line related to the original formation of the convective region with the favored location of development being the equatorward side of the subtropical jet stream entrance region (Whitney, 1977).

The clouds are breaking up by 0000 GMT on the 28th (Fig. 33); but new activity begins to form at $7^{\circ}\text{N}, 130^{\circ}\text{W}$ at 1200 GMT (Fig. 34); this activity is the beginning of a new third moisture burst even farther east than the previous two.

There are two major points that are brought out in this study of the satellite imagery. The first is the non-homogeneity over time and space of the cloud features of the moisture bursts studied. Neither one of the bursts was one single cloud type, cloud mass, or continuous convective region. In the first burst there were possibly as many as four different features in the clouds that all came together to actually form the burst. These features were: 1) the rapid appearance of cirrus clouds southeast of Hawaii; 2) the convective region to the east-northeast of Hawaii; 3) the remnants of the moisture burst that had already ceased to fulfill the requirements to actually be called a moisture burst, and; 4) the connection with the ITCZ.

The second major point is the almost continuous existence of moisture burst. The convective source region for the first burst disappears and a new convective

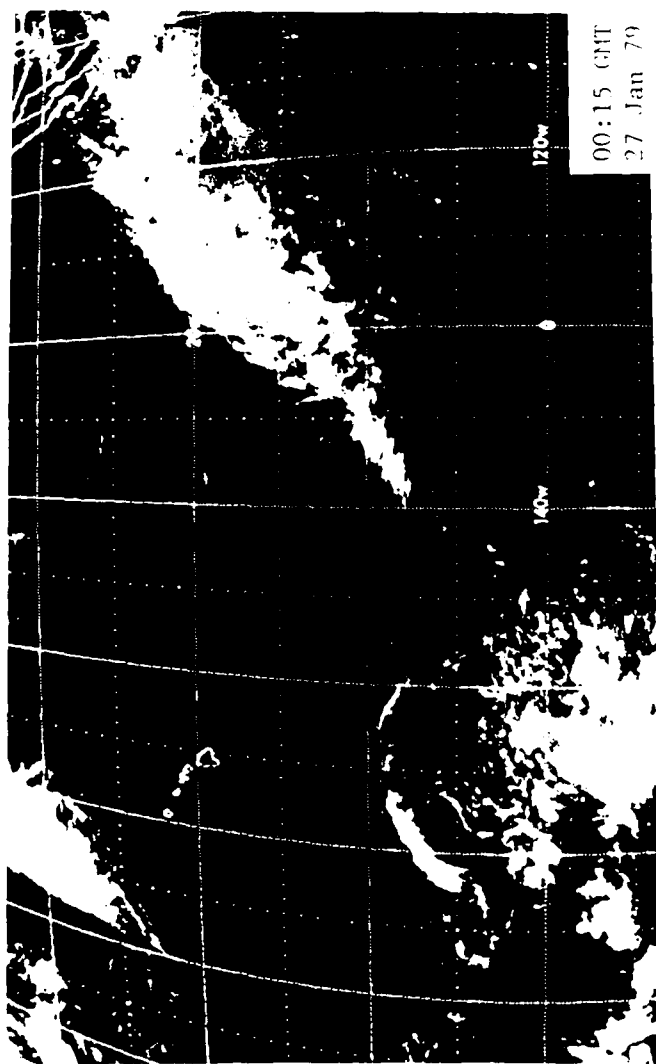


Fig. 31. As in Fig. 20 except for 0015 GMT 27 January 1979.

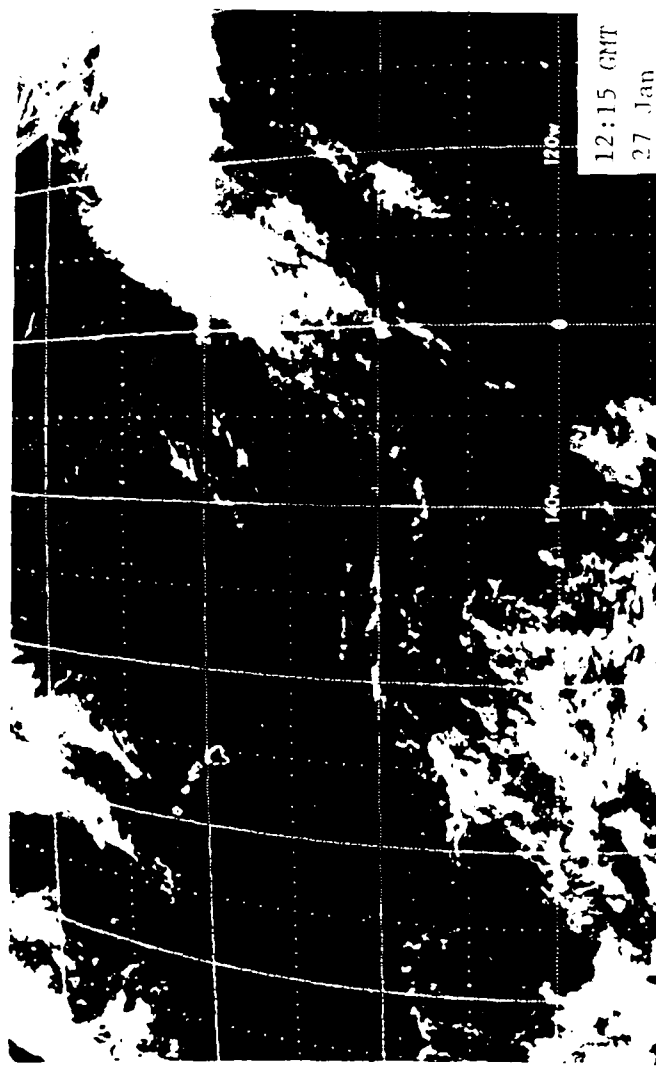


Fig. 32. As in Fig. 20 except for 1215 GMT 27 January 1979.

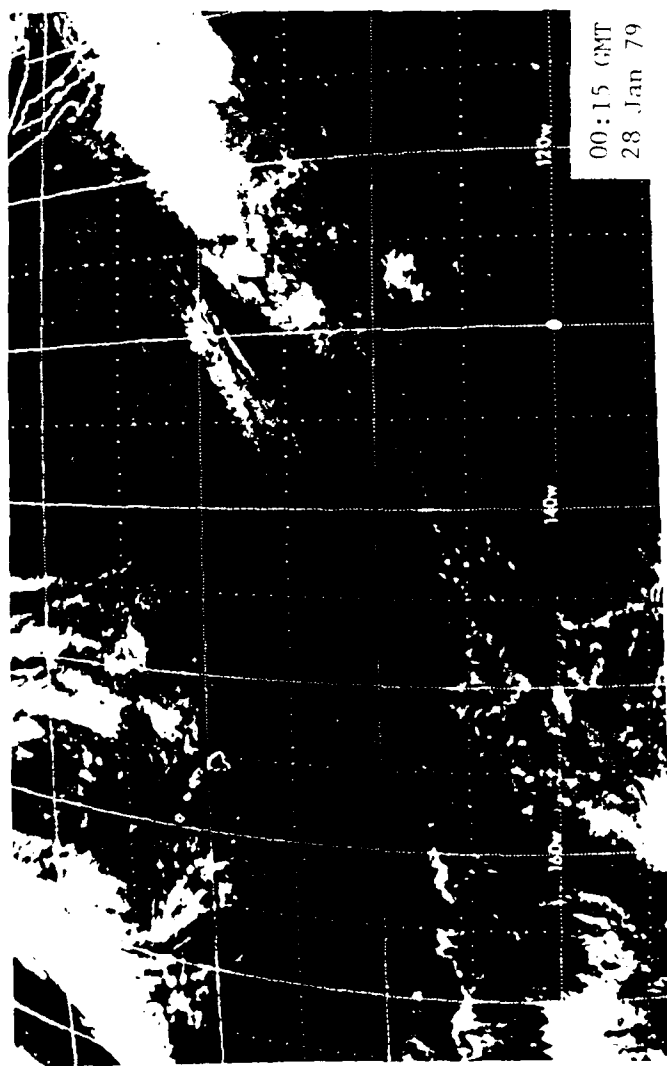


Fig. 33. As in Fig. 20 except for 0015 GMT 28 January 1979.

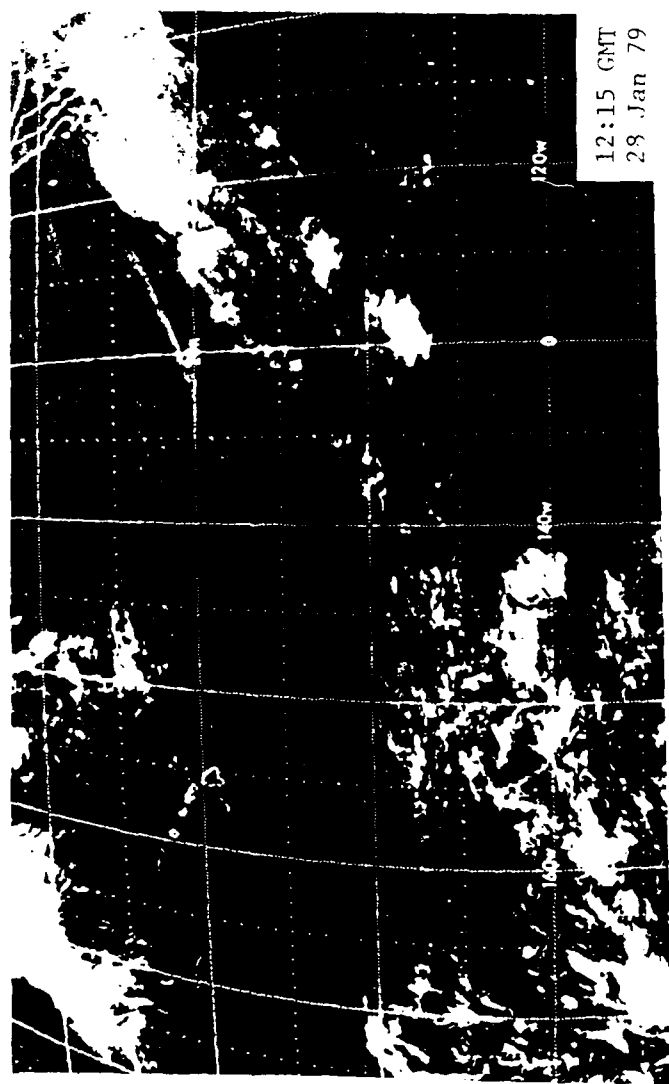


Fig. 34. As in Fig. 20 except for 1215 GMT 28 January 1979.

source region generates farther east, and therefore we call it two bursts, but still it seems to be almost one continuous phenomenon. The first burst itself developed along the axis of another burst, and a fourth burst was evolving in the same general region at the termination of the case study.

This section also showed that the areas exhibiting high moisture variability at upper levels correspond to the regions that are cloudy. Comparison of the maps of Chapter 3 with the satellite pictures so far discussed in this chapter suggest that the area of high temperature variability in the lower layers is an area that is commonly convectively active. The area of high temperature variability in the upper layers lies to the northwest of the majority of the cloud activity.

To summarize, to this point, the cloudy regions of the moisture bursts are highly variable in moisture content, in cloud type, and mesoscale cloud structure. Along the burst axis, the regions dominated by convective activity also exhibit amplified lower tropospheric temperature variability. High temperature variability also exists to the north and west of the burst axis in the upper troposphere. Surprisingly, although the burst axis is also the axis of high moisture variability, it is not an axis of high thermal variability.

b. Wind analyses

The previous section discussed some of the implied patterns of the wind fields. This section uses FGGE IIIb wind analyses with FGGE IIb data superimposed. The keys for the different levels are shown in Fig. 35. The keys are identical except for the FGGE IIb wind speed arrow lengths. This was done to account for the different average wind speeds for the various levels. The FGGE IIIb times are 0000 GMT but the FGGE IIb data are for 2100 GMT to 0300 GMT. The individual observations are for the observation level nearest the appropriate level ± 50 mb.

| KEY: 850 mb | |
|-------------|------------|
| □ | RAWINSONDE |
| * | P1BAL |
| X | THOS RADAR |
| Y | THOS NAVAO |
| ○ | DROPSonde |
| ☒ | BALLOON |
| † | AIRCRAFT |
| ☒ | SAT WINDS |
| ◊ | OTHER |
| → | 15 M/S |

| KEY: 300 mb | |
|-------------|------------|
| □ | RAWINSONDE |
| * | P1BAL |
| X | THOS RADAR |
| Y | THOS NAVAO |
| ○ | DROPSonde |
| ☒ | BALLOON |
| † | AIRCRAFT |
| ☒ | SAT WINDS |
| ◊ | OTHER |
| → | 40 M/S |

Fig. 35. Keys for next 11 figures. Note that the only difference for 850 mb and 300 mb is the length of wind speed arrow.

The upper level thermal trough and associated jet stream were shown in the previous section to be important in the formation of the moisture burst. Therefore we begin with the 300 mb analyses. This level was chosen because the majority of the dropsondes did not go as high as 200 mb. Fig. 36 shows 300 mb winds for 0000 GMT on 21 January 1979. It is obvious that both the FGGE IIIb analysis and the FGGE IIb observations point to a sharp trough from about $30^{\circ}\text{N}/145^{\circ}\text{W}$ to $11^{\circ}\text{N}/170^{\circ}\text{W}$ (actually, of course, it extends beyond both borders, but the discussion will be confined to the borders of the mappings). There is also a line of maximum counter-clockwise curvature extending from about $5^{\circ}\text{N}/154^{\circ}\text{W}$ to $10^{\circ}\text{S}/144^{\circ}\text{W}$. This curvature results in some northward meridional flow across the equator from about 130°W to 150°W . At this time the majority of the FGGE IIb data agrees reasonably well with the FGGE IIIb analysis. There are some observations that are probably in error, such as the pibal observation at $21^{\circ}\text{N}/157^{\circ}\text{W}$ showing northerly winds of about 50 ms^{-1} . The aircraft wind observations also are generally faster than the FGGE IIIb wind speeds. Along the eastern side of the trough the aircraft observations agree well in direction, but the speeds are generally 40 ms^{-1} and faster while the FGGE IIIb has only one area of greater than 40 ms^{-1} at about $19^{\circ}\text{N}/151^{\circ}\text{W}$.

By the 22nd (Fig. 37), the trough is sharper, and the wind speeds have increased on the east side. The FGGE IIIb wind analysis has a large area of speeds in excess of 48 ms^{-1} along the east side of the trough extending eastward to 120°W . Also there are several aircraft observations in this region recording speeds of over 60 ms^{-1} . There are three dropsonde wind reports between $12^{\circ}\text{N}/153^{\circ}\text{W}$ and $7^{\circ}\text{N}/151^{\circ}\text{W}$ that have strong southerly winds. They do not agree with the FGGE IIIb analysis. This does not mean they are wrong, as they do agree with the rapid

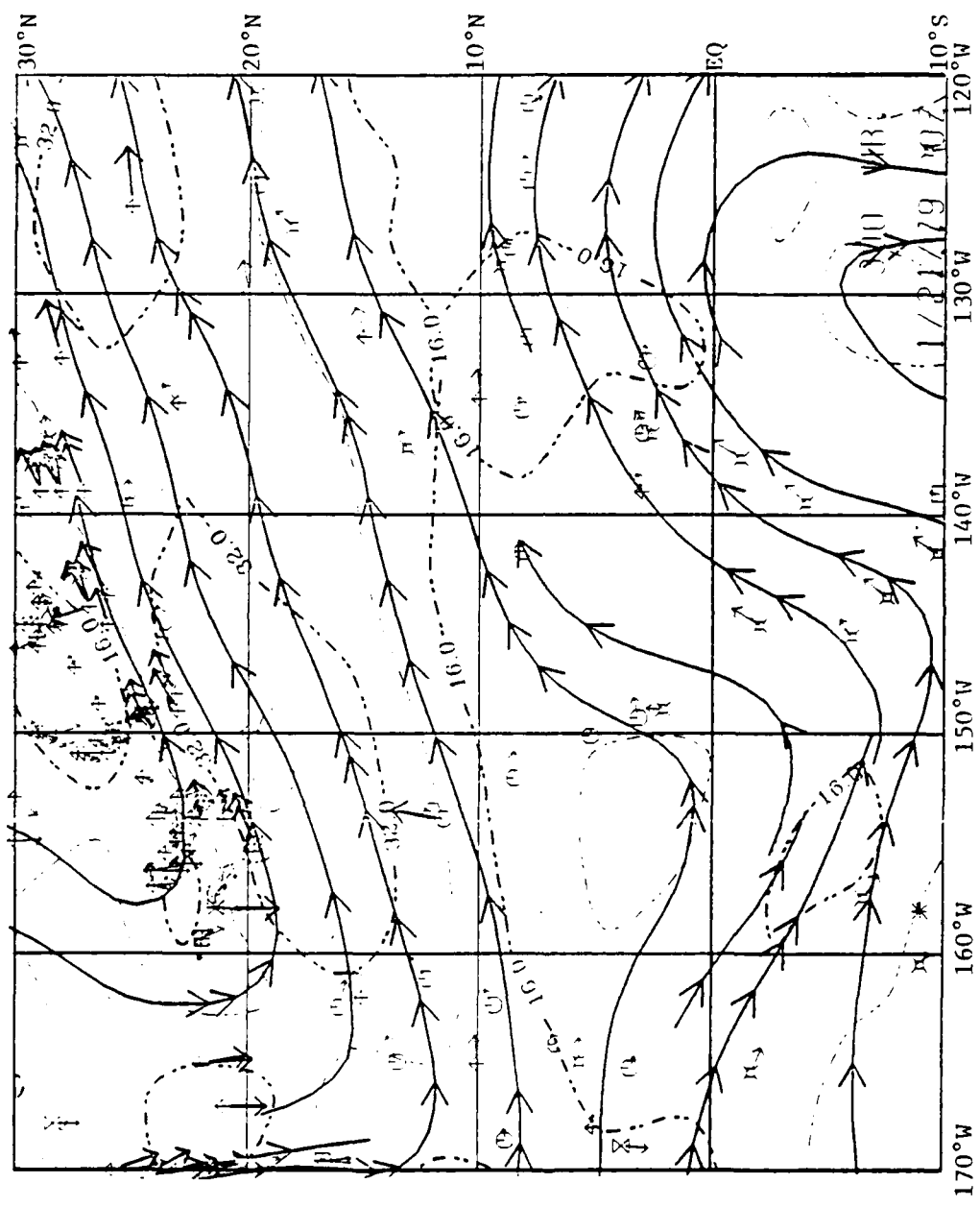


Fig. 36. 300 mb FGGE IIb streamline (solid lines) and isotach (dashed lines in ms^{-1}) fields for 0000 GMT 21 January 1979. Superimposed on this are the FGGE IIb actual observations. Key is found in Fig. 35.

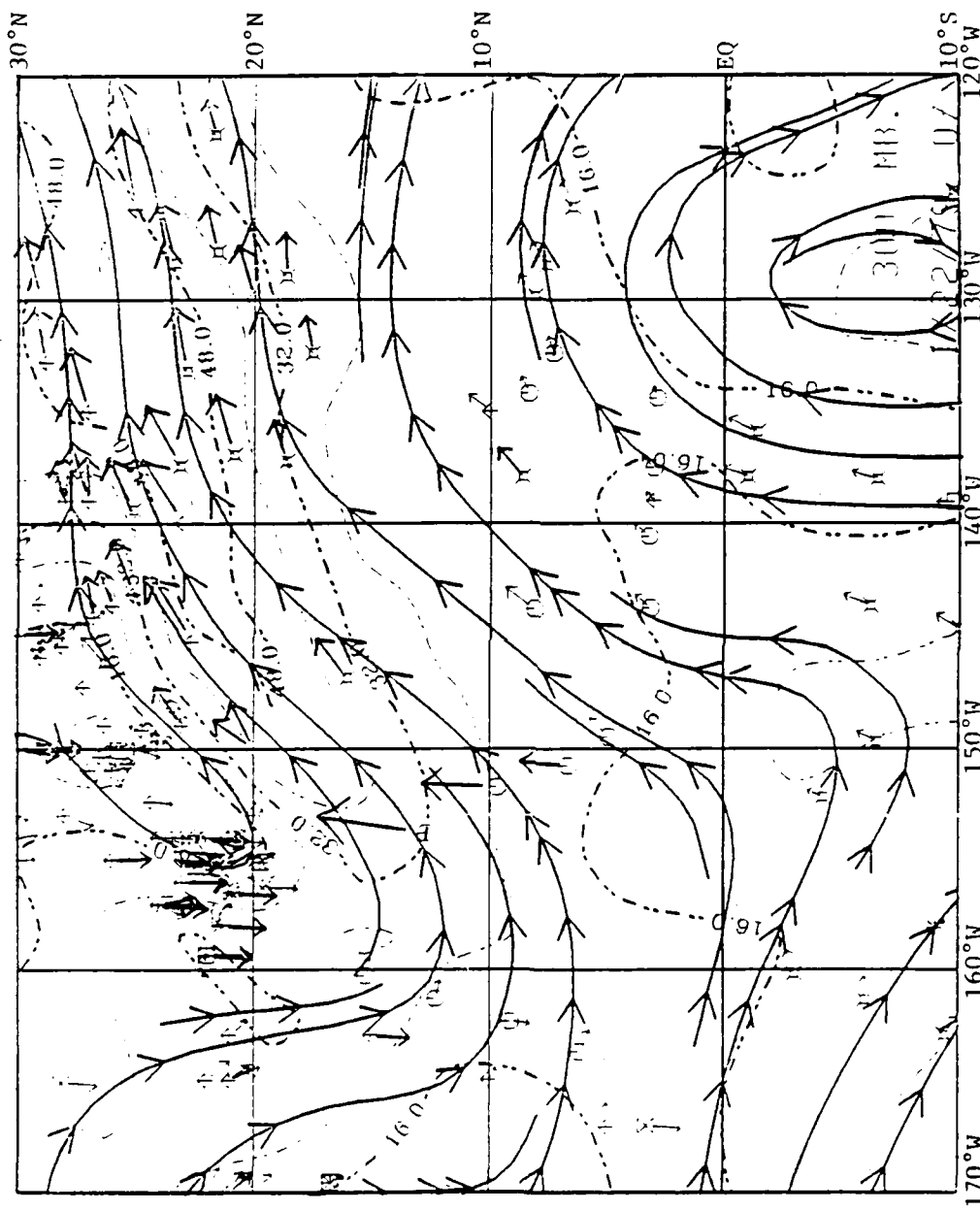


Fig. 37. As in Fig. 36 except for 0000 GMT 22 January 1979.

development and movement of 400 mb cirrus observed in the satellite film loops discussed in the previous section. If they are correct they indicate an extremely large meridional component to the winds in the area just to the northeast of the burst origin region. The line of maximum counter-clockwise circulation extending into the southern hemisphere continues to create cross-equatorial flow from the SPCZ around 150° W.

The northern hemisphere trough weakens by the 23rd (Fig. 38), but has combined with the southern hemisphere system to become a large region of counter-clockwise curvature with an axis line extending from north of 30° N/ 157° W to south of 10° S/ 160° W. The region of maximum winds is now located further downstream with wind speeds in excess of 64 ms^{-1} around 26° N/ 130° W. Several aircraft recorded speeds greater than 80 ms^{-1} .

On the 24th (Fig. 39), there is a new trough line running from north of Hawaii to southwest of 8° N/ 170° W. This new trough indicates that the model is generating short wave troughs on the long wave system. As the new short wave is generated the old one is dissipated on the eastern side of the long wave trough. The trough at this time is not very strong, with the strongest winds still well east of the trough.

The trough progresses eastward and by the 25th (Fig. 40) the axis extends from north of 30° N/ 145° W to 10° N/ 155° W and another line of maximum counter-clockwise curvature extending from 8° N/ 163° W into the southern hemisphere. The origin region for the second burst is about 7° N/ 144° W which is just east of the trough at this time. The trough line progresses rapidly eastward and by the 26th (Fig. 41) is from north of 30° N/ 141° W to about 8° N/ 145° W with observed wind speeds of almost 40 ms^{-1} along the bottom of the trough. The large wind speeds downstream from the trough continued with observed wind speeds in excess of 50 ms^{-1} .

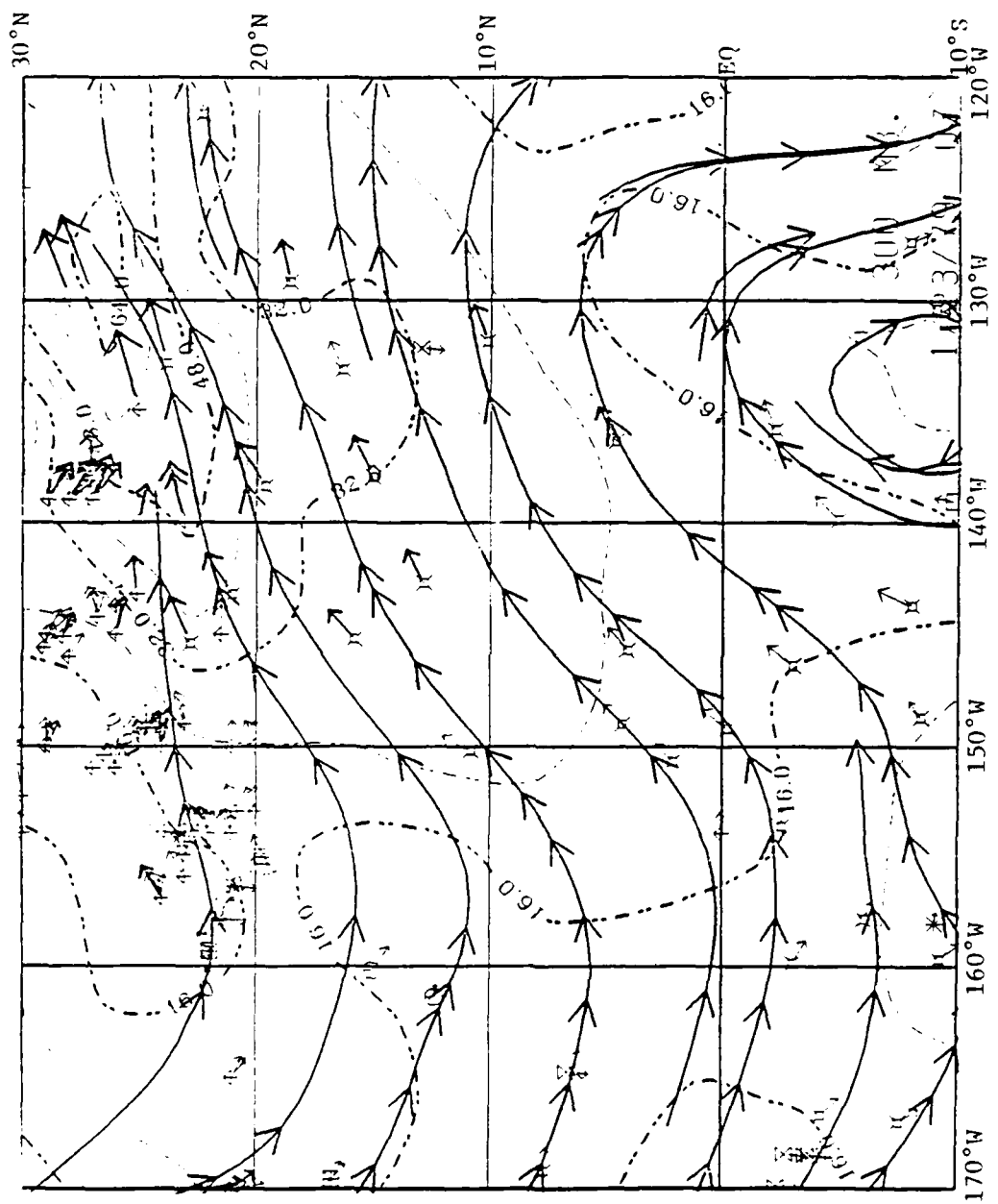


Fig. 38. As in Fig. 36 except for 0000 GMT 23 January 1979.

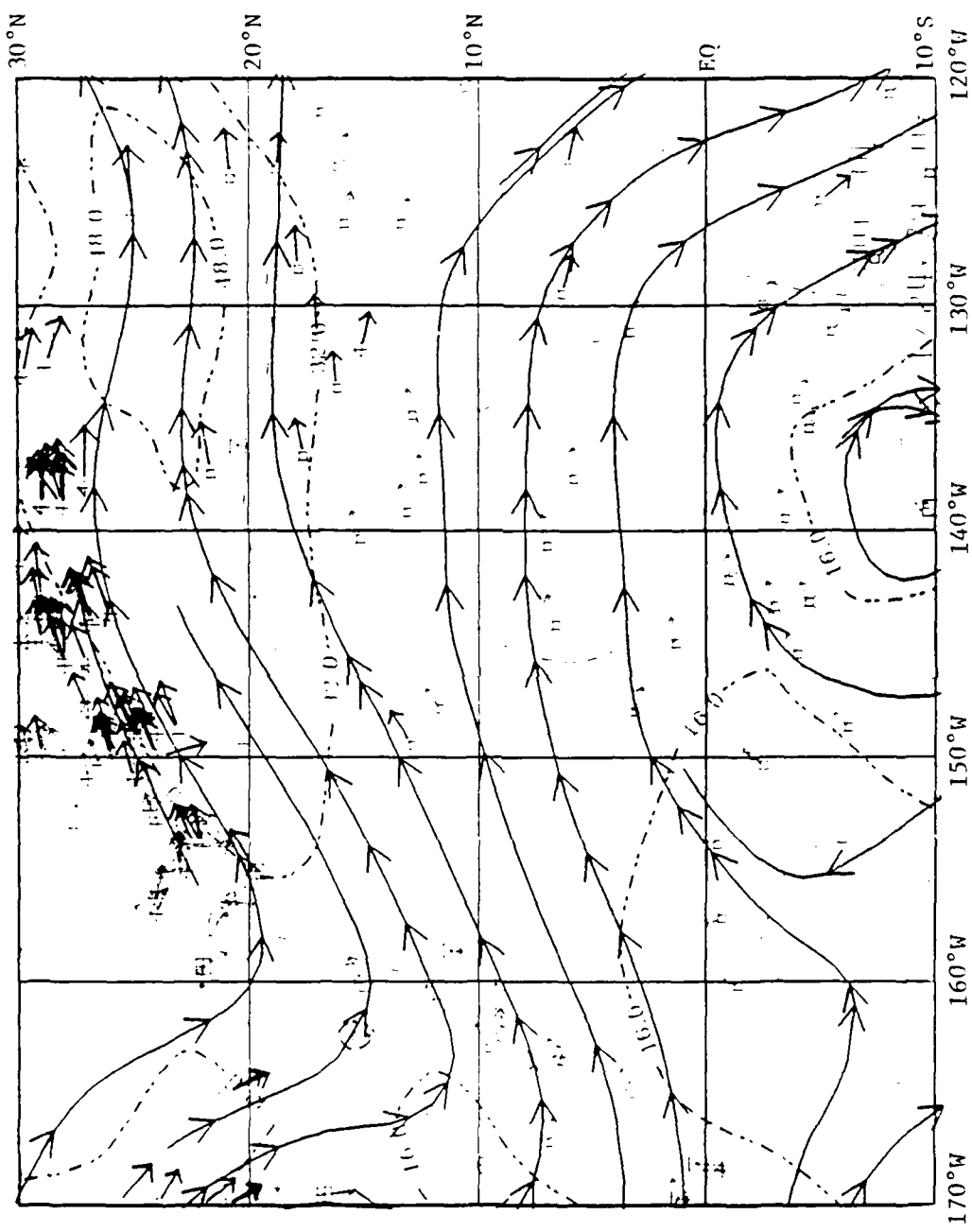
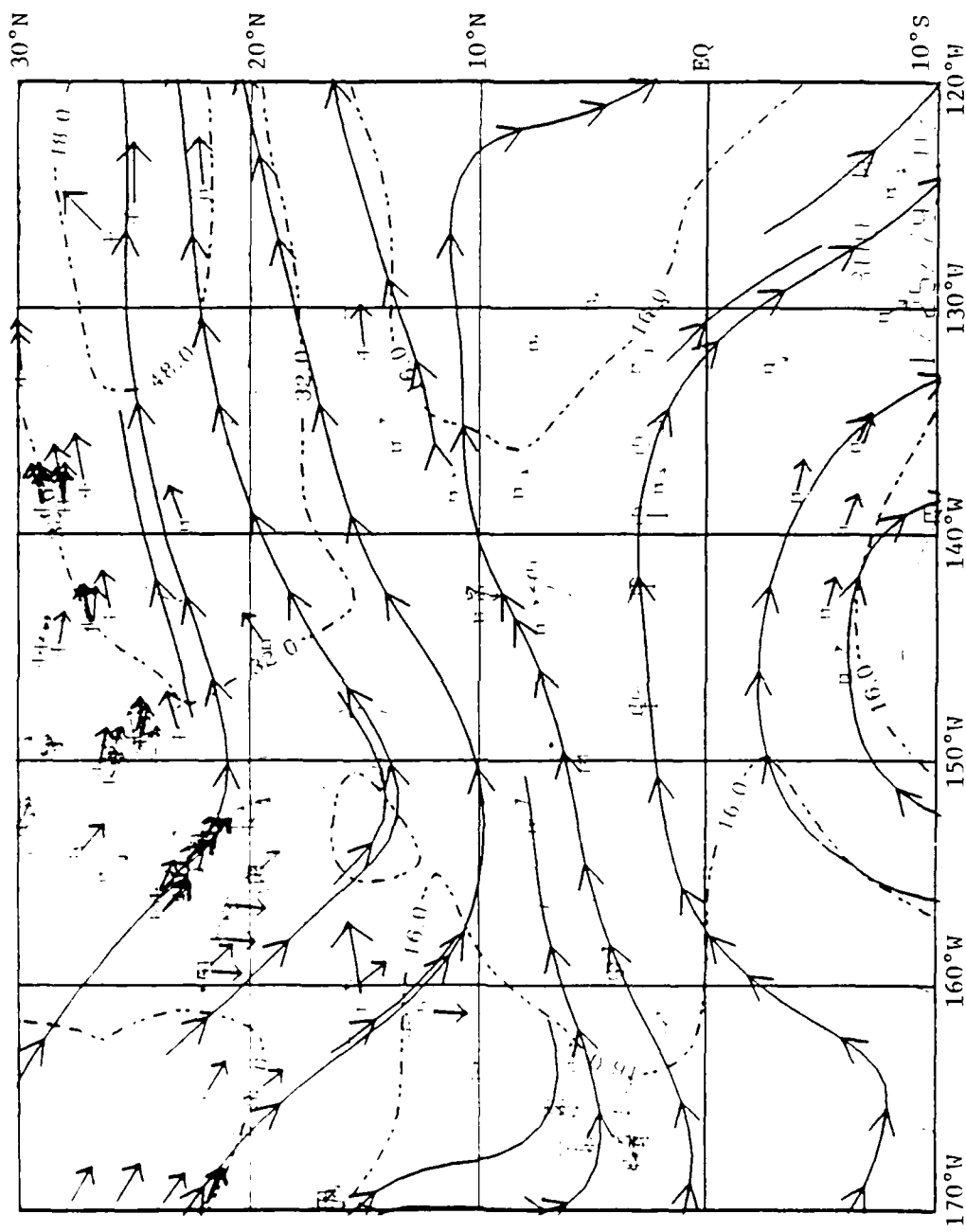


Fig. 39. As in Fig. 36 except for 0000 GMT 24 January 1979.



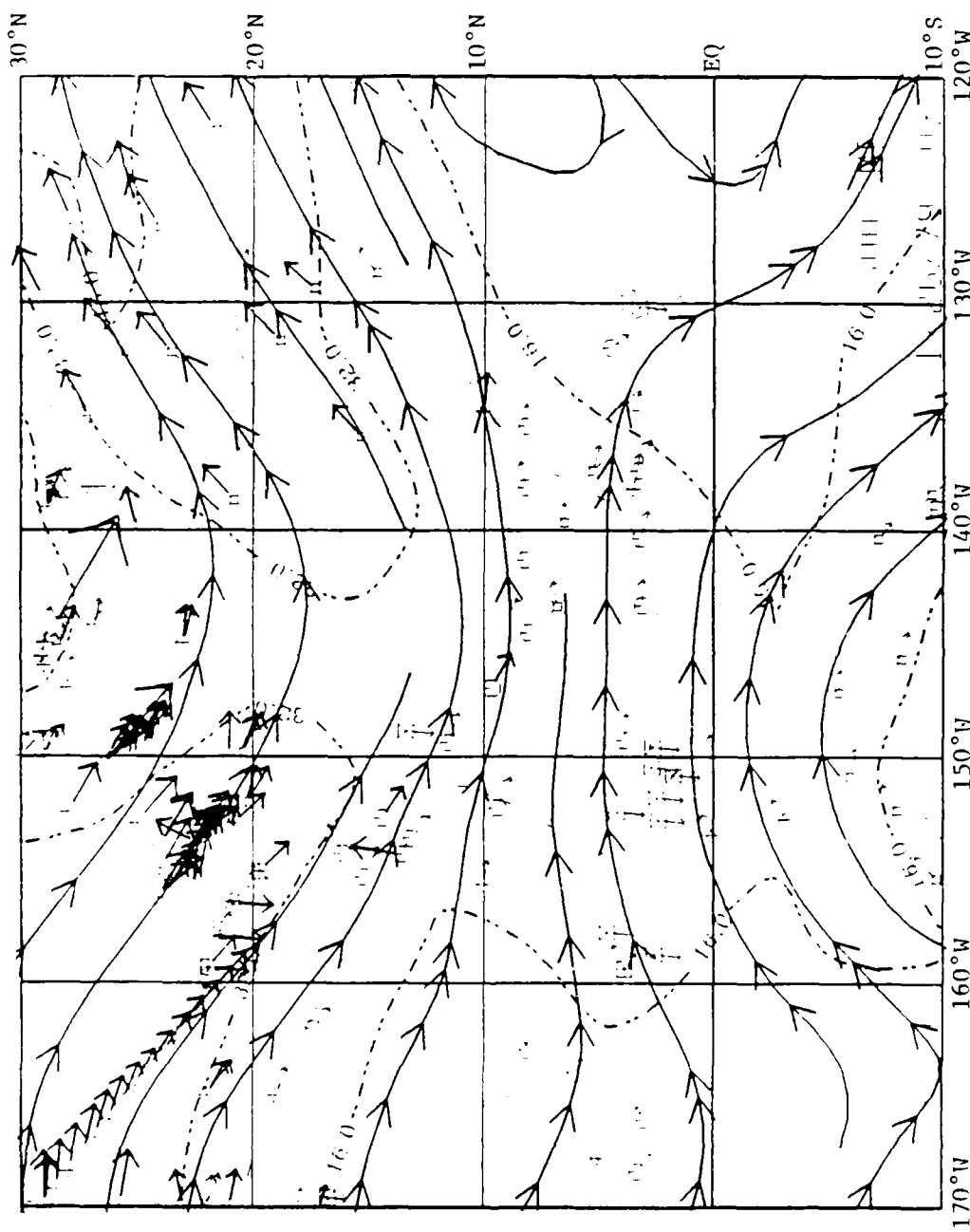


Fig. 41. As in Fig. 36 except for 0000 GMT 26 January 1979.

The trough continues moving to the east along with the large wind speeds until by the 29th (not shown) the trough is east of 120°W and the flow in the region of interest is nearly zonal.

The 850 mb level has fewer FGGE IIb data available. There are fewer satellite cloud drift winds available due in part to the amount of upper level clouds masking the lower clouds. Also there are fewer aircraft observations at this level.

On the 21st (Fig. 42) there is an area of counter-clockwise circulation on the equator centered at about 155°W . This results in a trough line northward from this point to around $25^{\circ}\text{N}/150^{\circ}\text{W}$. This trough resembles an easterly wave, although movement at this time is undefined. The pattern in the northeast area seems due mostly to lack of data. The data agree with the analysis, but other interpretation is possible. The aircraft dropsonde wind observations in the region of $10^{\circ}\text{N}/160^{\circ}\text{W}$ are inconsistent with the analysis and questionable.

By the 22nd (Fig. 43) the counter-clockwise rotation area moved very little. The associated northern hemisphere trough is also almost stationary. The ridgeline from the high pressure area at about $17^{\circ}\text{N}/125^{\circ}\text{W}$ has pushed westward and the trough is sharper. There is now a col point at about $20^{\circ}\text{N}/143^{\circ}\text{W}$, which results in a region of confluence at about $19^{\circ}\text{N}/150^{\circ}\text{W}$.

The region of counter-clockwise rotation moves northwest and by the 23rd (Fig. 44) is centered at about $6^{\circ}\text{N}/159^{\circ}\text{W}$. The northern portion of the trough has apparently moved little, although with the lack of time continuity there is a possibility that this is not the same trough. It is interesting to note that for this time there are virtually no observations east of 150°W . In spite of this the FGGE IIb model generated a high pressure center where the neutral point was 24 h before.

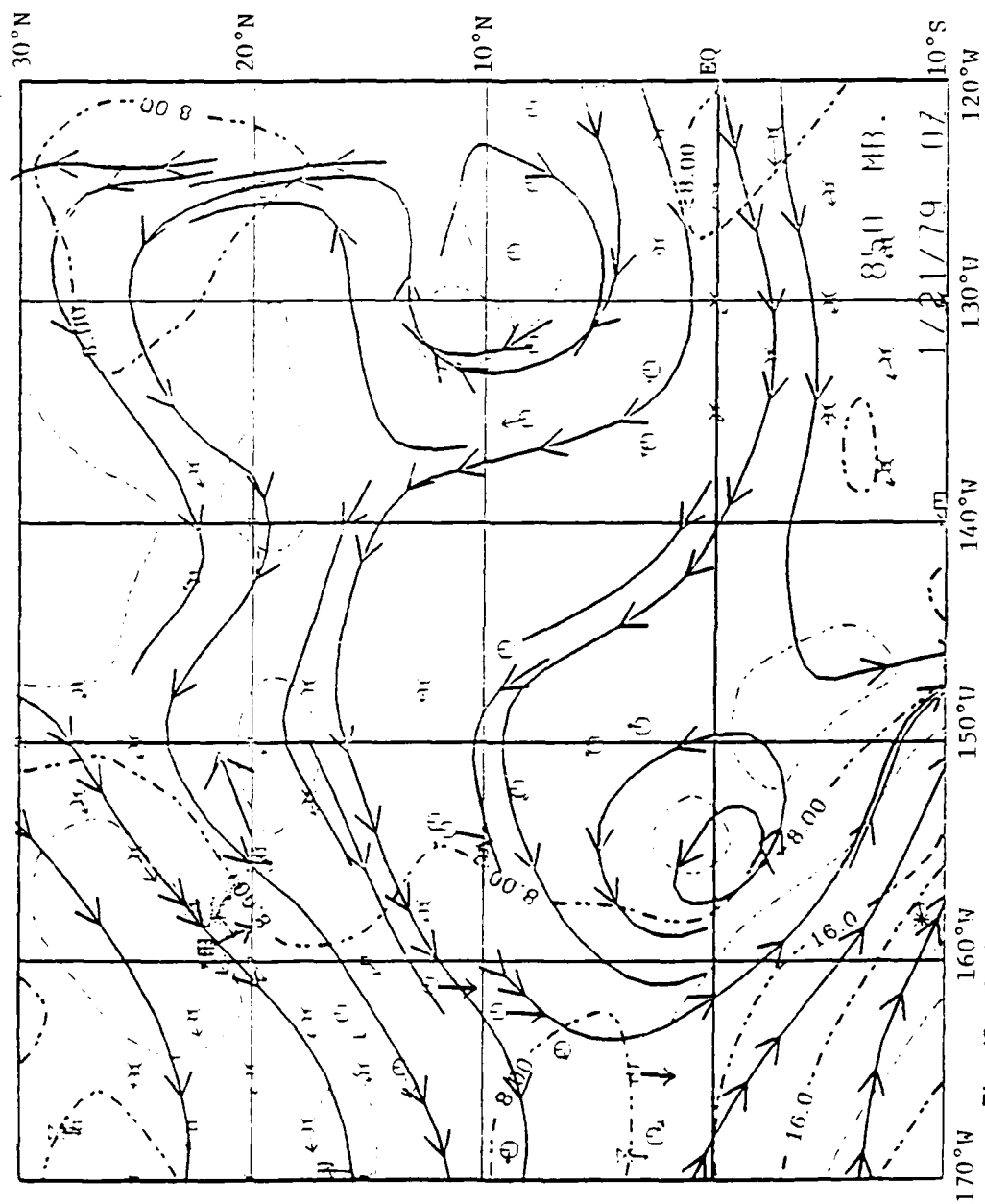


Fig. 42. As in Fig. 36 except for 850 mb at 0000 GMT 21 January 1979.

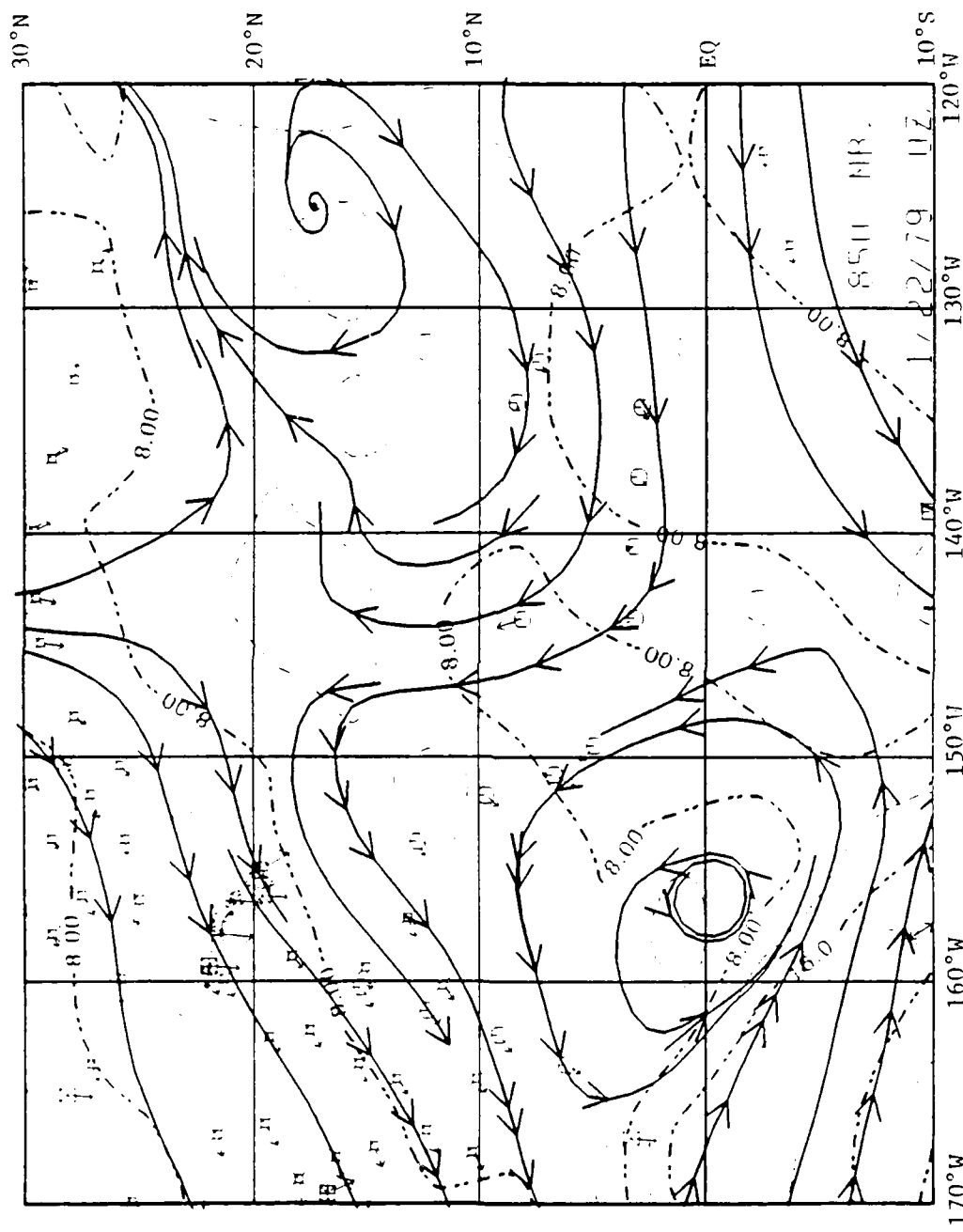


Fig. 43. As in Fig. 36 except for 850 mb at 0000 GMT 22 January 1979.

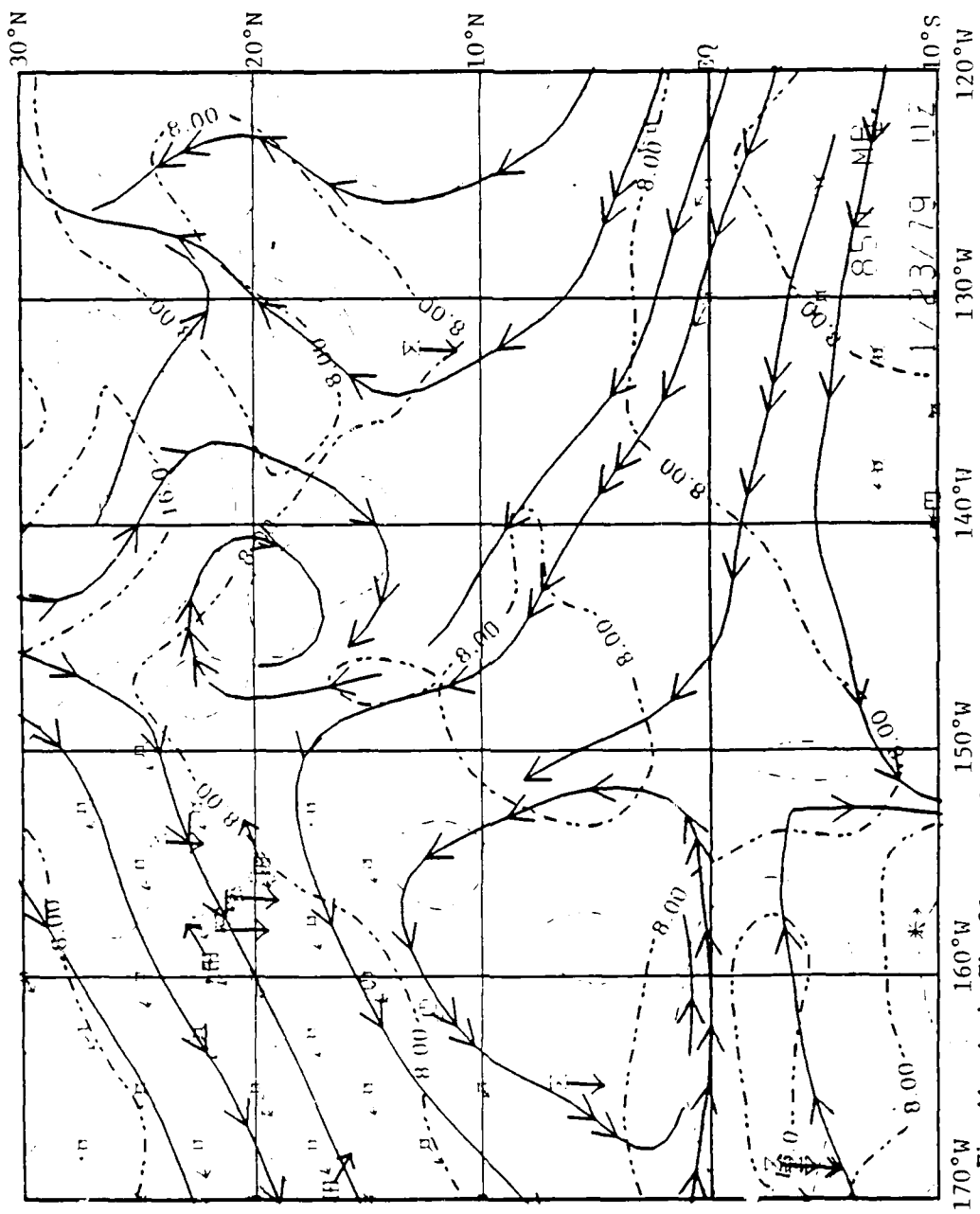


Fig. 44. As in Fig. 36 except for 850 mb at 0000 GMT 23 January 1979.

By the 24th (Fig. 45) there is an area of strong convergence centered at about $17^{\circ}\text{N}/146^{\circ}\text{W}$. The confluent area is within the cloudy region of the first burst, as is the cyclonic circulation area to the west. There are few observations available to confirm the convergence region but there are several that support the cyclonic circulation region.

On the 25th (not shown) the area of confluence shifted slightly east, and the cyclonic circulation remained fairly stationary. By the 26th (Fig. 46) there is a new area of cyclonic circulation to the east at $13^{\circ}\text{N}/140^{\circ}\text{W}$, and the aircraft dropsonde wind observations seem to agree with the FGGE IIIb analysis.

After the 27th (not shown) the systems weaken, until by the 29th (not shown) the flow is nearly zonal easterlies between 20°N and 10°S .

Looking at both levels simultaneously in time sequence reveals several interesting facts. At 0000 GMT on 21 January 1979 near the origin time for the first moisture burst the 850 mb trough (Fig. 42) is to the east of the 300 mb trough (Fig. 36). The clouds form near the low level trough, and therefore to the east of the upper level trough. By the 22nd the low level trough moved slowly west, while the upper level trough moved east resulting in a nearly vertical trough axis. The previous section on satellite interpretation showed this to be the time when and place where the first burst rapidly intensifies. This is also the time when the upper level downstream wind speeds increased. This horizontal speed shear could be the outflow needed to allow increased convection related to the low level trough. As the upper level trough weakens the moisture burst is eventually separated from its origin region. A second upper level trough begins moving into the region and intensifying until its southeastern edge coincides with a region of low level convergence at about 0000 GMT on the 25th around the origin region of the second burst ($7^{\circ}\text{N}/144^{\circ}\text{W}$).

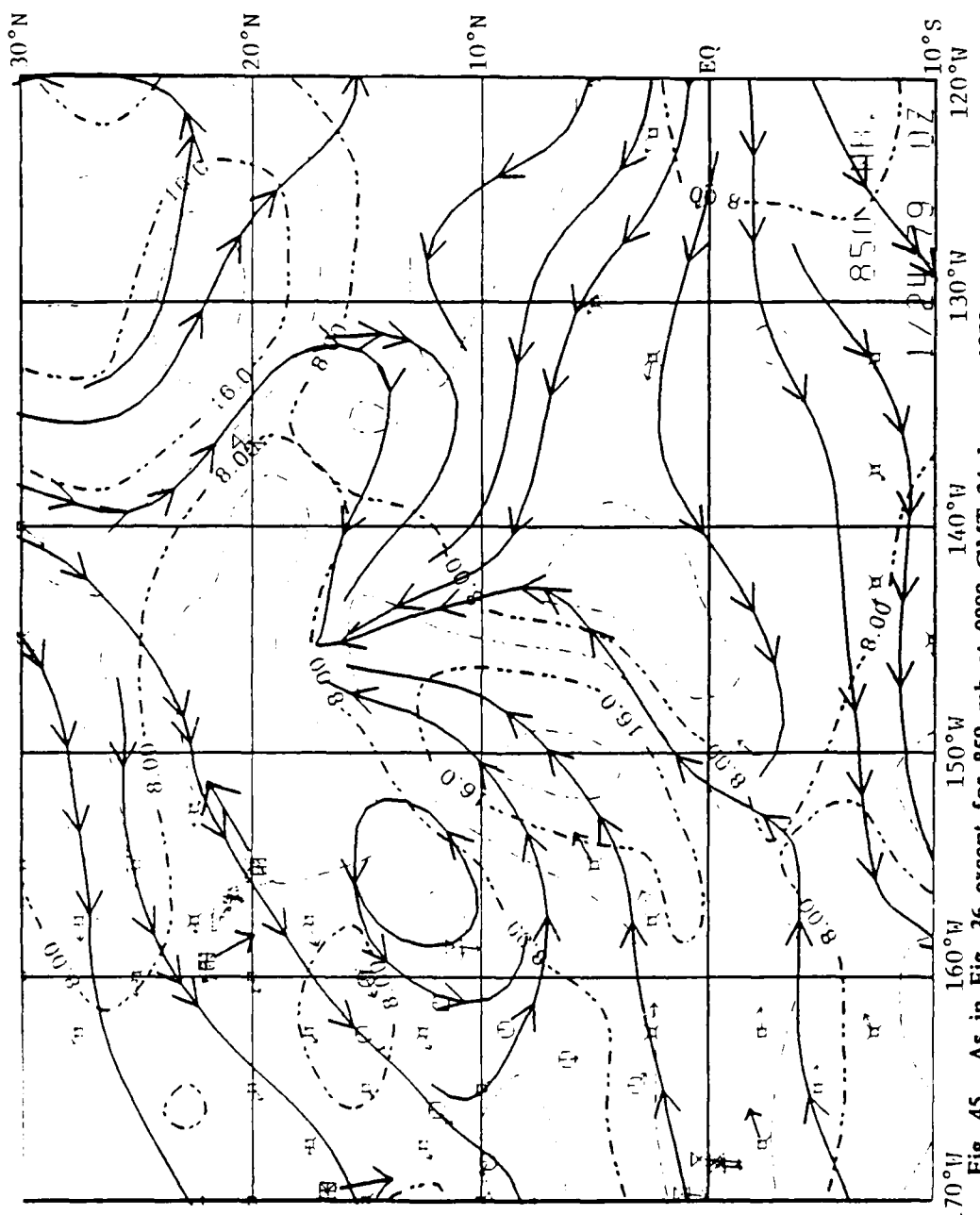


Fig. 45. As in Fig. 36 except for 850 mb at 0000 GMT 24 January 1979.

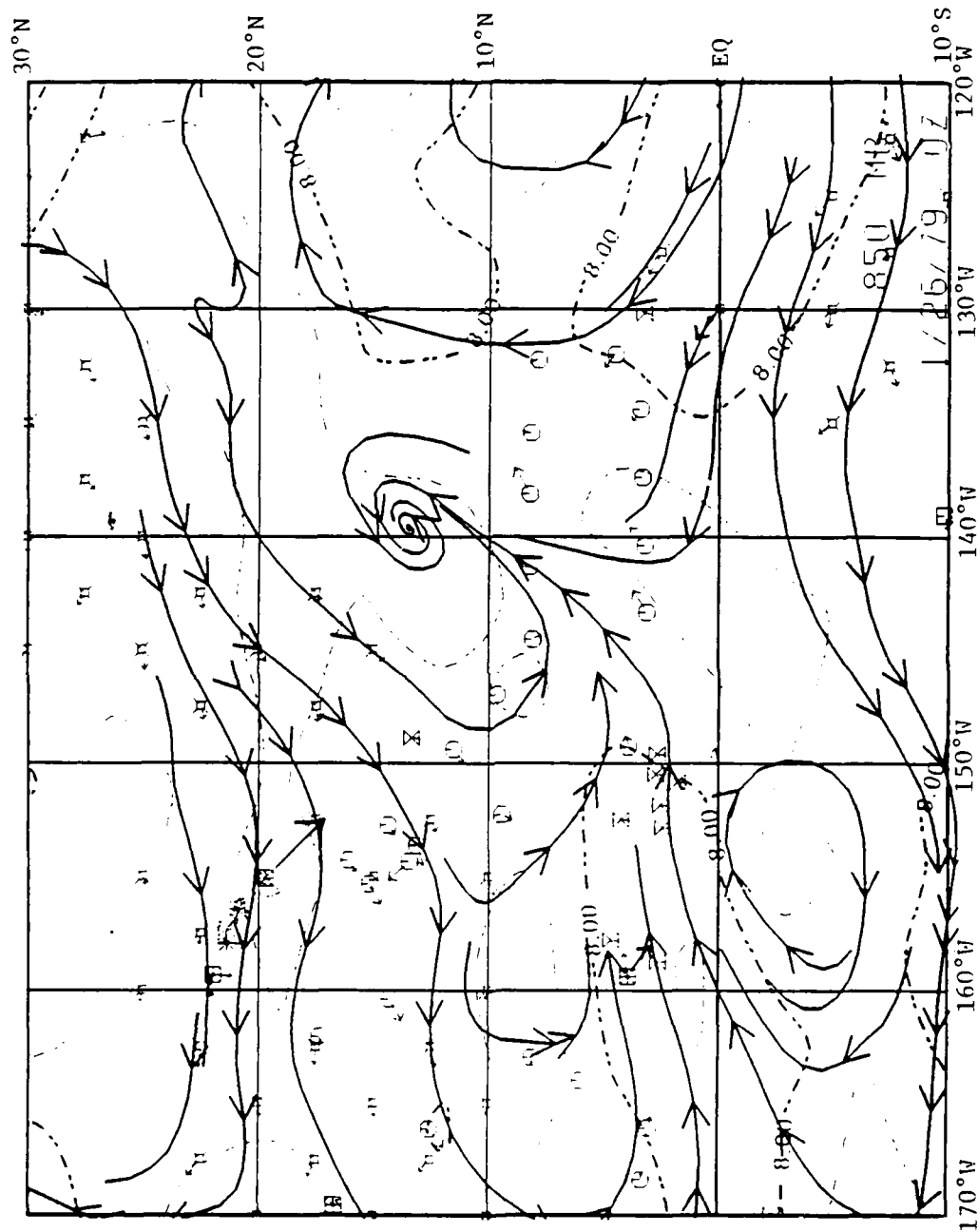


Fig. 46. As in Fig. 36 except for 850 mb at 0000 GMT 26 January 1979.

Therefore the low level pattern would seem important for the convergence of moist tropical air, and the upper level pattern provides the outflow to allow for not only the convection but also the transport of upper level moisture. These points are also discussed in Section 4d on FGGE IIIb moisture depictions.

c. Temperature changes

To study the subtle temperature patterns of the two moisture bursts, temperature time changes were computed and analyzed for the 300, 500, 700, 850 and 1000 mb surfaces. The 300 mb temperature changes are for 12 h time intervals to allow for better resolution, while the remaining levels, are for 24 h time intervals to eliminate diurnal fluctuations. The three middle levels were not found to have many significant signals, and are therefore not shown. The isotherms are drawn at 1°C intervals with "H" representing warming and "L" cooling.

The 24 h temperature change for 1000 mb for the time period ending 1200 GMT on the 21st (Fig. 47) has a large area of strong cooling centered at 10°N/150°W. There is also an area of warming centered at about 22°N/131°W. In the southern hemisphere there is a warming center at about 11°S/151°W and a cooling center just to the southeast.

Fig. 48 shows that the southern hemisphere warming expands across the equator and the northern hemisphere cooling area discussed previously has moved to the northeast. The northern hemisphere warming center remained almost stationary but intensified to almost 9°C for a 24 h change. This is a very large temperature change for a tropical oceanic region at this low a level.

The warming region that moved across the equator has intensified and by 1200 GMT on the 22nd (Fig. 49) is centered at about 7°N/150°W. It intensified to over 10°C of change in 24 h.

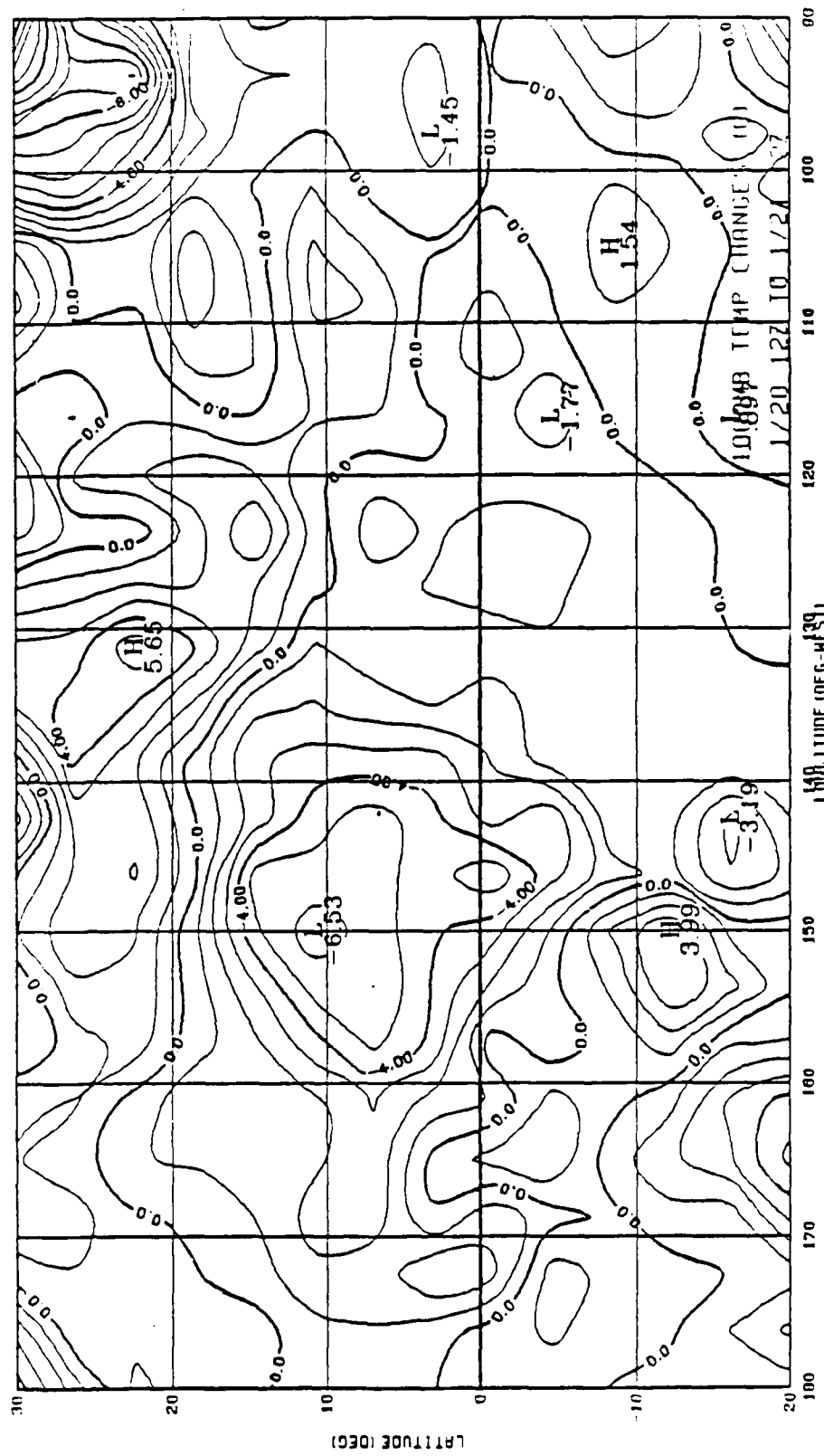


Fig. 47. FGGE IIIb 24 h temperature changes at 1000 mb for the period ending 1200 GMT 21 January 1979. Units are $^{\circ}$ C.

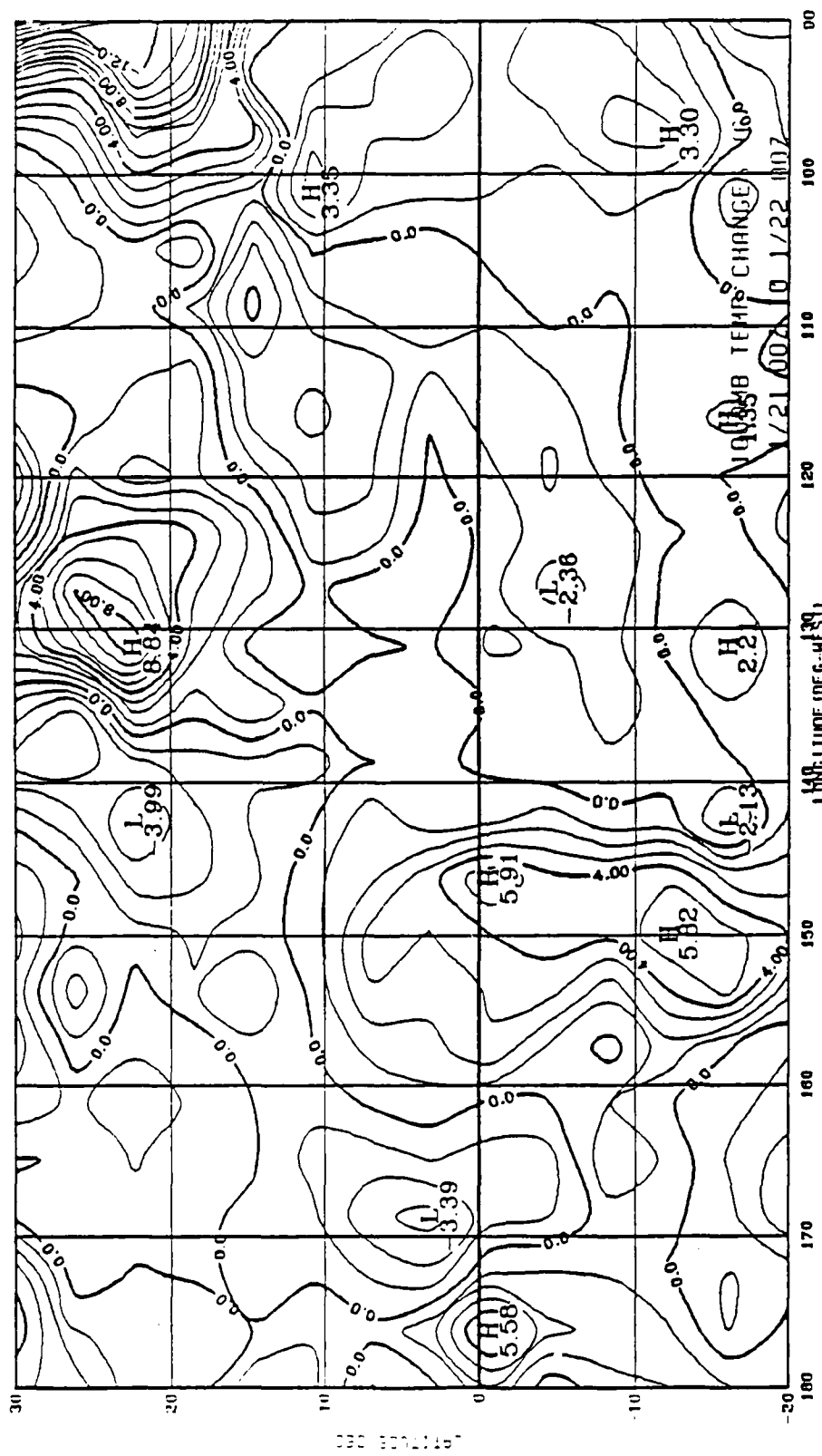


Fig. 48. As in Fig. 47 except for the period ending 0000 GMT 22 January 1979.

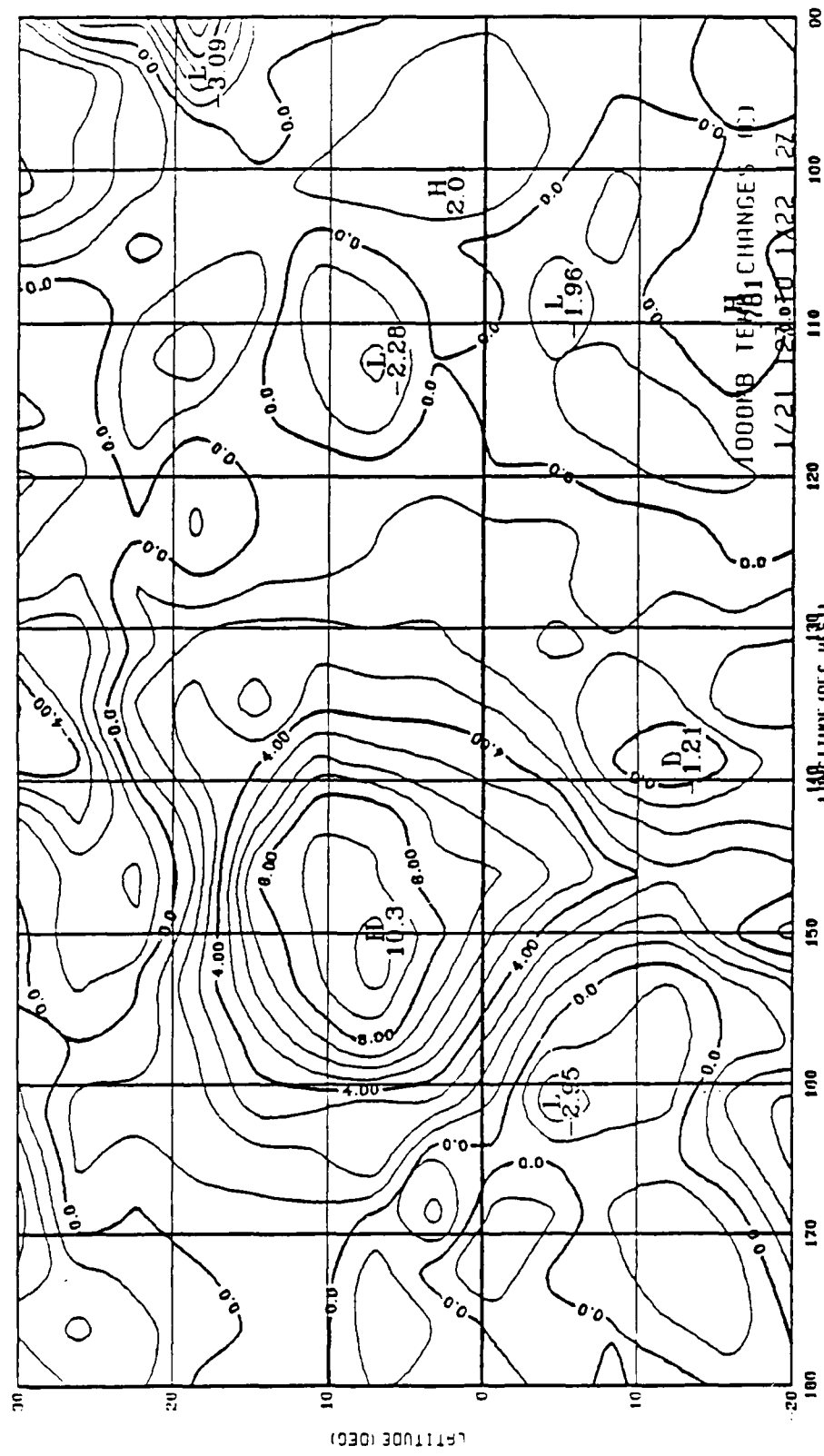


Fig. 49. As in Fig. 47 except for the period ending 1200 GMT 22 January 1979.

There is an interesting pattern evident on Fig. 50 for 1200 GMT on the 23rd. Along the moisture burst there are two areas of cooling and two areas of warming. Starting from the southwest the areas are: cooling at about $6^{\circ}\text{N}/155^{\circ}\text{W}$, warming at about $10^{\circ}\text{N}/143^{\circ}\text{W}$, cooling at about $20^{\circ}\text{N}/127^{\circ}\text{W}$, and warming at about $22^{\circ}\text{N}/116^{\circ}\text{W}$.

The southwestern warming area becomes a strong region of cooling at $10^{\circ}\text{N}/142^{\circ}\text{W}$ by 1200 GMT on the 24th (Fig. 51). This area is very strong with over 12°C of change. Alternate warming and cooling occur further downstream under the moisture burst.

For the remainder of the nine days the 1000 mb 24 h temperature changes become much smaller and show very little pattern. Therefore the analyses are not shown.

The 1000 mb 24 h temperature changes of course agree with the 1000 mb temporal standard deviation. The area of large deviations agrees with the band of large changes that prevails on the temperature change maps. This band is associated with the main axis of the first moisture burst.

The synoptic temperature changes are larger than climatologically expected and are due possibly to the FGGE IIIb model trying to reflect the intense convection in the burst region. Also one of the few data sources for the model at this level is satellite-derived temperatures, and at this level the channel may be highly contaminated by low level moisture and the sea surface.

At 300 mb the 12 h temperature change for the time ending 0000 GMT on the 21st (Fig. 52) shows an area of intense warming centered at $25^{\circ}\text{N}/128^{\circ}\text{W}$ and another at $21^{\circ}\text{N}/161^{\circ}\text{W}$. There also is a region of cooling at $22^{\circ}\text{N}/150^{\circ}\text{W}$. Twelve hours later (Fig. 53) the area of cooling continues in roughly the same

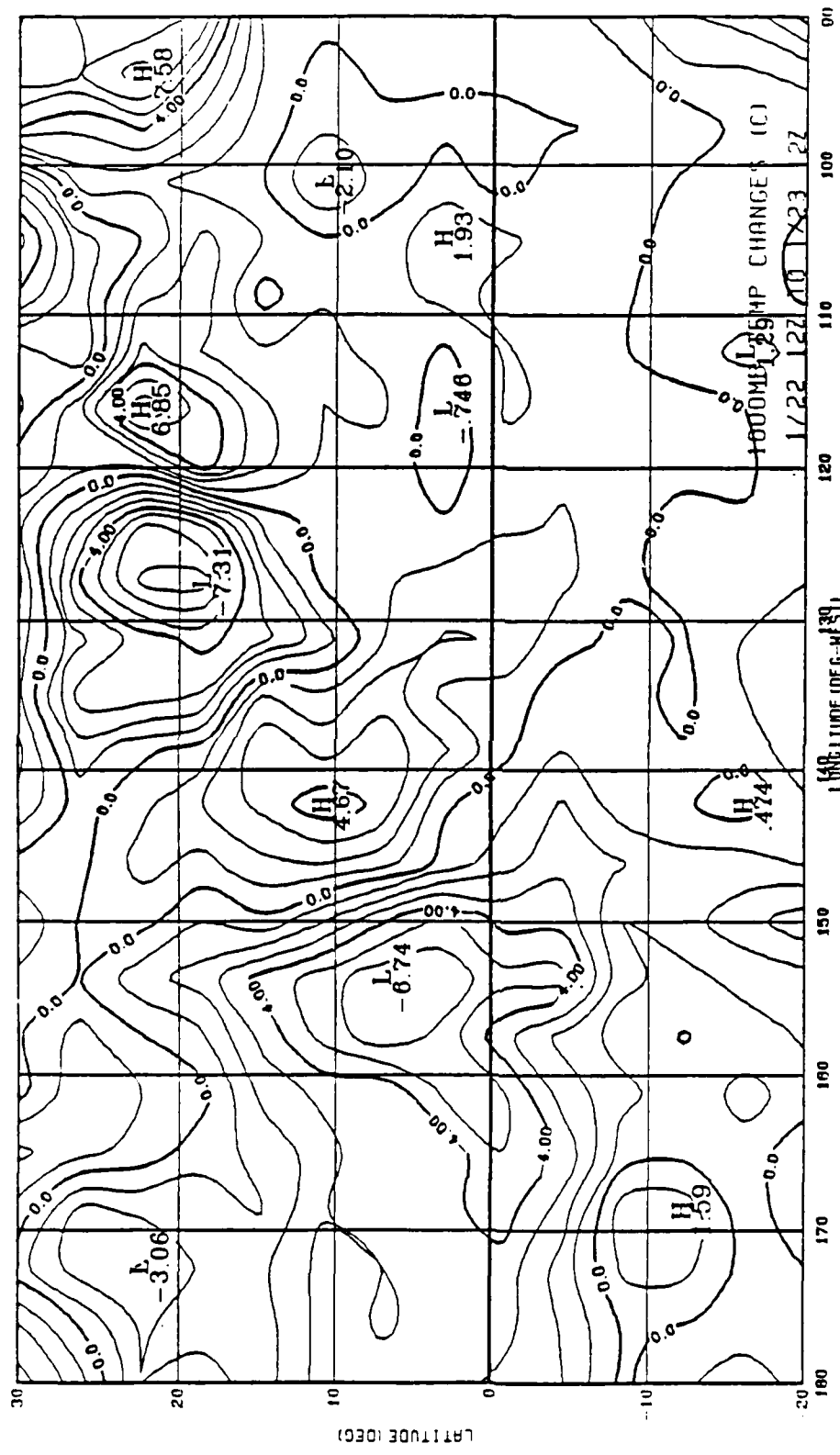


Fig. 50. As in Fig. 47 except for the period ending 1200 GMT 23 January 1979.

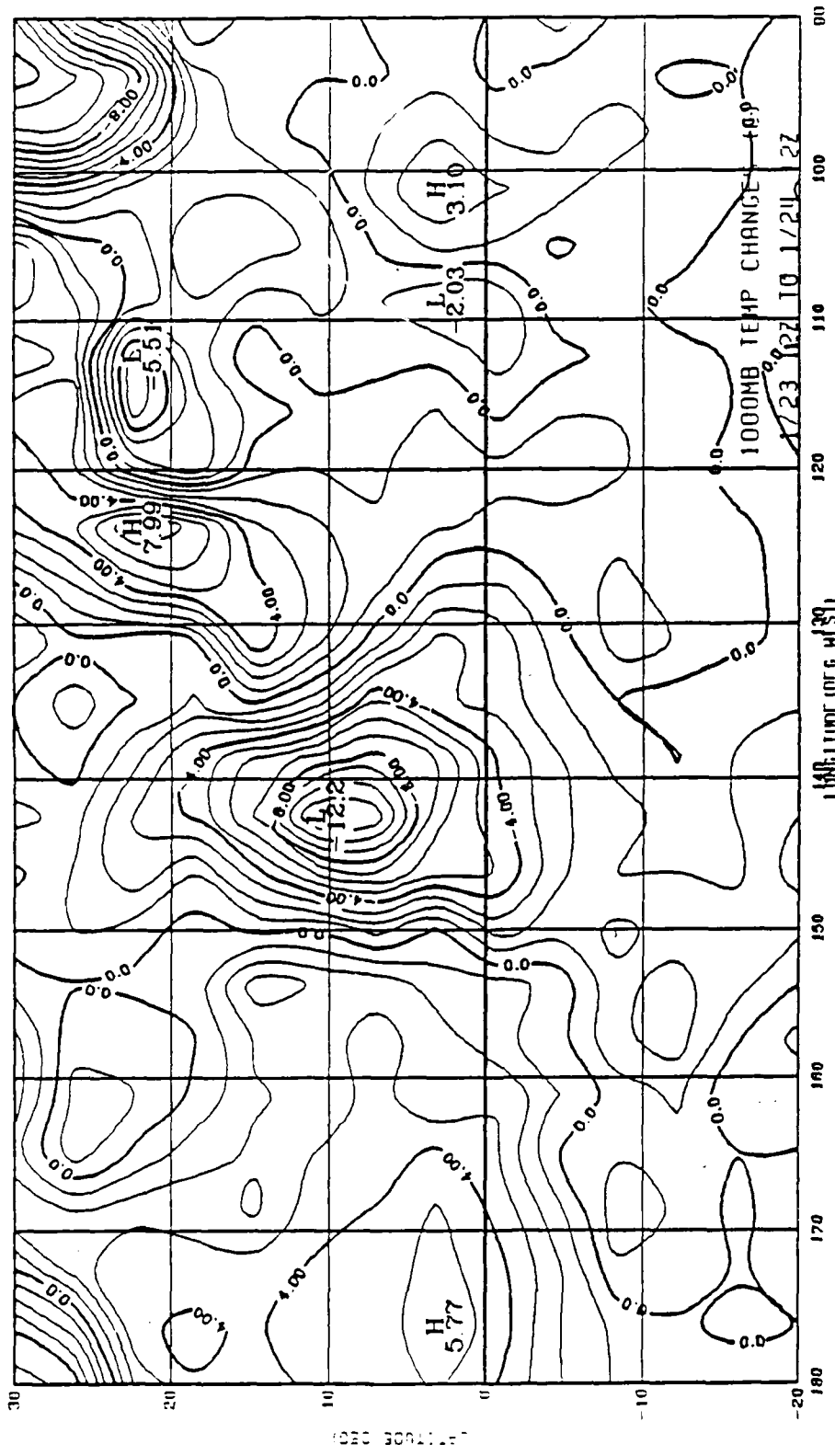


Fig. 51. As in Fig. 47 except for the period ending 1200 GMT 24 January 1979.

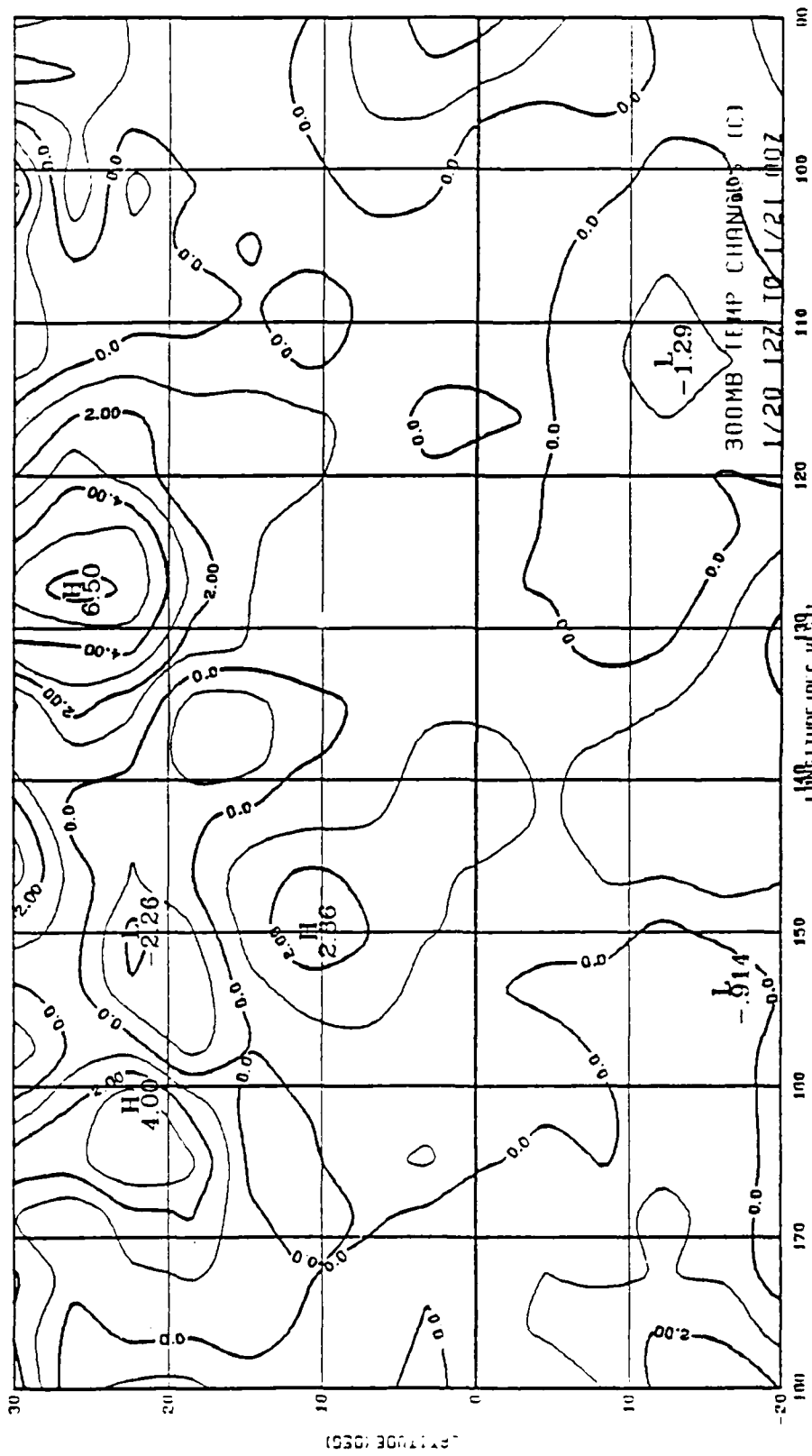


Fig. 52. FGGE IIIB 12 h temperature changes at 300 mb for the period ending 0000 GMT
21 January 1979. Units are °C.

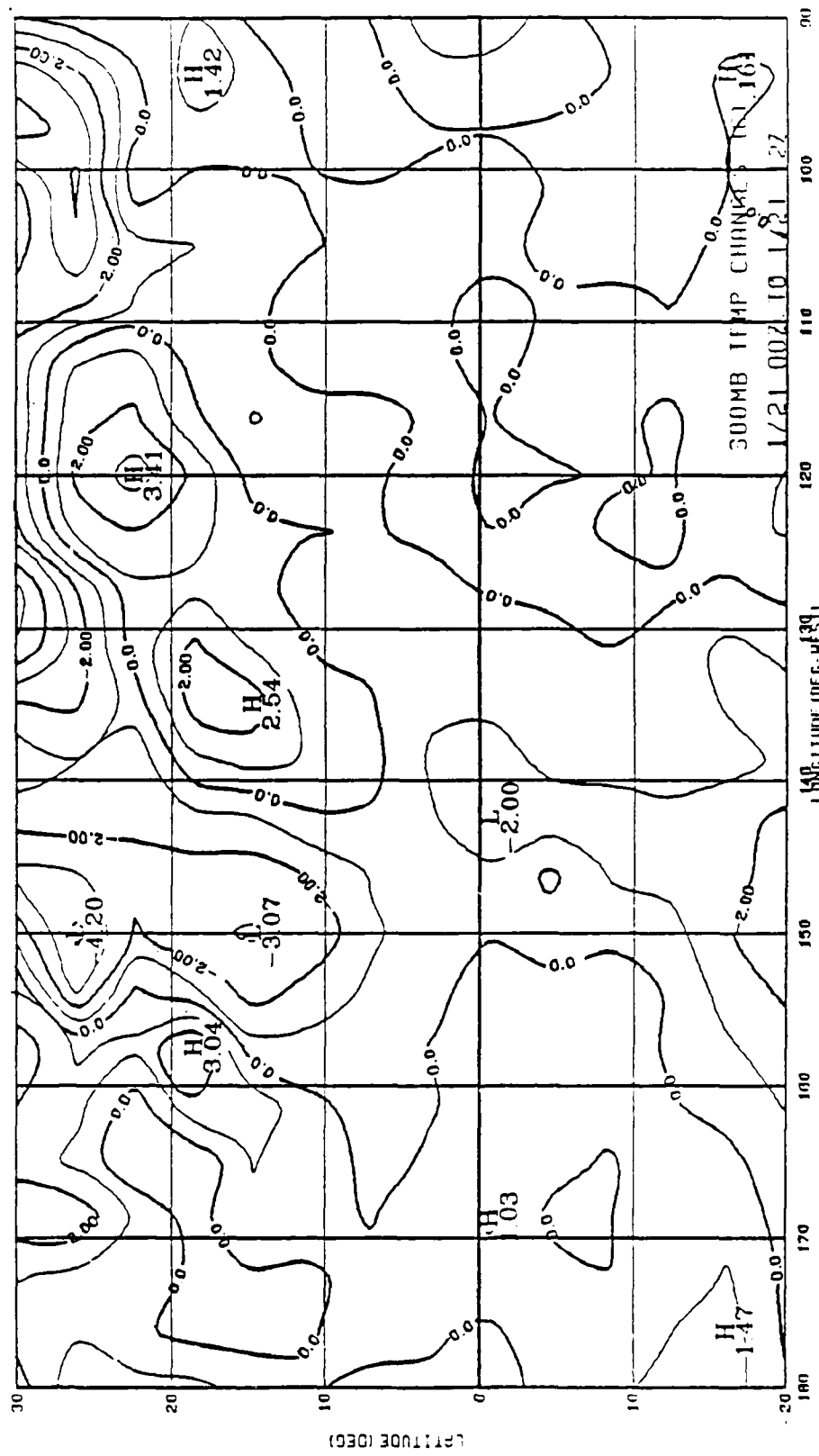


Fig. 53. As in Fig. 52 except for the period ending 1200 GMT 21 January 1979.

location, although there is now a second maximum center south of the original location. The area around $21^{\circ}\text{N}/120^{\circ}\text{W}$ has even greater warming and is in an area of cloudiness resulting from a moisture burst that originated prior to 20 January.

By 0000 GMT on the 22nd (Fig. 54) the area of cooling moved east and is now centered at $19^{\circ}\text{N}/135^{\circ}\text{W}$. The center of the warming to the west remained stationary, but encompasses a much larger area. The line of 0°C temperature change separating these two areas now runs from about $30^{\circ}\text{N}/140^{\circ}\text{W}$ to $5^{\circ}\text{N}/153^{\circ}\text{W}$ which roughly bisects the first burst south of 20°N .

The center of warming moves to $26^{\circ}\text{N}/150^{\circ}\text{W}$ by 1200 GMT on the 22nd (Fig. 55) resulting in a 12 h temperature change greater than 6°C . The cooling region centered at $15^{\circ}\text{N}/147^{\circ}\text{W}$ is now within the moisture burst. This results in a southwest-northeast temperature change gradient which is strong along a line from $12^{\circ}\text{N}/155^{\circ}\text{W}$ to $30^{\circ}\text{N}/140^{\circ}\text{W}$. This gradient lies along the moisture burst axis.

Fig. 56 shows that by 0000 GMT on the 23rd the burst region is dominated by an area of warming. There is one center of almost 5°C at $26^{\circ}\text{N}/139^{\circ}\text{W}$ and another of about 4°C at $17^{\circ}\text{N}/150^{\circ}\text{W}$. There is a region of cooling to the east of this at $26^{\circ}\text{N}/120^{\circ}\text{W}$ and a new area of cooling in the northwest at $22^{\circ}\text{N}/171^{\circ}\text{W}$.

The northwestern cooling is slowly moving south-southeast and is over the Hawaiian Islands by 0000 GMT on the 24th (Fig. 57) with a maximum cooling of 2.6°C . Fig. 58 shows the cooling center that was over Hawaii moved southeast and is at $10^{\circ}\text{N}/150^{\circ}\text{W}$ with a maximum change of 2.7°C .

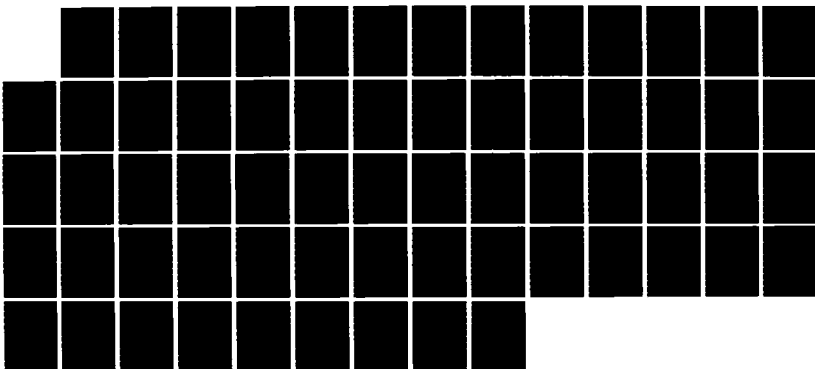
For the period ending 0000 GMT on the 25th (Fig. 59) there is an area of cooling centered at $19^{\circ}\text{N}/131^{\circ}\text{W}$ along the axis of the second moisture burst. By 1200 GMT (Fig. 60) there is warming in the general region of origin of the second burst at $15^{\circ}\text{N}/147^{\circ}\text{W}$ and cooling along the northern edge of the burst axis at $26^{\circ}\text{N}/127^{\circ}\text{W}$.

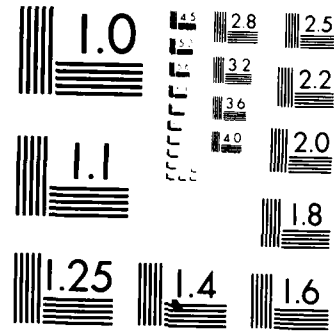
AD-A170 670 OBSERVING THE SYNOPTIC STRUCTURE OF TWO MOISTURE BURSTS 2/2
(U) AIR FORCE INST OF TECH WRIGHT-PATTERSON AFB OH
J R SCHAEFER DEC 85 AFIT/CI/NR-86-70T

UNCLASSIFIED

FFG 4/2

NL





MICROCOPY RESOLUTION TEST CHART
NATIONAL BUREAU OF STANDARDS 1963 A

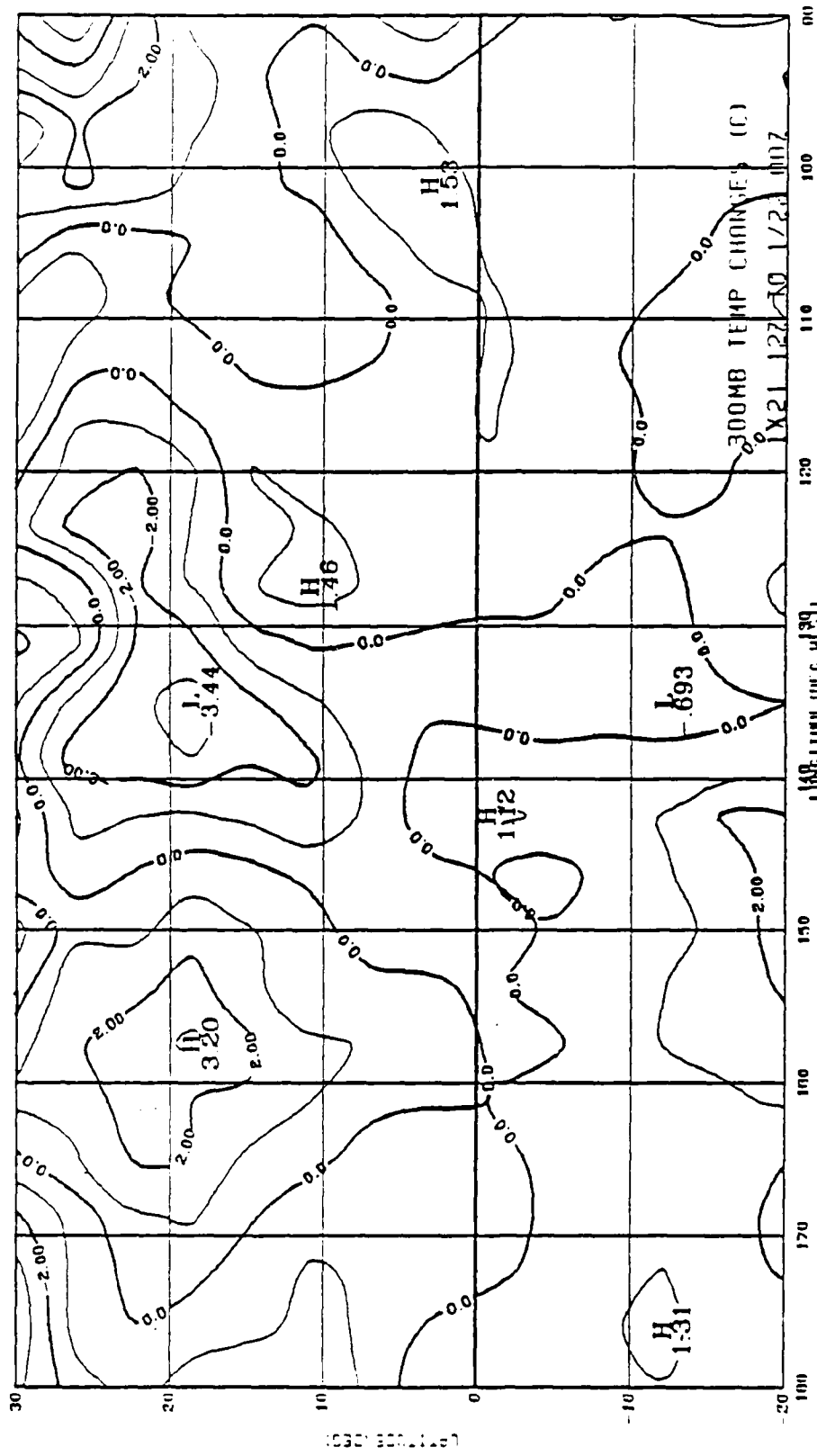


Fig. 54. As in Fig. 52 except for the period ending 0000 GMT 22 January 1979.

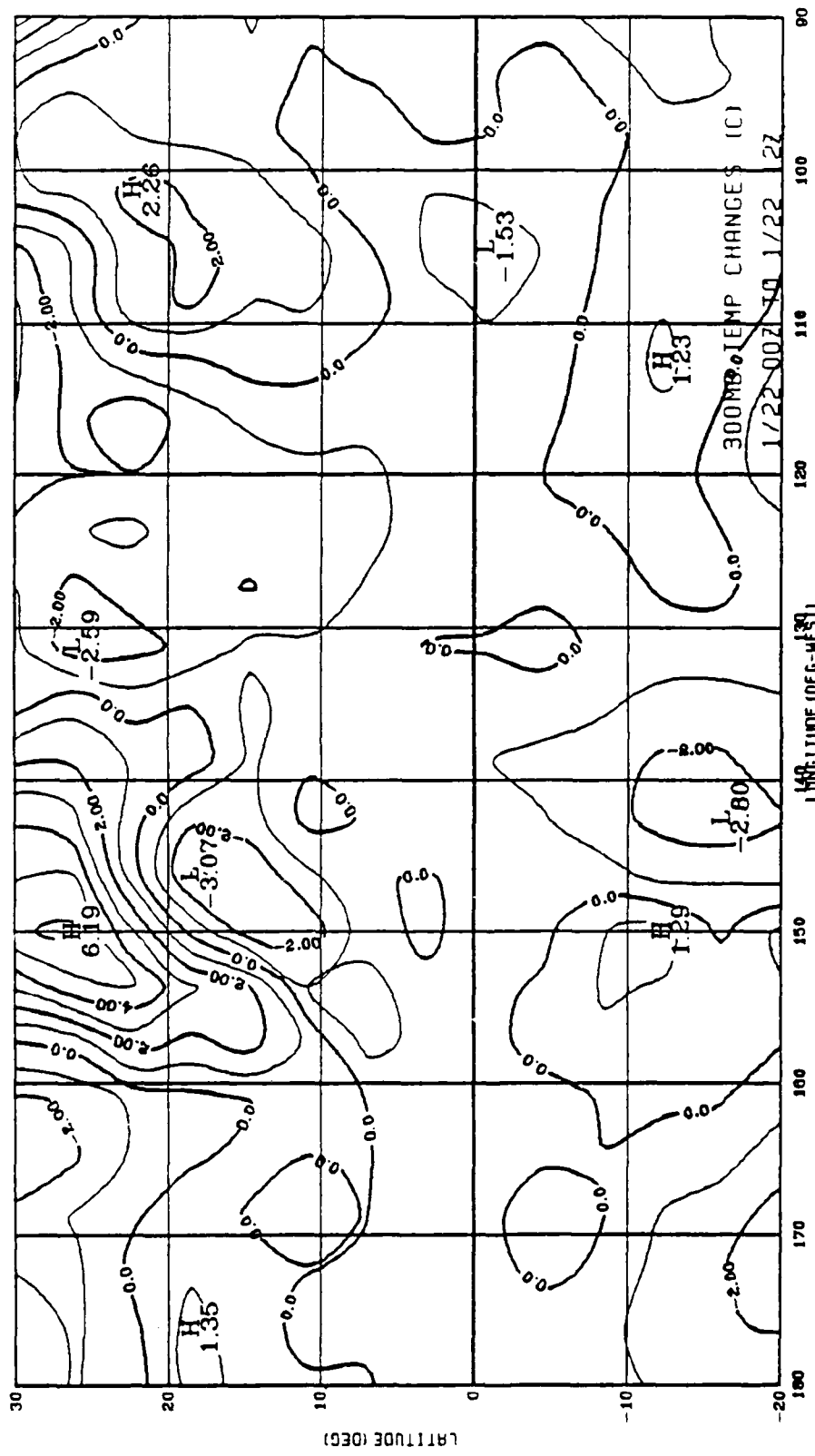


Fig. 55. As in Fig. 52 except for the period ending 1200 GMT 22 January 1979.

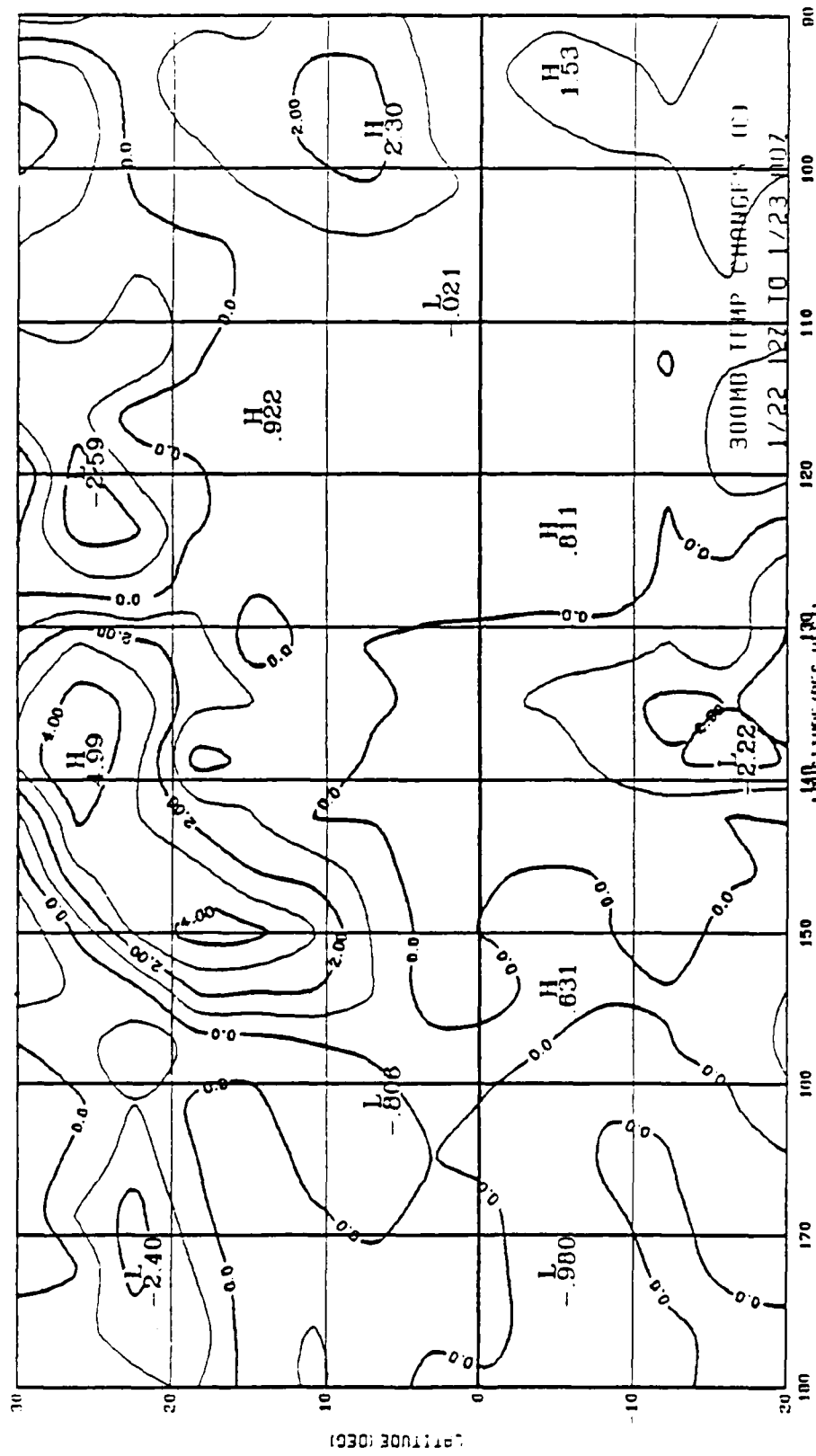


Fig. 56. As in Fig. 52 except for the period ending 0000 GMT 23 January 1979.

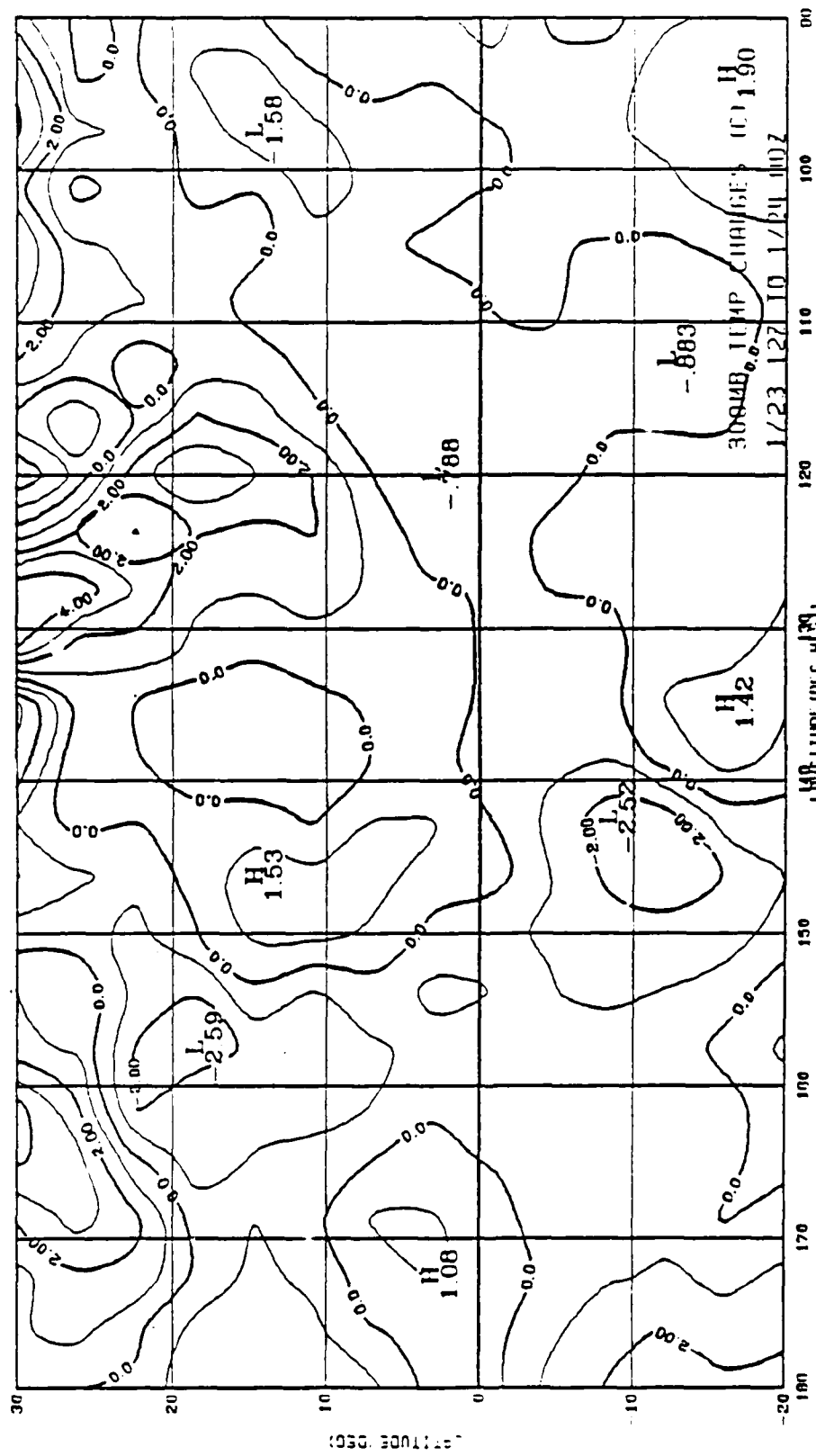


Fig. 57. As in Fig. 52 except for the period ending 0000 GMT 24 January 1979.

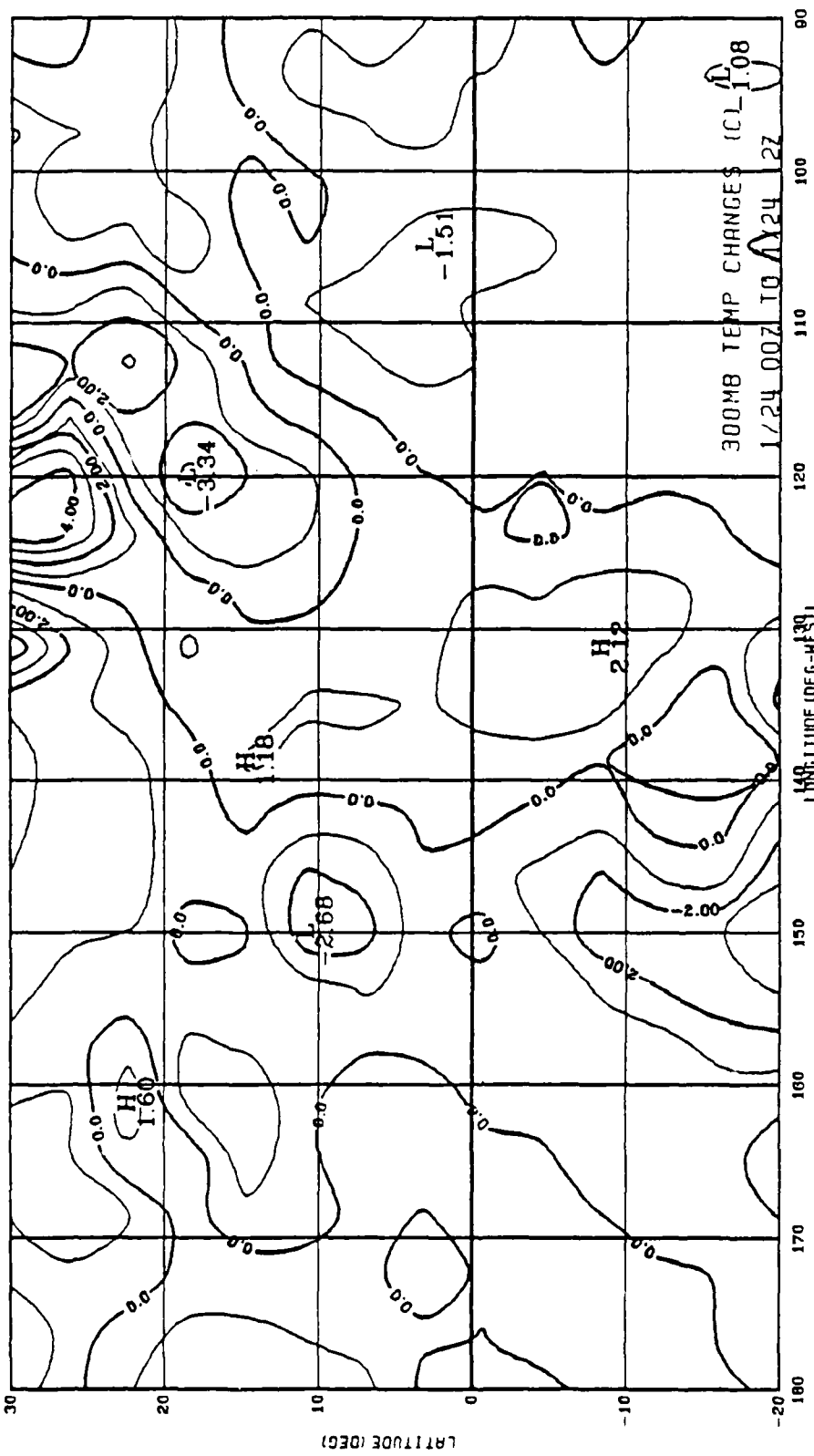


Fig. 58. As in Fig. 52 except for the period ending 1200 GMT 24 January 1979.

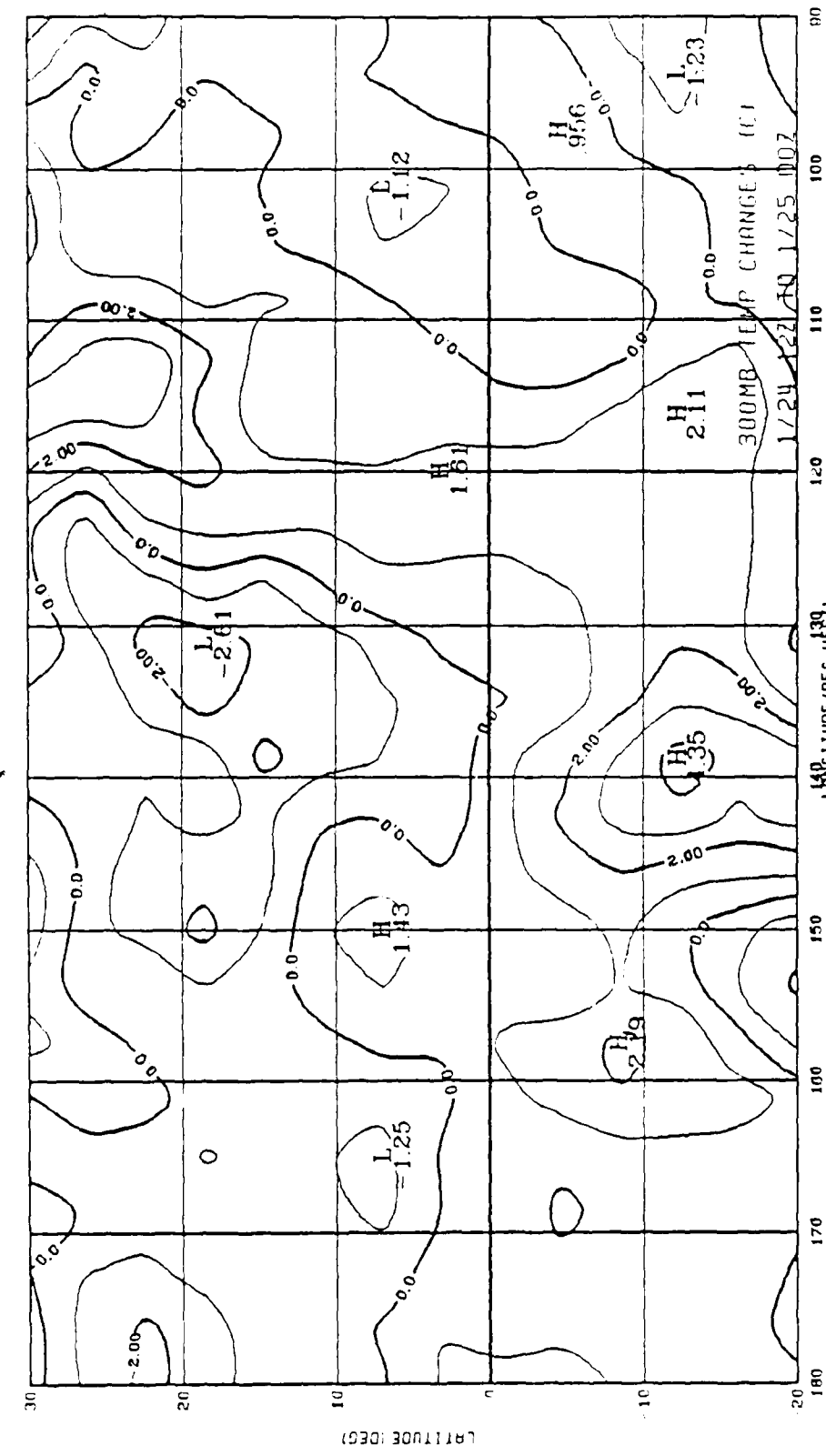


Fig. 59. As in Fig. 52 except for the period ending 0000 GMT 25 January 1979.

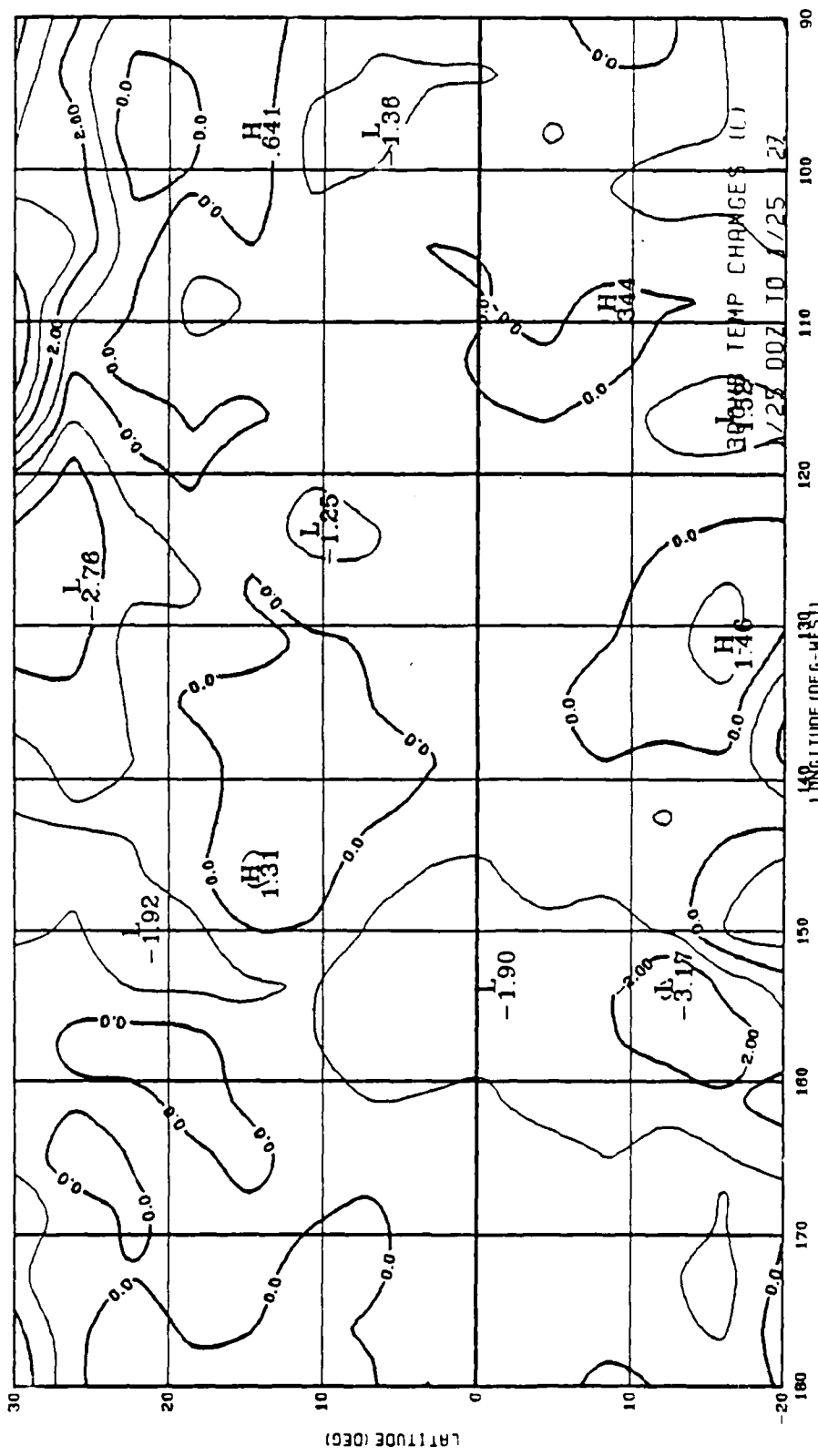


Fig. 60. As in Fig. 52 except for the period ending 1200 GMT 25 January 1979.

The 300 mb temperature changes point to an upper level cooling trend moving in from the northwest during the origin time period for the first burst. The second burst has a much weaker and more confused pattern, but has some cooling to the northwest of the burst. This cooling supports the upper level cold air associated with the trough that will be shown to coincide with the first moisture burst (Section 4e). The significant warming behind the cold air also discussed in Section 4e was also shown for the first burst.

d. FGGE IIIb relative humidity depictions

The next set of Figs. are three-dimensional depictions of the FGGE IIIb RH fields for the two bursts. To create the cross sections, a line was drawn through the approximate center of the moisture burst, based on cloud imagery, for each time period. They are not exact center lines because time continuity of tracks was also considered important. Therefore if a track was still considered representative of the burst 12 h later it was retained, even if it was not precisely centered. The (a) portions of these figures are the vertical cross sections along burst axes. The heights are a quasi-logarithmic (modified slightly to allow better representation of the figures) pressure scale in millibars. Additional tracks were chosen to lie perpendicular to the main track. The locations were selected to allow depiction of selected features along the moisture bursts. The point of intersection of each perpendicular section with the main track is labeled along the bottom of the main cross sections. These perpendicular tracks, and the main track, are shown on the map insert in the upper right of the main track figures. On each map are stippled areas representing the locations of significant clouds at the time of the cross section. Since the maps show all significant clouds, the edges of the stippled areas do not

necessarily represent the boundaries of the unbroken middle and upper clouds that fulfill the actual moisture burst definition. All the tracks are computer analyzed with RH areas greater than 80% lined, and areas greater than 70% stippled. The areas with FGGE IIIb RH greater than 70% do not encompass the entire cloudy regions, but regions having 60% and greater RH showed just as much area that was relatively cloud free. Therefore a value of 70% and greater was selected as representing areas in the FGGE IIIb analyses coinciding with cloudiness.

Figs. 61a and 61b are for 0000 GMT on the 21st. The main track does not follow the cloud pattern for this time period, but lies along the approximate axis of the initial cloudiness of the first moisture burst. Selection of the track is done to study the RH depiction before the actual moisture burst. The moist region marked A in the southwest portion of the main track is related to the ITCZ as shown in the cloud mapping. Perpendiculars 2 and 3, and the large area of moisture marked B on the main cross section capture the three cloudy areas present. They represent the narrow cloud band to the south (although cloud height is not well represented) and the two relatively small areas of low clouds along, and north of the main track. Even though the first burst has not yet met the definition, there are still areas of moisture remaining along the approximate axis from the previous burst.

The moisture associated with the ITCZ is represented by the area marked A on Figs. 62a-b. The figures show the ITCZ moisture to be mostly in the southern section of the tracks, extending from the surface up to above 400 mb in Fig. 62a, perpendicular 1 and 2, and somewhat lower in perpendicular 3. The moisture is largely confined to the southeast of the main track as evidenced by track 2. There is an area of low-level moisture further along the main track at point B. As suggested by the satellite imagery, there seems to be more than one low level moisture source in this moisture burst.

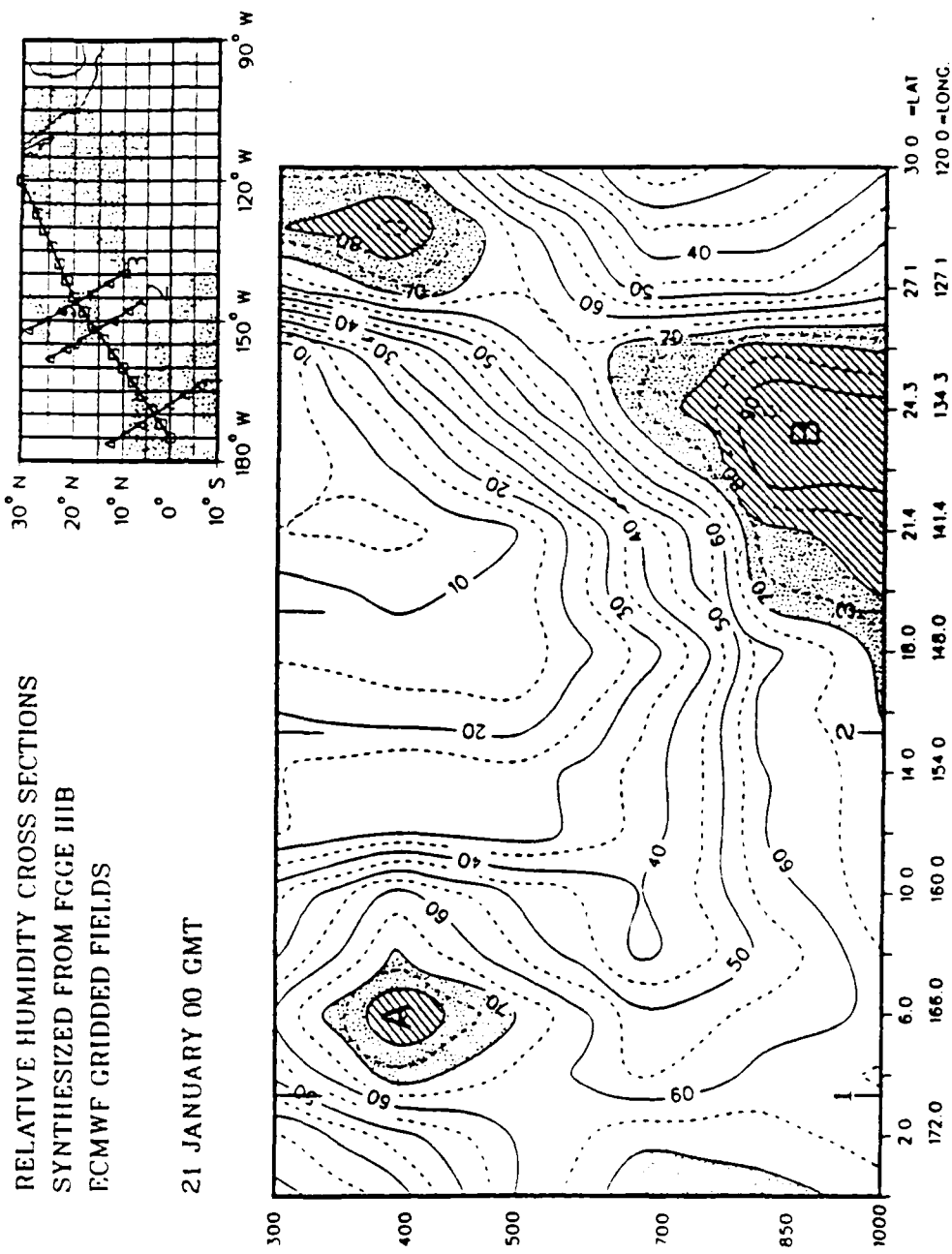


Fig. 61a. Vertical cross section of FGGE IIIb relative humidity for 0000 GMT 21 January 1979. Units are % R.H. Regions greater than 70% are stipled and greater than 80% are lined. Shaded areas in the cross section track (upper right) represent significant clouds.

PERPENDICULAR SECTION 1
CROSSING TRACK AT 170W
PERPENDICULAR SECTION 2
CROSSING TRACK AT 152W
PERPENDICULAR SECTION 3
CROSSING TRACK AT 146W

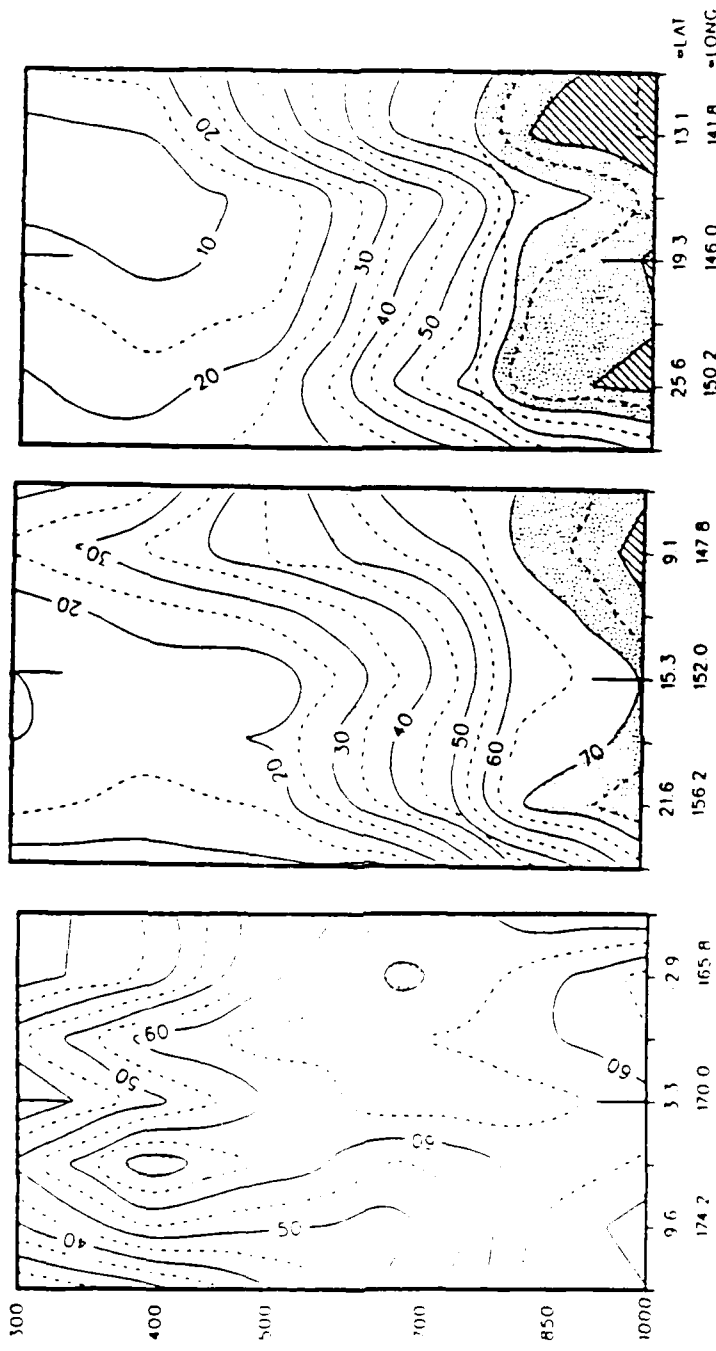


Fig. 61b. Vertical cross sections of FGGE IIIB relative humidity perpendicular to the main track for 0000 GMT 21 January 1979. Units are % R.H. shaded as in Fig. 61a.

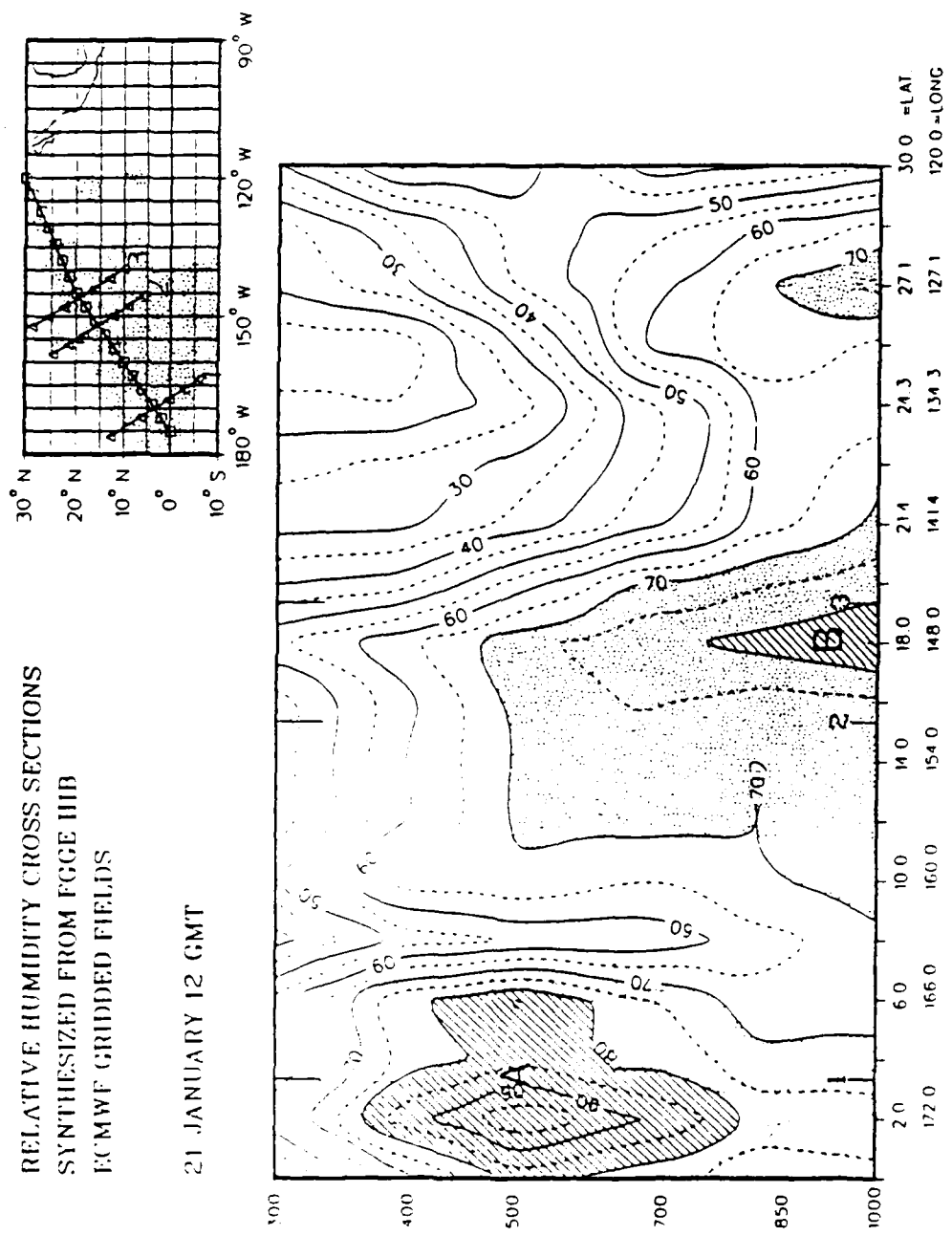


Fig. 62a. As in Fig. 61a except for 1200 GMT 21 January 1979.

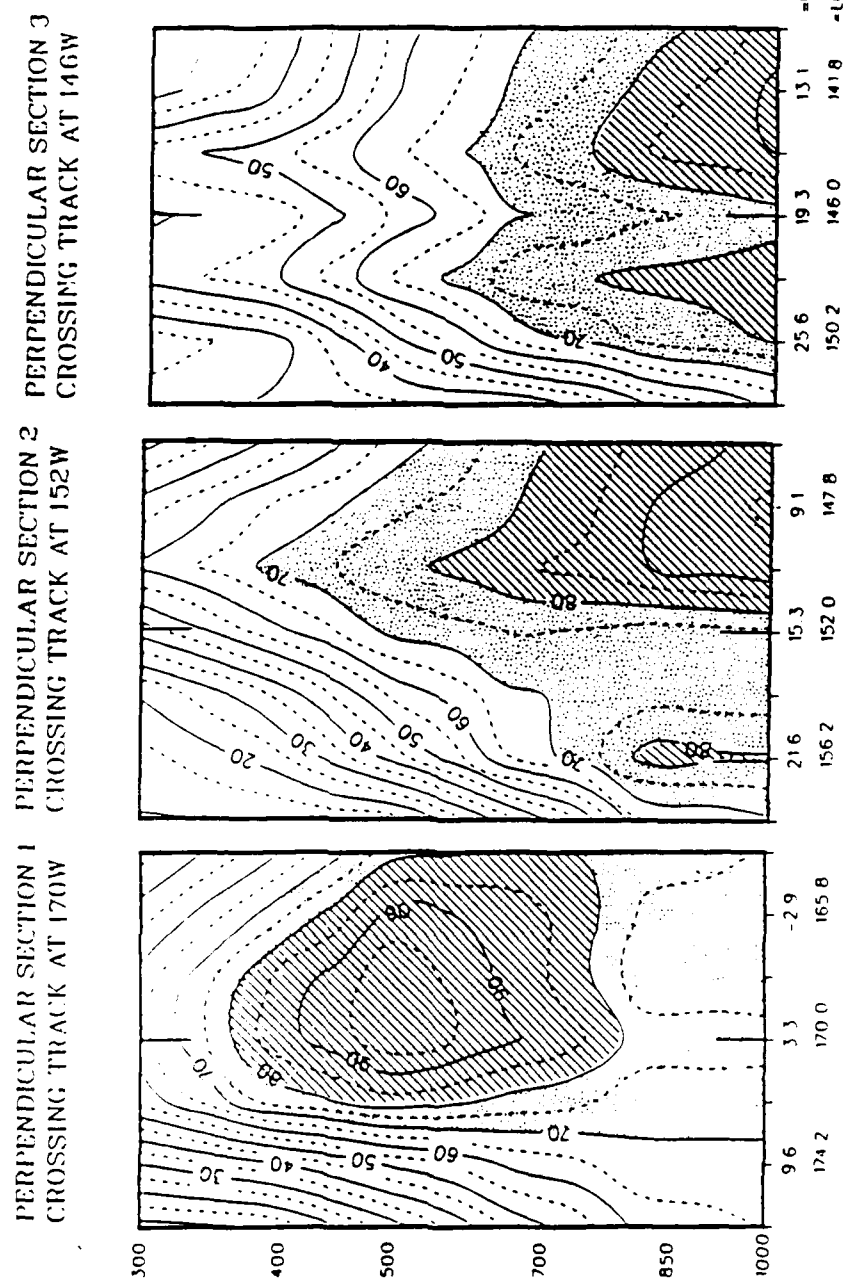


Fig. 62b. As in Fig. 61b except for 0000 GMT 22 January 1979.

These same tracks are used for 0000 GMT on the 22nd (Figs. 63a and 63b). The western moisture region, marked A, has expanded northeastward. The second region, marked C, has greatly expanded and advected downwind, and is now deep moisture from the surface to 300 mb. There is a dry region between A and C. This region's dryness intensified between 0000 and 1200 GMT while the burst was first developing. Perpendicular 2 shows that while there is a drier area on the main track, there is moisture just to the south, again in the ITCZ.

The track is shifted to the east for 1200 GMT on the 22nd (Figs. 64a and 64b). The ITCZ continues to be represented by the area marked A, and there still seems to be a drier region between it and the moisture area marked C. The northern ends of the perpendiculars show that this dry region lies all along the northern flank of the burst, with its southernmost extent to about 8° N, just northeast of the burst origin. All perpendiculars again show some moisture to the southeast of the main track.

The sections for the 23rd at 0000 GMT (Figs. 65a and 65b) retain the same tracks. A large area of continuous moisture is shown over almost the entire track. This sudden increase in moist areas seems to be due not only to advection from the ITCZ, but also increased vertical transport of moisture. Comparing the cloudy areas in Fig. 64a with Fig. 65a shows the amount of cloudiness remains fairly steady, while the area of FGGE IIIb moisture is actually increasing. This could be due to the FGGE IIIb model increasing the vertical transport of moisture. This agrees with the actual increase in convection as shown through satellite interpretation in Section 4a.

The same tracks are used at 1200 GMT on the 23rd (Figs. 66a and 66b). The main track shows two separate regions of moisture. Region A is a continuation of the moisture as shown previously in the figures. The dry area at perpendicular 4 is

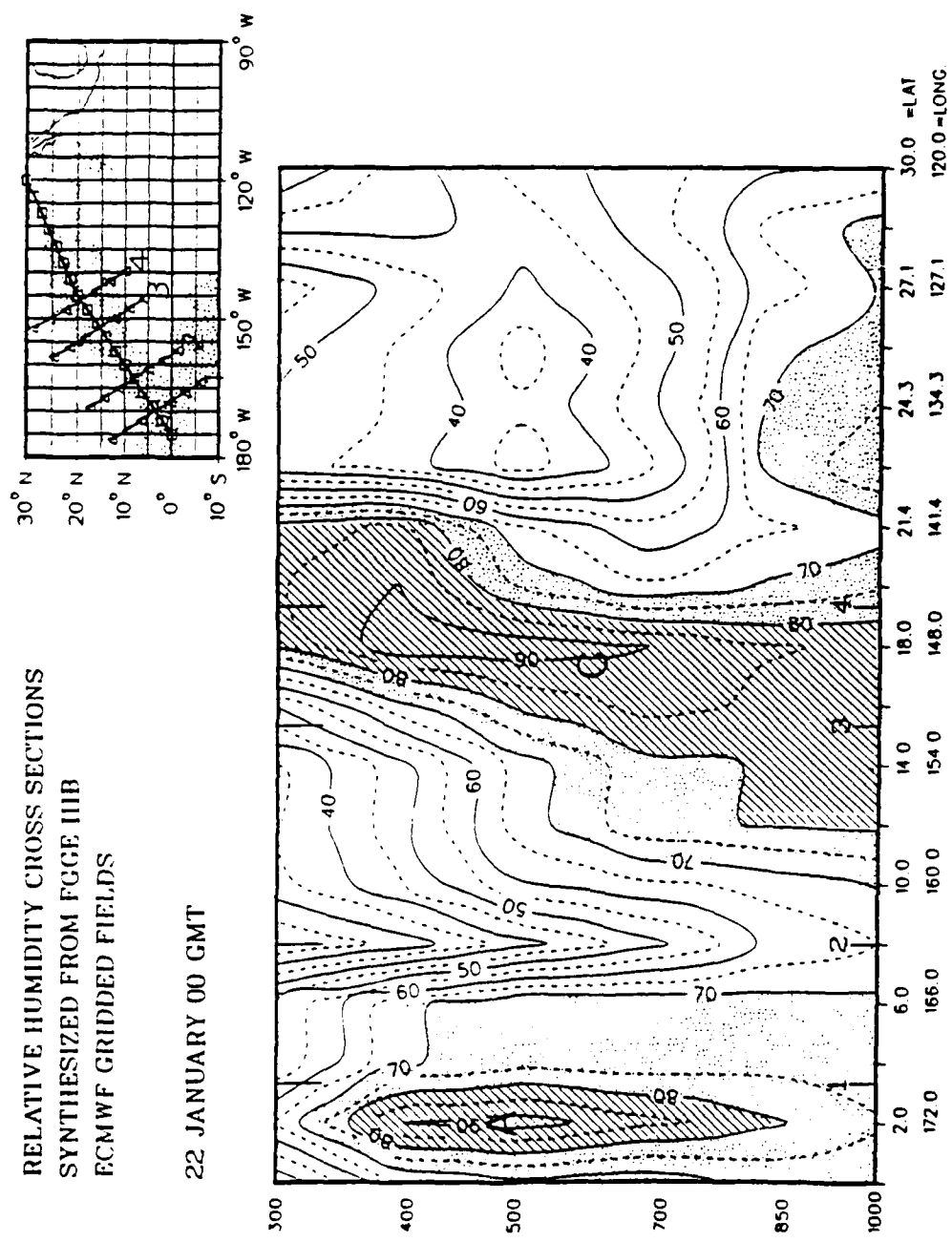


Fig. 63a. As in Fig. 61a except for 0000 GMT 22 January 1979.

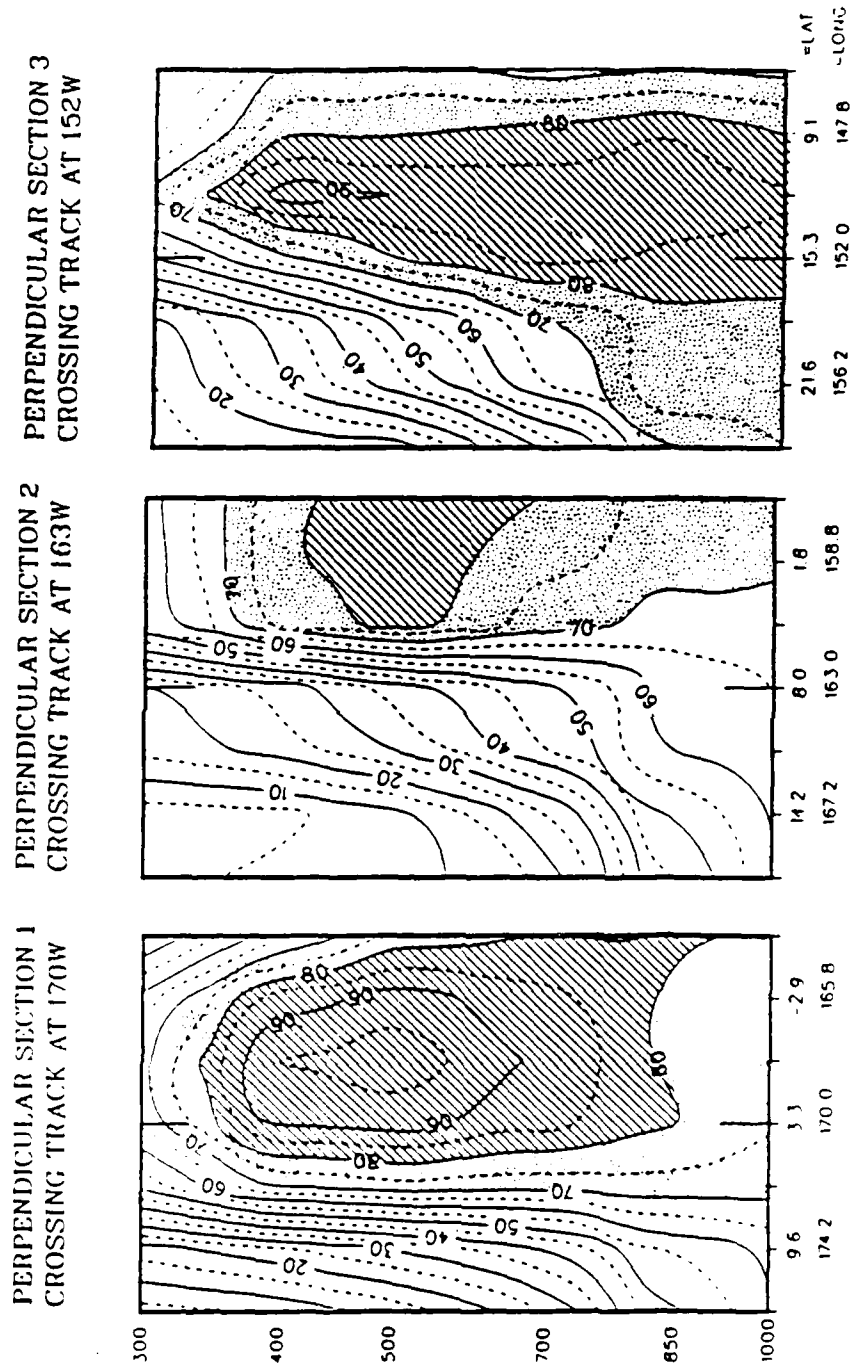


Fig. 63b. As in Fig. 61b except for 1200 GMT 21 January 1979.

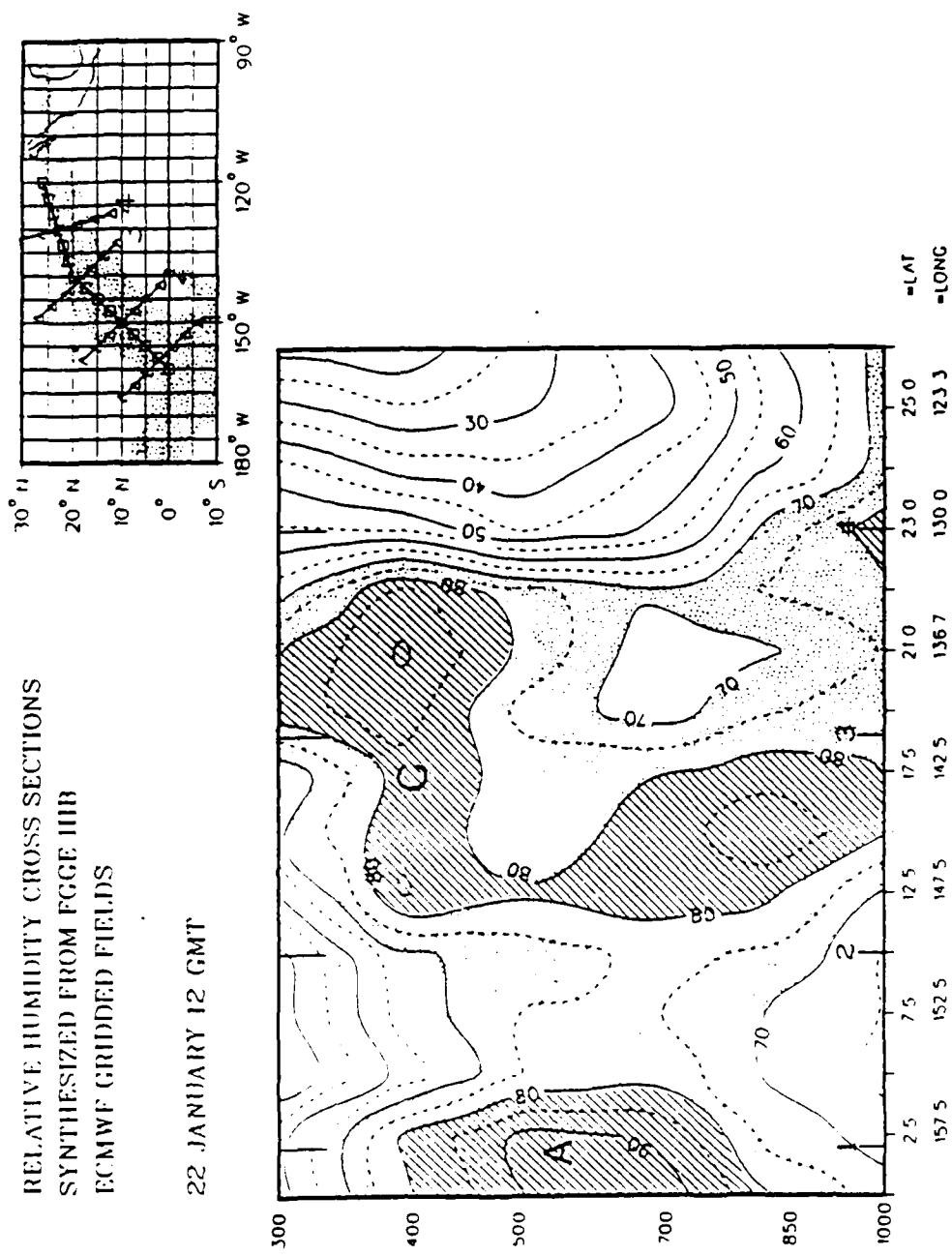


Fig. 64a. As in Fig. 61a except for 1200 GMT 22 January 1979.

PERPENDICULAR SECTION 1
CROSSING TRACK AT 15RW
PERPENDICULAR SECTION 2
CROSSING TRACK AT 150W

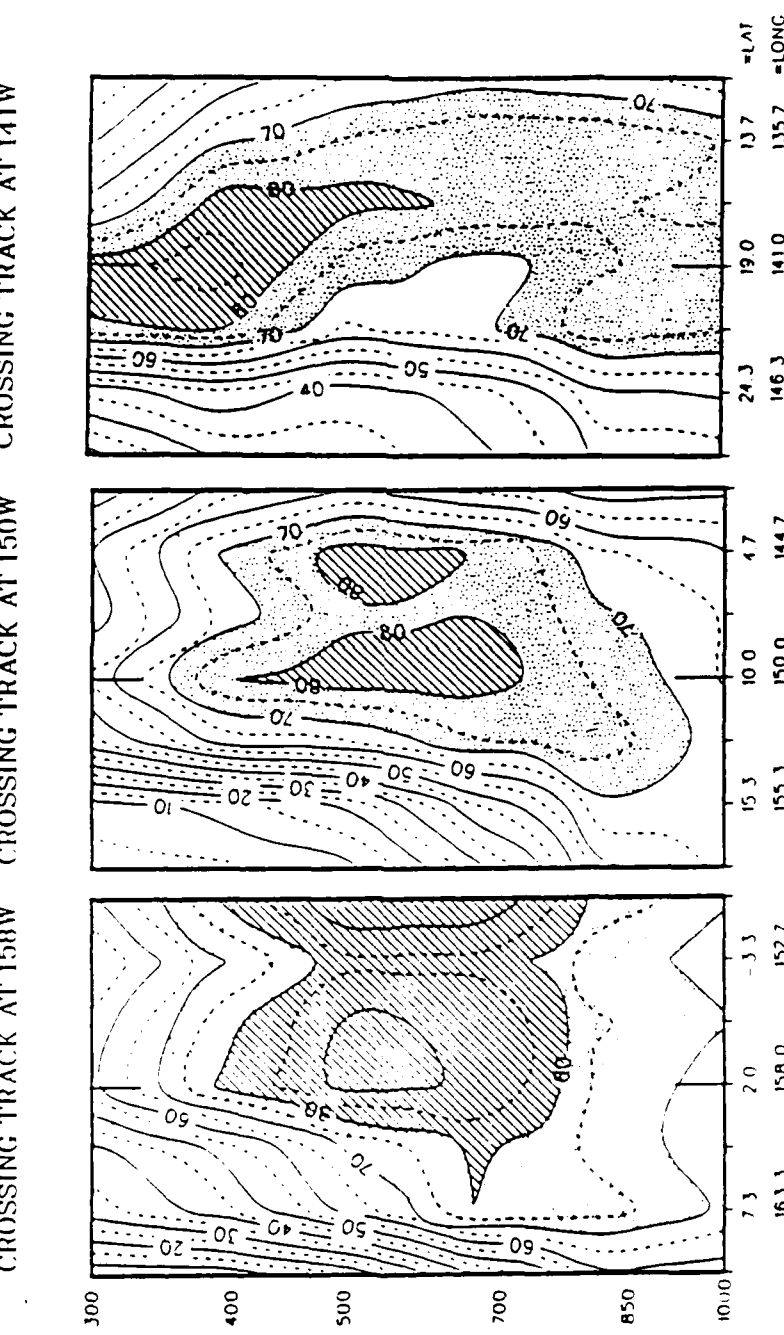


Fig. 64b. As in Fig. 61b except for 1200 GMT 22 January 1979.

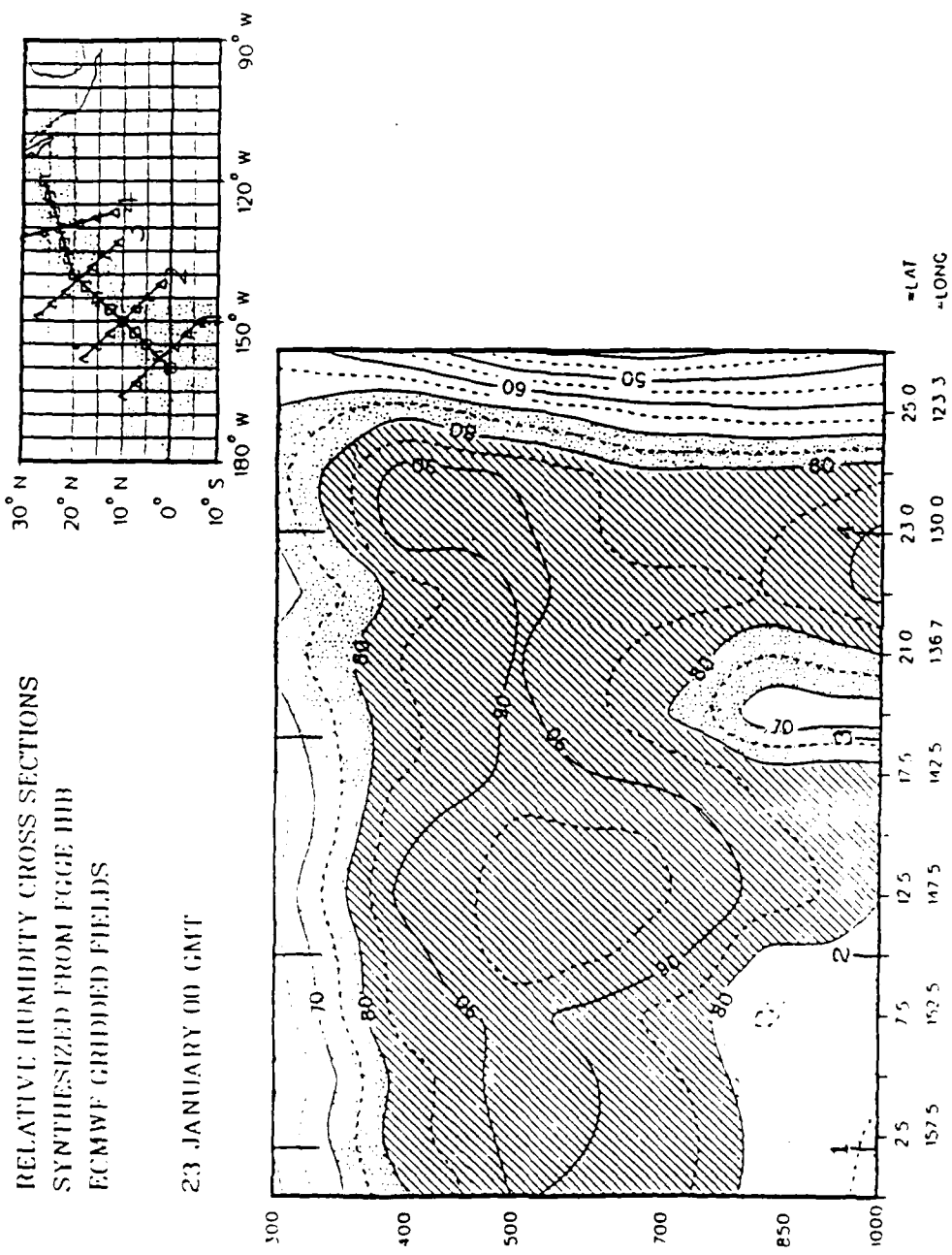


Fig. 65a. As in Fig. 61a except for 0000 GMT 23 January 1979.

PERPENDICULAR SECTION 1
CROSSING TRACK AT 150W

PERPENDICULAR SECTION 2
CROSSING TRACK AT 150W

PERPENDICULAR SECTION 4
CROSSING TRACK AT 130W

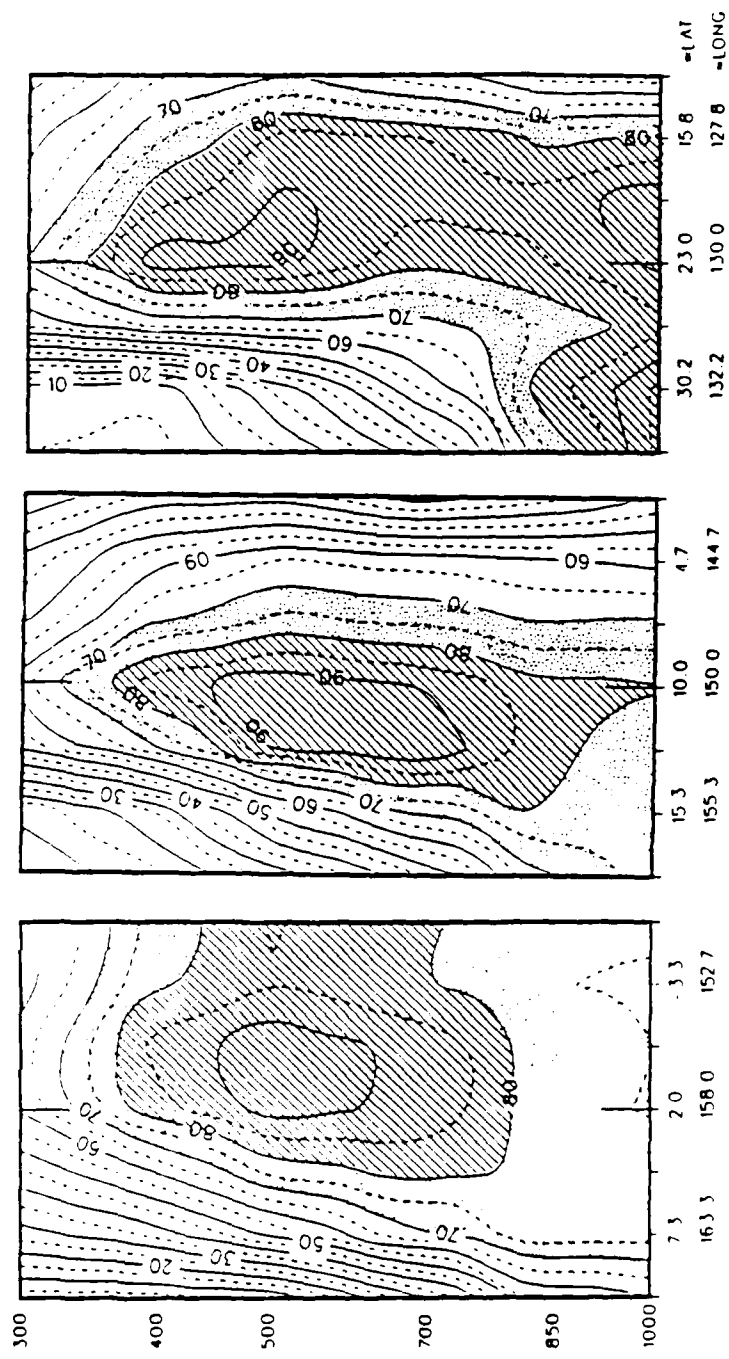


Fig. 65b. As in Fig. 61b except for 0000 GMT 23 January 1979. Note that only perpendiculars 1, 2 and 4 are shown.

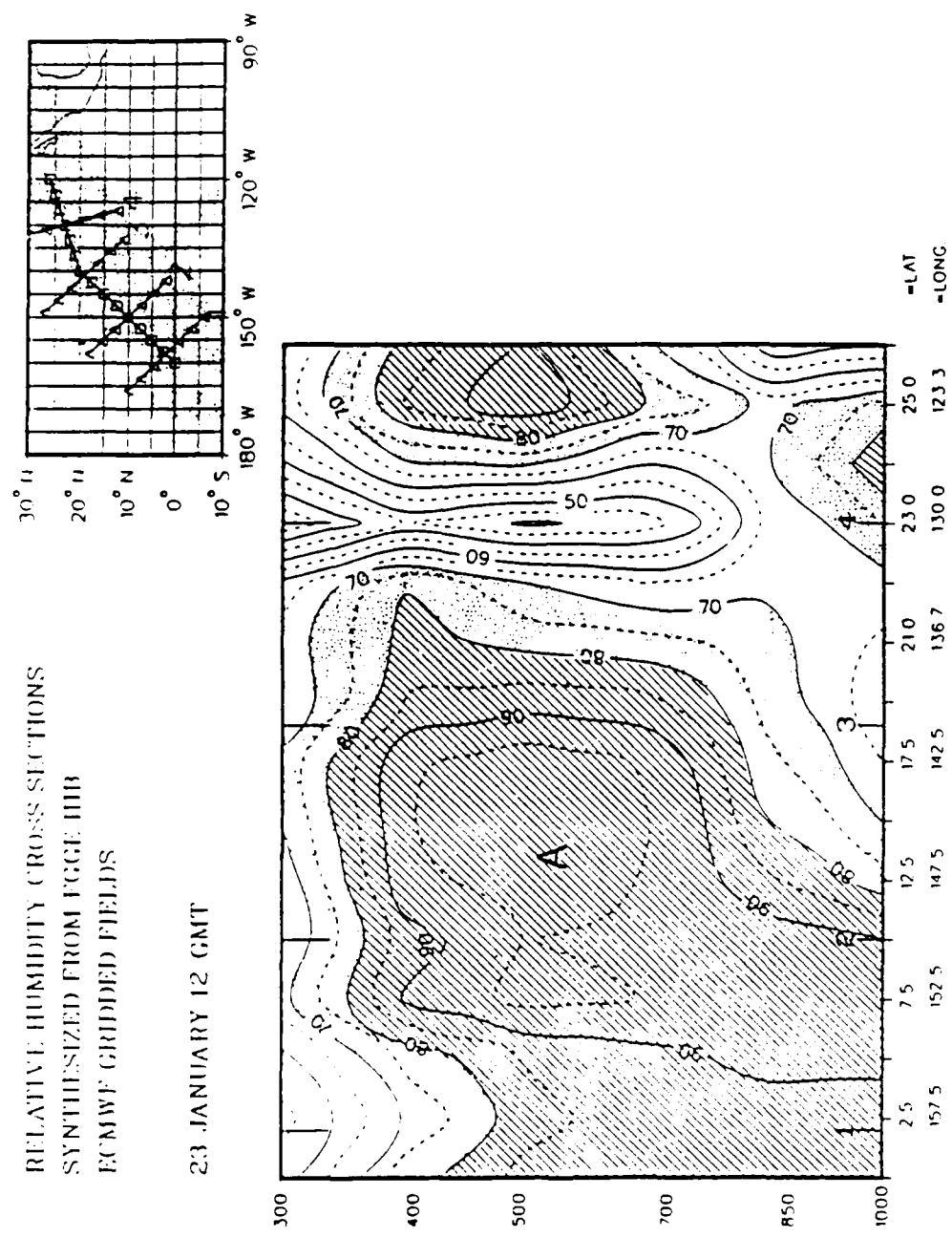


Fig. 66a. As in Fig. 61a except for 1200 GMT 23 January 1979.

PERPENDICULAR SECTION 1
PERPENDICULAR SECTION 2
CROSSING TRACK AT 130W

PERPENDICULAR SECTION 1
CROSSING TRACK AT 150W

PERPENDICULAR SECTION 4
CROSSING TRACK AT 150W

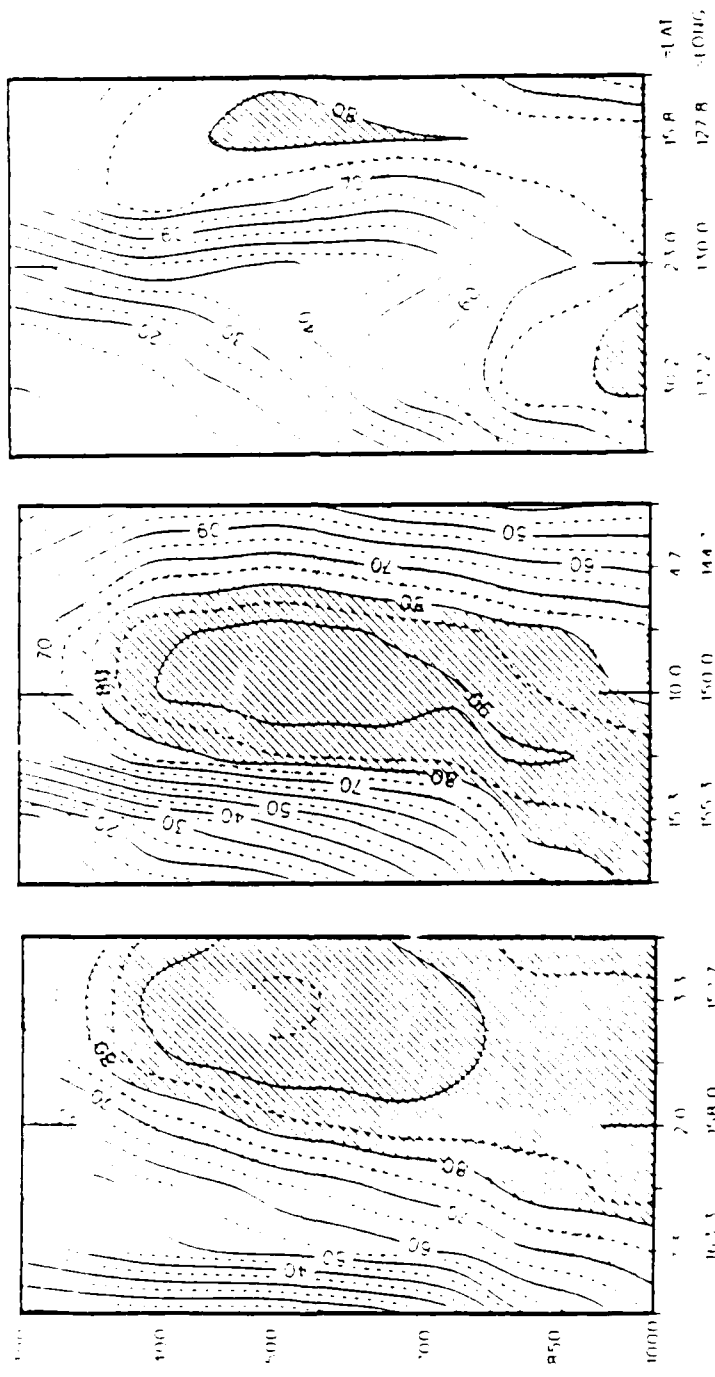


Fig. 66b. As in Fig. 61b except for 1700 GMT 23 January 1979 Note that only
perpendiculars 1, 2 and 4 are shown.

due probably to intrusion from the north of the drier air as well as subsidence. While further along the main track the moisture again becomes apparent.

The track changes again for 1200 GMT on the 24th (Figs. 67a and 67b). The southwestern end and perpendicular 1 both show a drying trend in this area. The general drying prevails throughout the major portions of the tracks. The central moist area marked A is considerably smaller than the same moist area 12 h before. There is a cloudy region from $17^{\circ}\text{N}/157^{\circ}\text{W}$ to $25^{\circ}\text{N}/140^{\circ}\text{W}$ that perpendicular 3 intersects. The perpendicular does not show this to be a high moisture area. Therefore either the FGGE IIIb model does not create the dynamics necessary to create the high RH, or the moisture is not advected into the correct location.

Considerable drying occurs by 0000 GMT on the 25th (Figs. 68a and 68b). There is a new moist area represented by a region of above 80% RH at the equator around 500 mb. This is also represented in one small area on the cross section for perpendicular 1. There is another small area of moisture on perpendicular 4, to the south of the main track. Even though there are few areas of RH above 70% there are significant regions of RH above 60% throughout the moisture burst region.

The same tracks are used for 0000 GMT on the 26th (Figs. 69a and 69b). The southwestern portion of the track is even drier than 12 h earlier, but around perpendicular 2 on the main track an area of moisture has formed.

Figs. 70a and 70b show a moist region that begins with a small area on the southwest edge of the main track. The moisture then increases on the main track between perpendiculars 1 and 2, and once again on perpendicular 2 along the track and just to the north. There is a similar moisture pattern evident at 0000 GMT on the 27th (Figs. 71a and 71b). The significant difference is the lowering of the moisture to 700 mb and below at the later time.

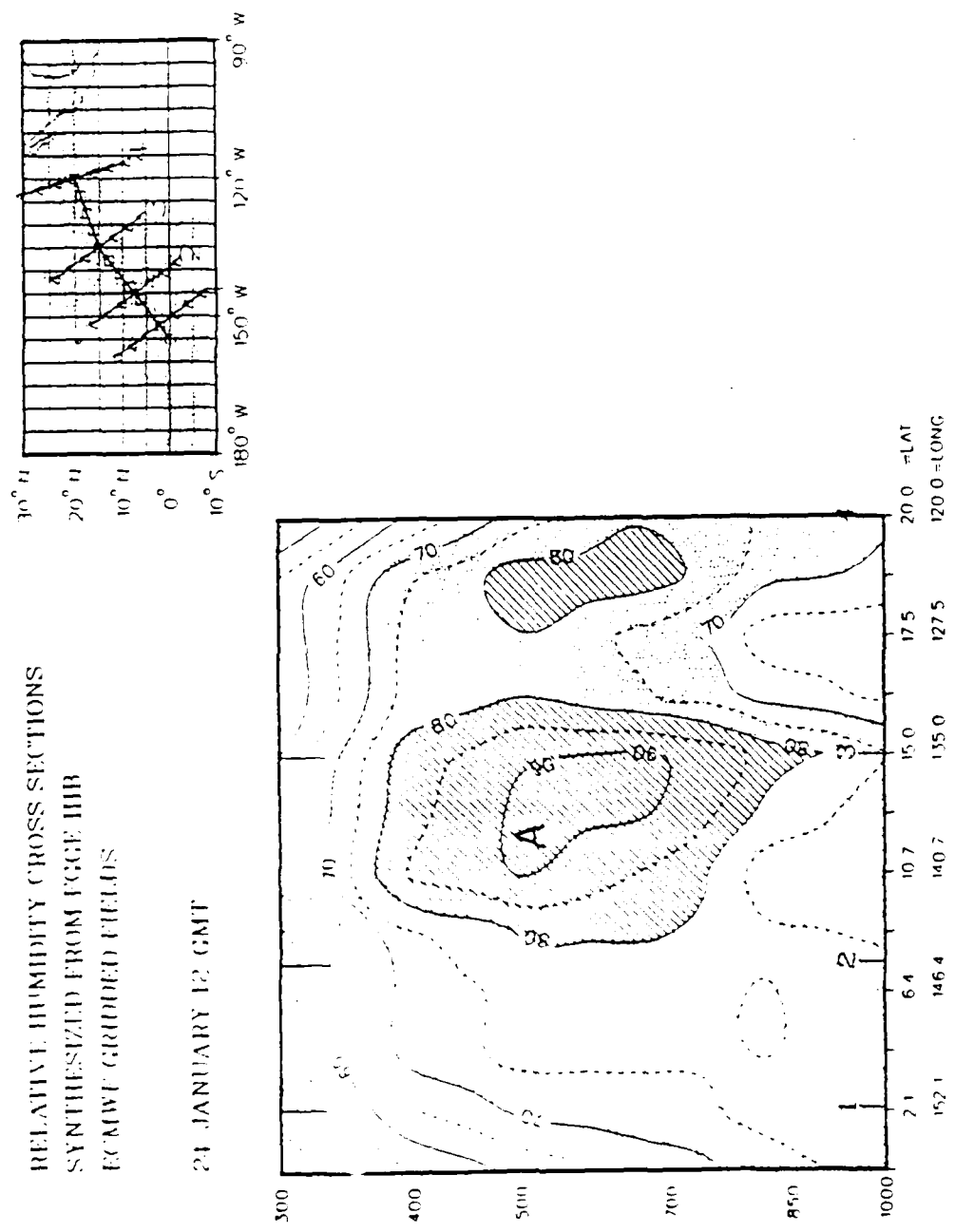
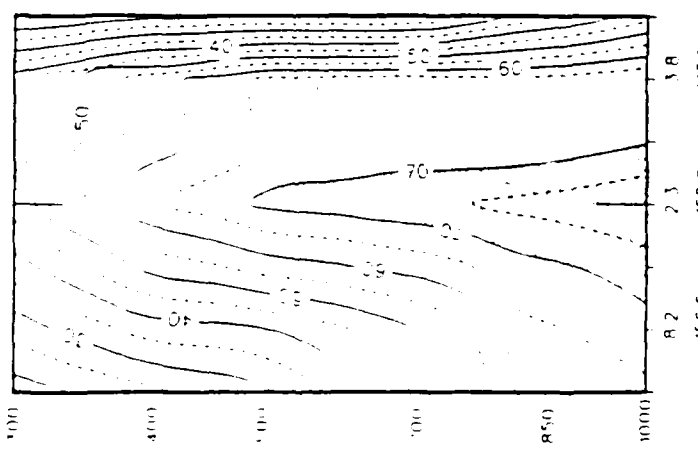
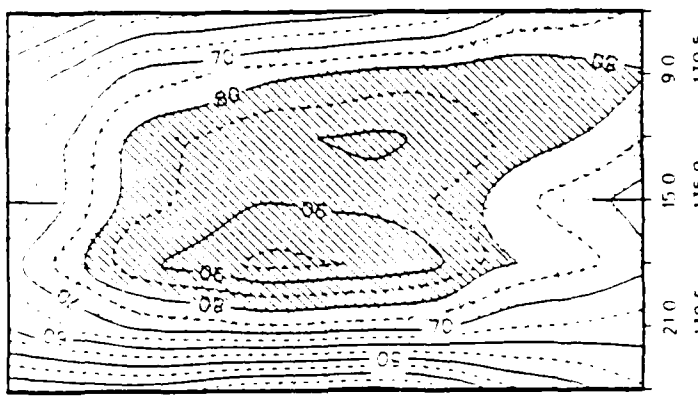


Fig. 67a. As in Fig. 61a except for 1200 GMT 24 January 1979.

PERPENDICULAR SECTION 1
CROSSING TRACK AT 153W



PERPENDICULAR SECTION 3
CROSSING TRACK AT 135W



PERPENDICULAR AIR SECTION 4
CROSSING TRACK AT 115W

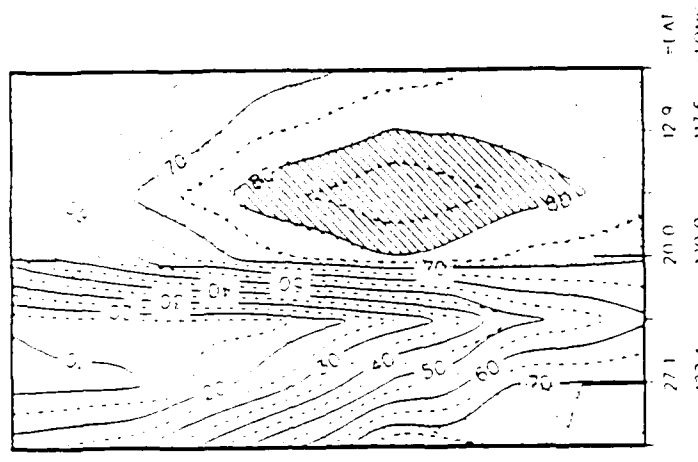


Fig. 67b. As in Fig. 61b except for 1200 GMT 24 January 1979. Note that only perpendiculars 1, 3 and 4 are shown.

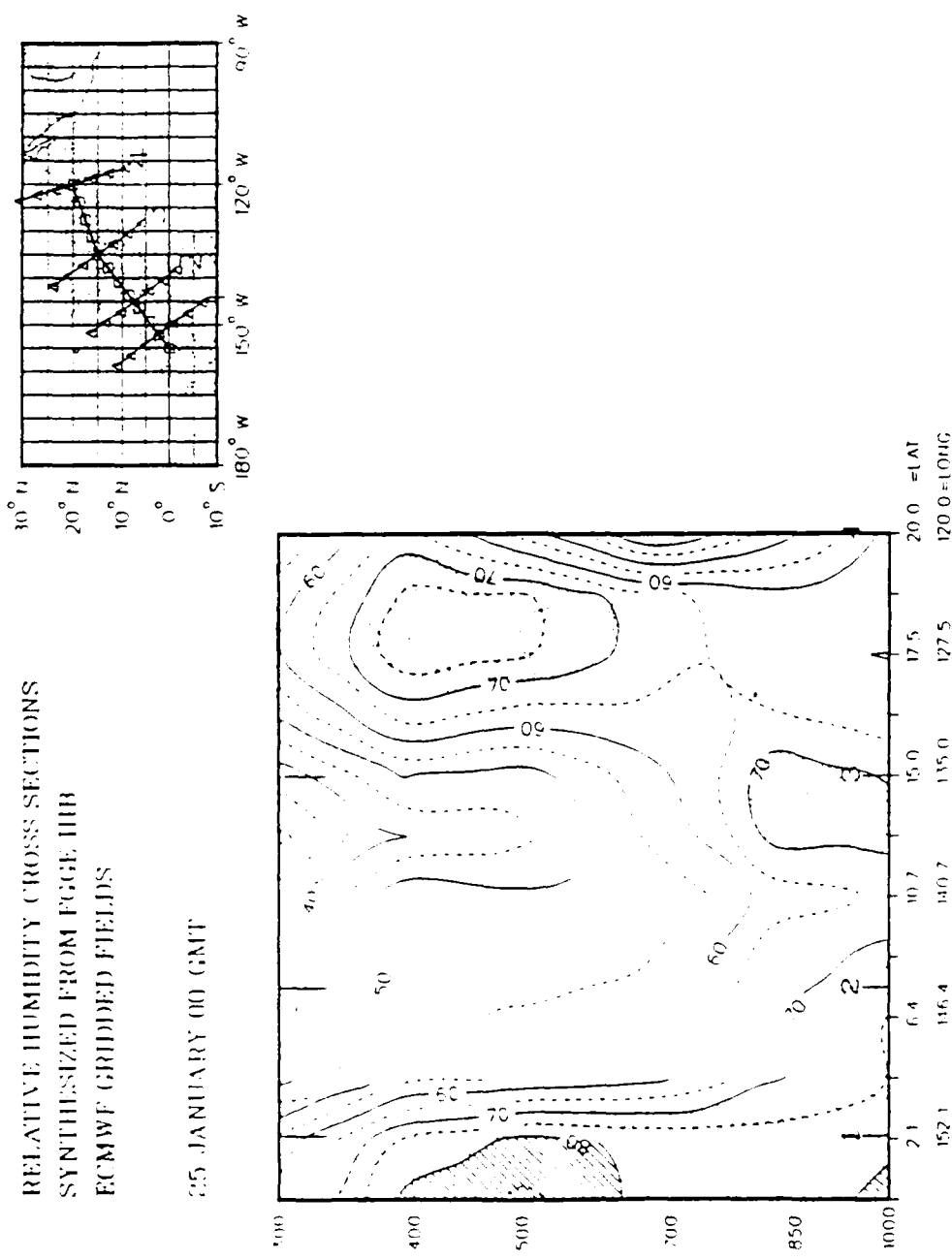


Fig. 68a. As in Fig. 61a except for 0000 GMT 25 January 1979.

PERPENDICULAR SECTION 1
CROSSING TRACK AT 152W

PERPENDICULAR SECTION 3
CROSSING TRACK AT 135W

PERPENDICULAR SECTION 4
CROSSING TRACK AT 120W

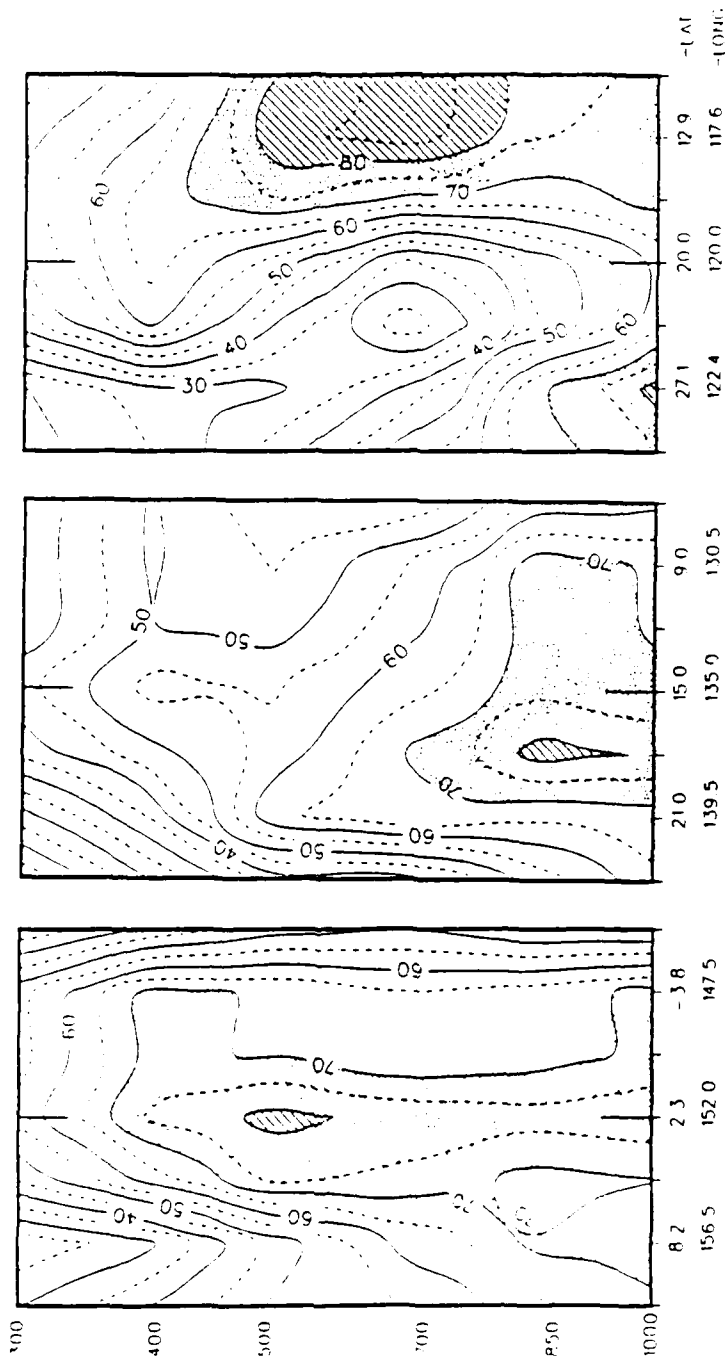


Fig. 68b. As in Fig. 61b except for 0000 GMT 25 January 1979. Note that only perpendicularly 1, 3 and 4 are shown.

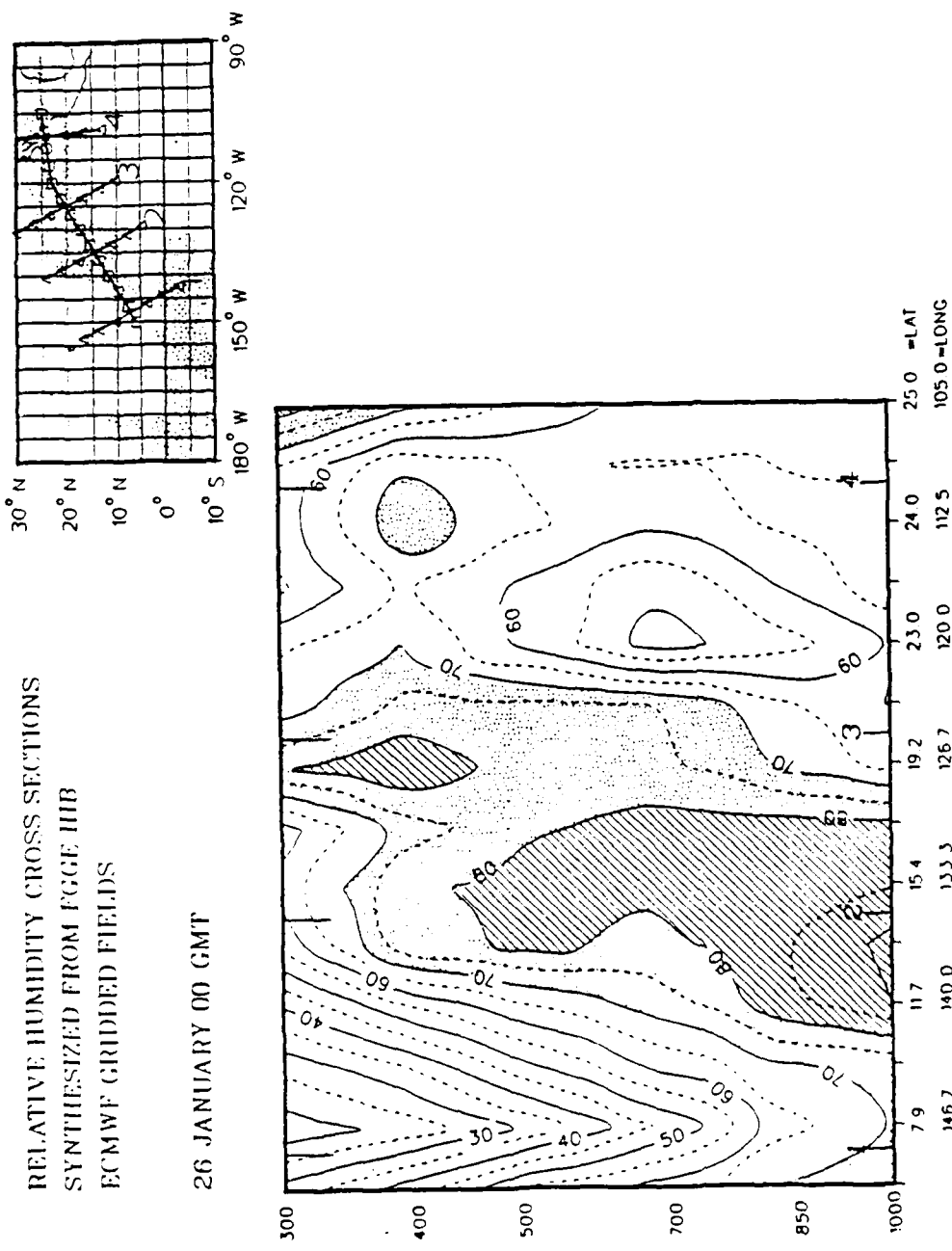


Fig. 69a. As in Fig. 61a except for 0000 GMT 26 January 1979.

PERPENDICULAR SECTION 2
CROSSING TRACK AT 135W PERPENDICULAR SECTION 3
CROSSING TRACK AT 125W PERPENDICULAR SECTION 4
CROSSING TRACK AT HOW

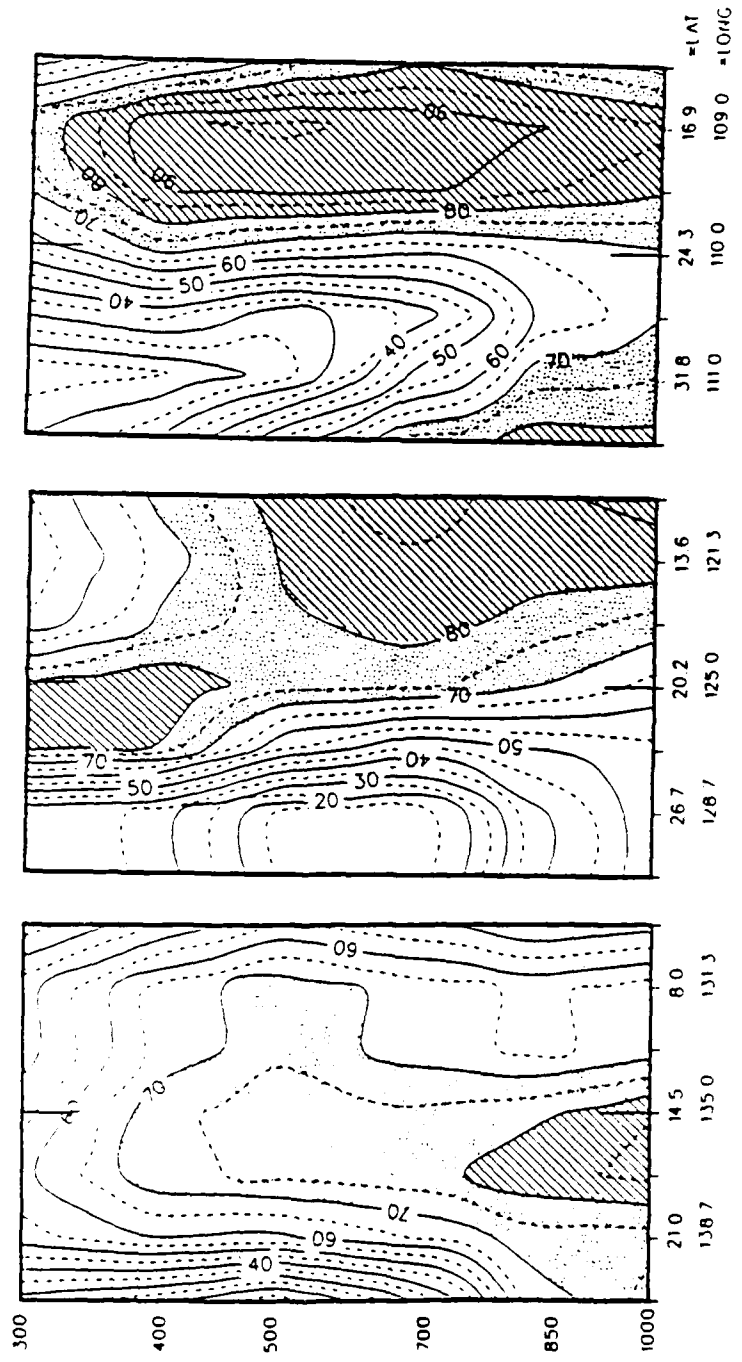


Fig. 69b. As in Fig. 61b except for 0000 GMT 26 January 1979. Note that only perpendiculars 2, 3 and 4 are shown.

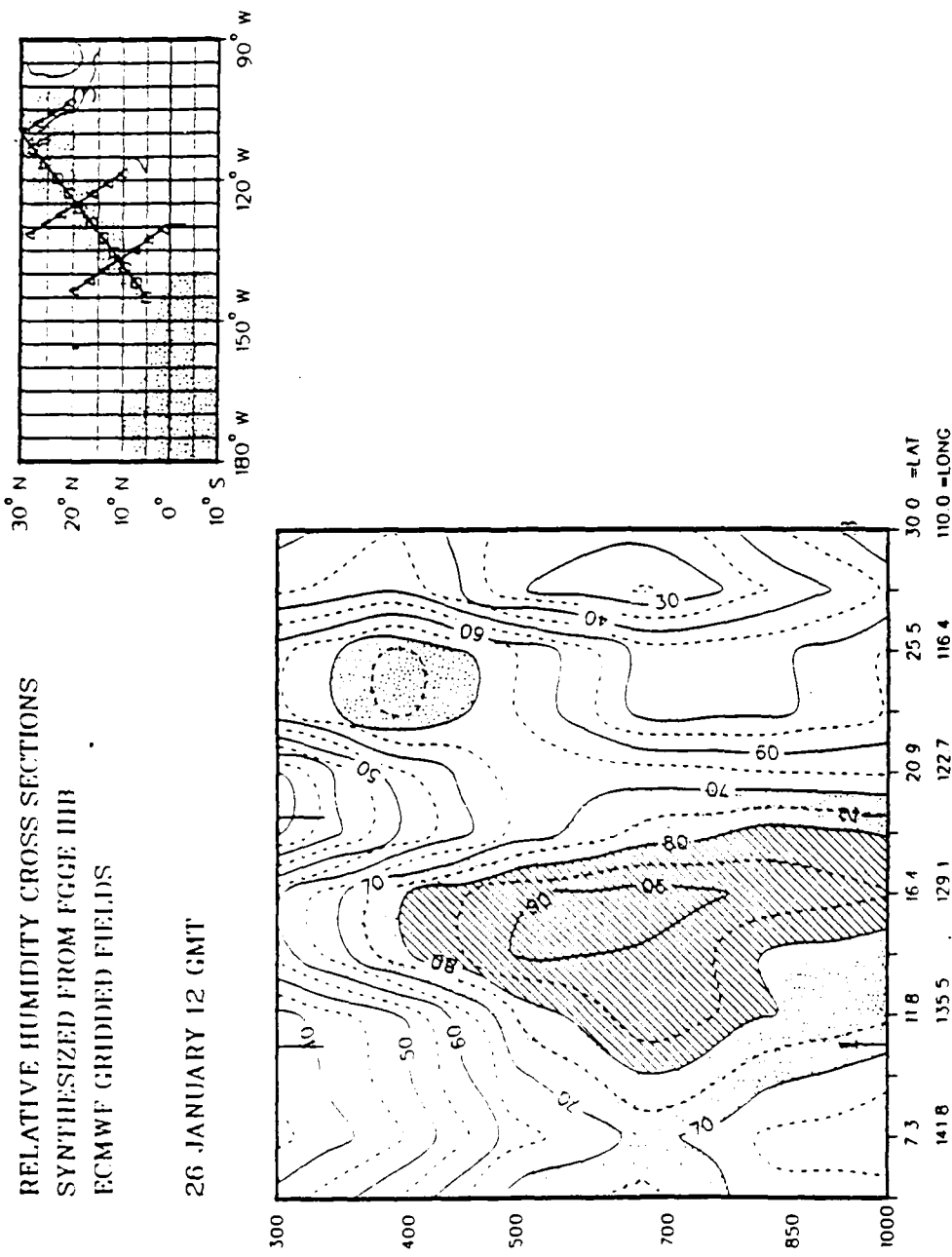


Fig. 70a. As in Fig. 61a except for 1200 GMT 26 January 1979.

PERPENDICULAR SECTION 1
CROSSING TRACK AT 137W
PERPENDICULAR SECTION 2
CROSSING TRACK AT 125W
PERPENDICULAR SECTION 3
CROSSING TRACK AT 110W

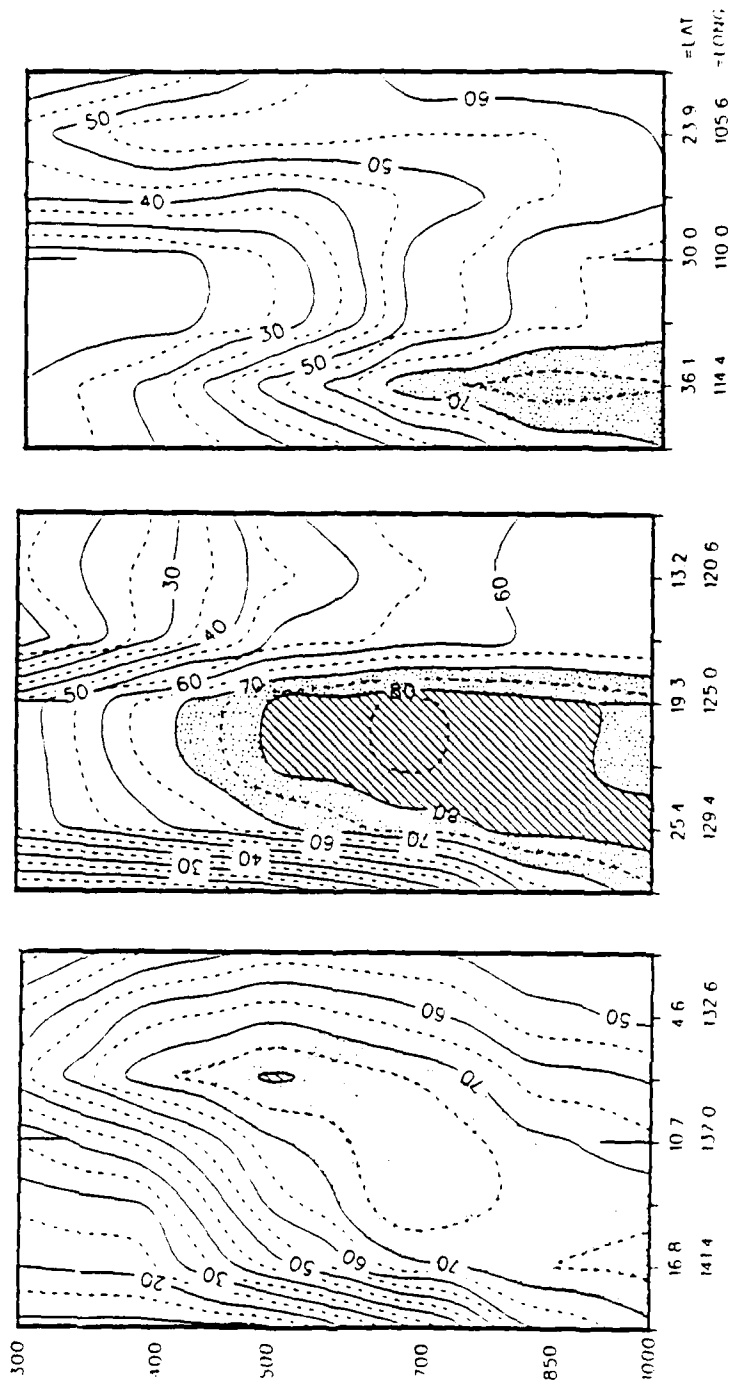


Fig. 70b. As in Fig. 61b except for 1200 GMT 26 January 1979.

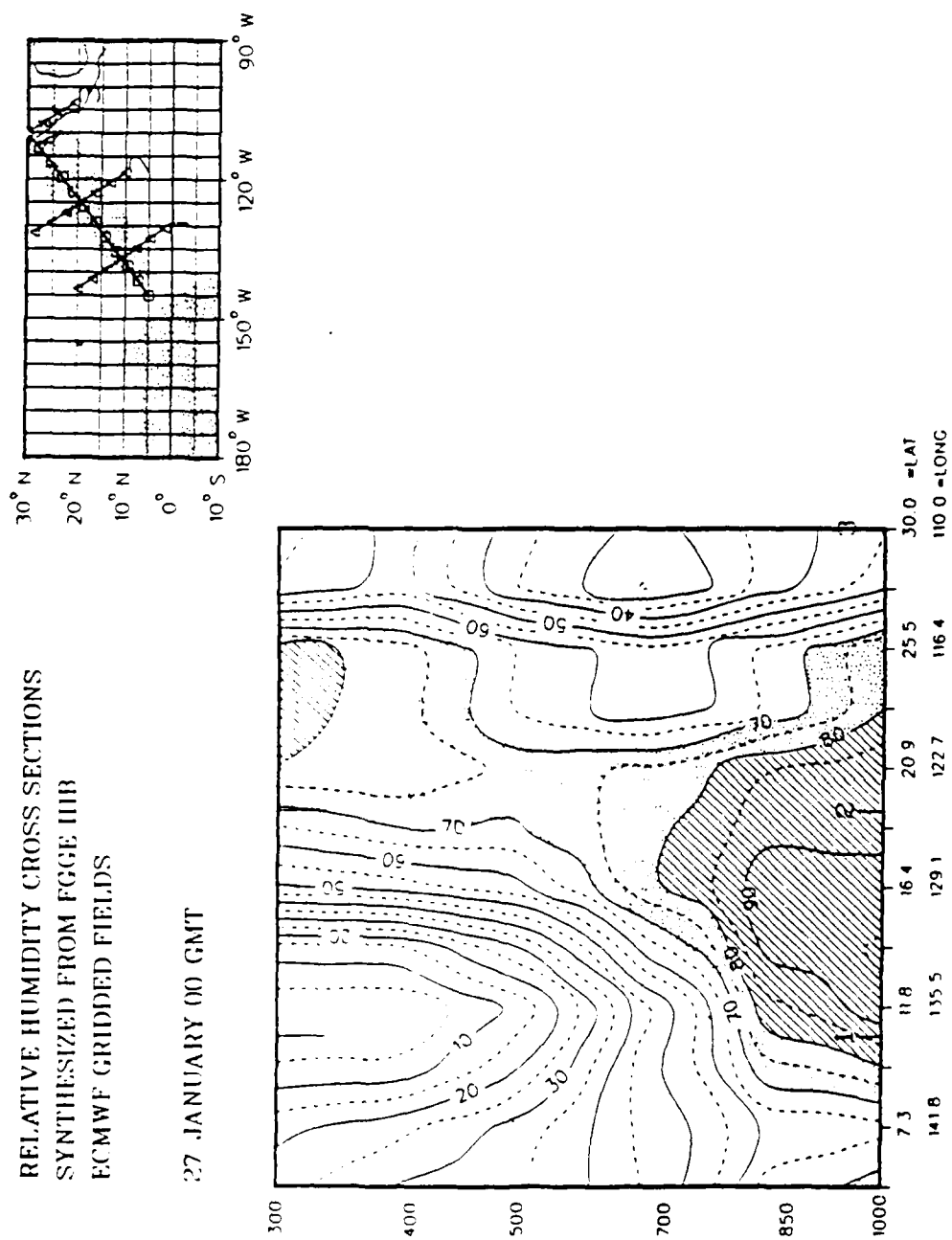


Fig. 71a. As in Fig. 61a except for 0000 GMT 27 January 1979.

PERPENDICULAR SECTION 3
CROSSING TRACK AT 110W

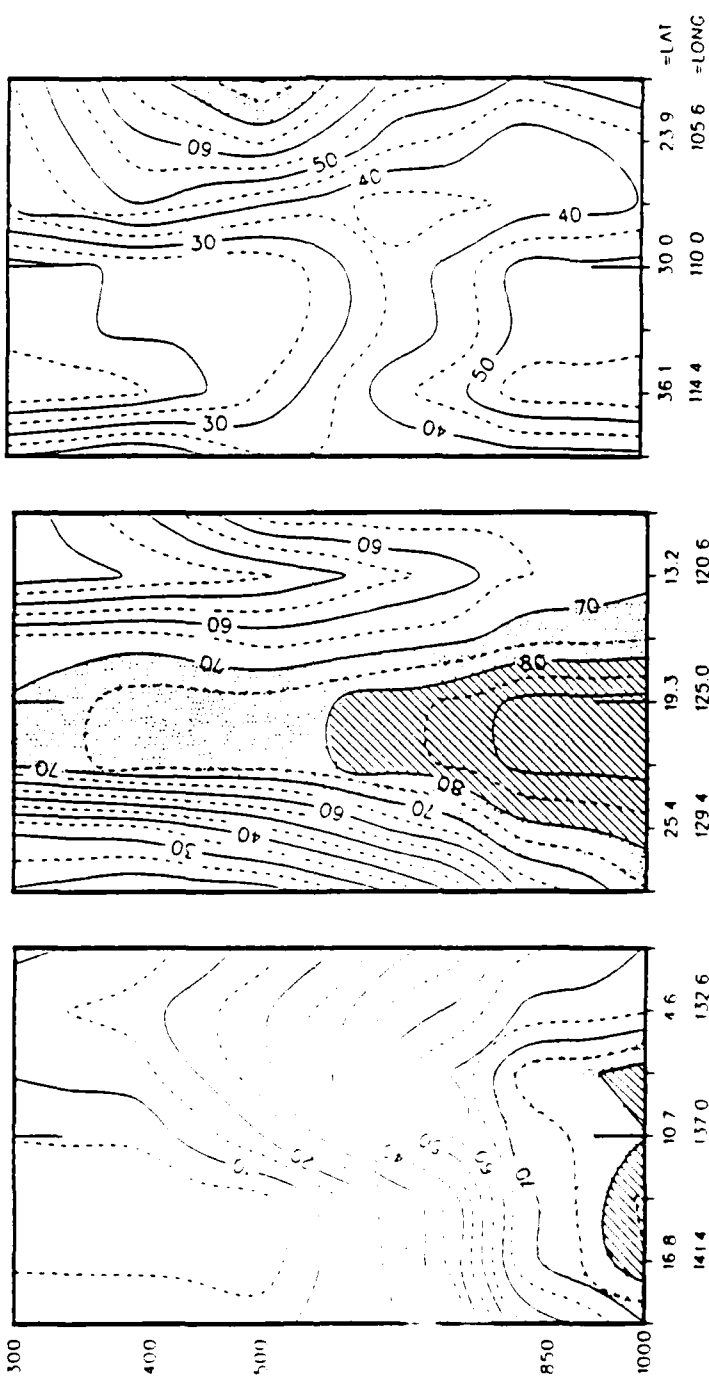


Fig. 71b. As in Fig. 61b except for 0000 GMT 27 January 1979.

The moisture burst narrows by 1200 GMT on the 27th, and the FGGE IIIb model reflects this narrowing (Figs. 72a and 72b). There is only low level moisture on the main track, and the perpendiculars show either little moisture or very small areas. Figs. 73a and 73b for 0000 GMT on the 28th show even less moisture in the region of the burst. There is an area of cloudiness at about $18^{\circ}\text{N}/132^{\circ}\text{W}$ that is shown to also be an area of FGGE IIIb moisture on perpendicular 3. This is possibly just coincidence, but if not, at least in this case the FGGE IIIb model did an excellent job of capturing the physical mechanisms responsible for this relatively small area of cloudiness.

In looking at the moisture depictions as a group using 70% RH as the cutoff point for clouds seems to succeed fairly well, at least as a coarse approximation. The FGGE IIIb model seems to capture realistic moisture patterns. Assuming that these mappings are representative, certain characteristics of the moisture burst become evident.

The first two days (Figs. 61-64) show that there are three reasonably distinct moist regions in the burst area which do not all combine until approximately 0000 GMT on the 23rd. The first two moist areas are both related to the ITCZ and are just to the southwest and southeast of origin area respectively. The third is just to the southeast of Hawaii at about $16^{\circ}\text{N}/150^{\circ}\text{W}$. This pattern indicates that at least a good portion of the third area is due to vertical motion rather than advection because if it were totally horizontal advection there would not be a drier area between. This third area is the region of rapid development of the first burst discussed in Section 4a on satellite interpretation. The second moisture burst also shows this separation of moisture from the ITCZ (Fig. 70a).

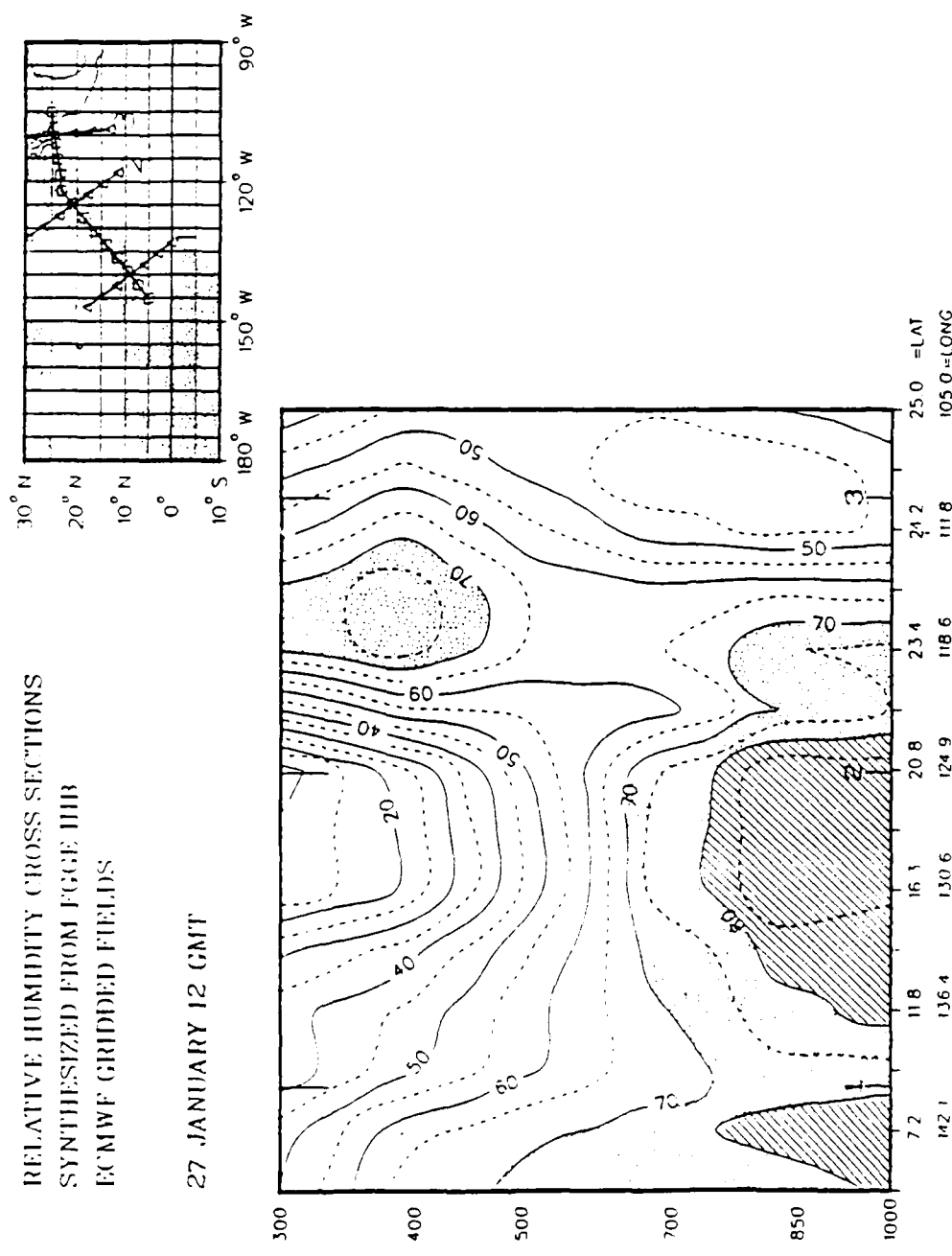


Fig. 72a. As in Fig. 61a except for 1200 GMT 27 January 1979.

PERPENDICULAR SECTION 1
CROSSING TRACK AT 140W

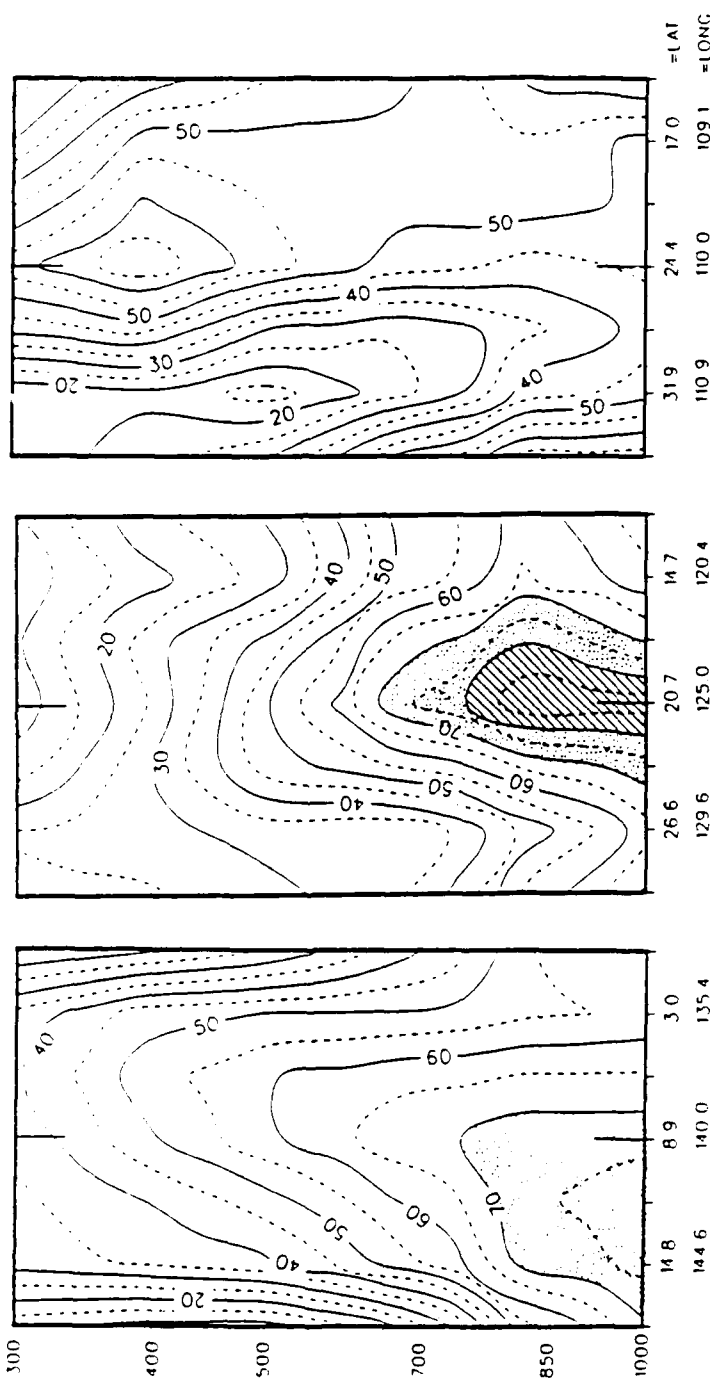


Fig. 72b. As in Fig. 61b except for 1200 GMT 27 January 1979.

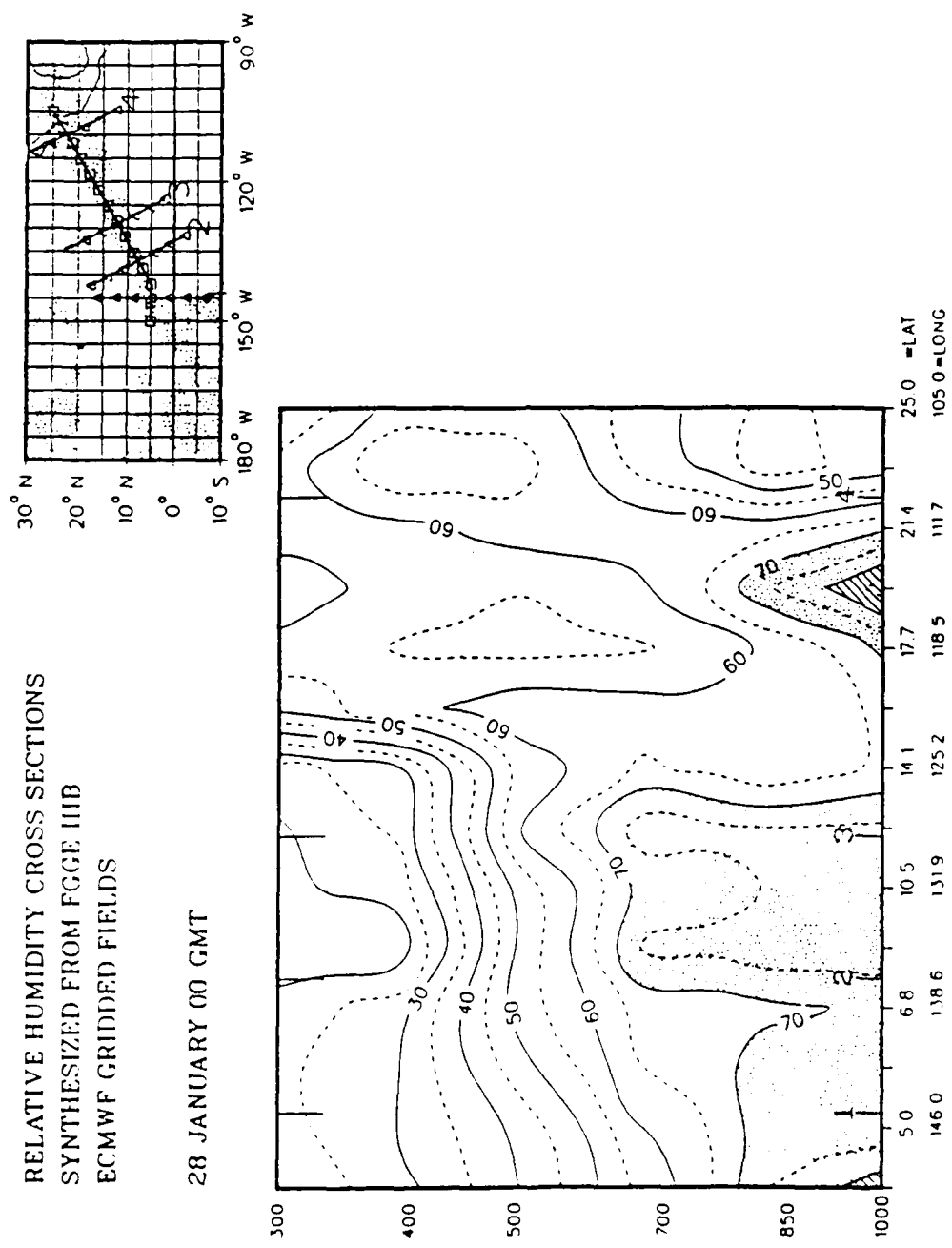


Fig. 73a. As in Fig. 61a except for 0000 GMT 28 January 1979.

PERPENDICULAR SECTION 1 PERPENDICULAR SECTION 2 PERPENDICULAR SECTION 3
CROSSING TRACK AT 145W CROSSING TRACK AT 137W CROSSING TRACK AT 129W

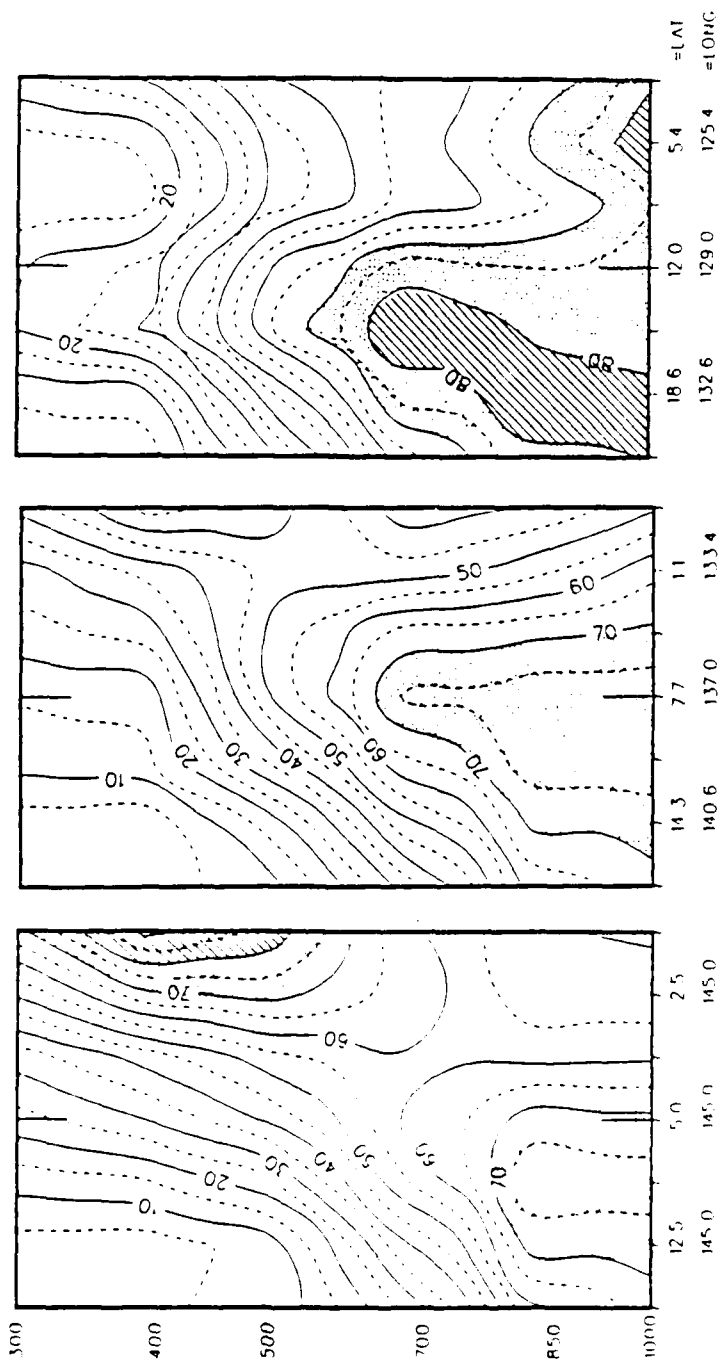


Fig. 73b. As in Fig. 61b except for 0000 GMT 28 January 1979.

Almost all of the perpendiculars, as expected, show much drier air just to the north and northwest of the main tracks. This drier air is also evident when the main track is slightly too far north. Figs. 69a and 69b show that the main track becomes fairly dry at A, but perpendiculars 3 and 4 show moisture just to the south of the main track.

There are relatively few moist areas that are confined strictly to the upper or middle levels. Fig. 63b shows two perpendiculars that extend into the area described in Section 4a as being mostly thin cirrus, yet the moisture is still shown as surface based rather than strictly upper-level moisture. Therefore detailed conclusions as to moisture depth may be dubious due to this seeming lack of cirrus-related moisture.

The northeastern portions of the tracks show generally drier air. The satellite photographs (see Section 4a) show these regions to be cloudy for most of the period. This feature, and the few instances of strictly upper level moisture, point to the FGGE IIIb model not handling advection of moisture well at levels other than the surface. Since the FGGE IIIb model does not contain any upper level moisture as input data, it also can not correct for moisture that is obviously present. Therefore if, say, the upper level jet is stronger than forecasted, and there is no wind information to correct the analysis, it may never reflect blowoff cirrus in an area.

Comparison of the two bursts shows that the second burst has less moisture than the first. This difference agrees with the satellite interpretation which showed that the second burst was considerably narrower than the first. Otherwise, the FGGE IIIb moisture patterns were fairly consistent.

e. Hawaii time sections

Satellite IR film loops revealed a weak cloud band that crossed the two Hawaiian radiosonde stations just prior to the rapid intensification of the first burst. To investigate this cloud structure, time sections for the two Hawaiian radiosonde stations were plotted and analyzed. The two stations are Hilo ($19.72^{\circ}\text{N}/155.09^{\circ}\text{W}$) and Lihue ($21.97^{\circ}\text{N}/159.37^{\circ}\text{W}$). Figs. 74 and 75 are the time sections of temperature, dew point depression, and equivalent potential temperature. Areas of dew point depression less than 5°C are stippled. Since the second moisture burst occurred so far east of Hawaii and no signal is evident in these cross sections, only the first four days of the time period are shown on the figures. Time sections of the winds are shown in Figs. 76 and 77.

Both of the temperature-time sections show features common in the tropics. Capping an area of moisture is a sometimes-discontinuous trade wind inversion at about 800 mb. The wind time sections show northeast trade winds dominating the lower atmosphere; as Riehl *et al.* (1951) and Holland and Rasmussen (1973) point out, the wind shift and inversion do not necessarily coincide. What the current data emphasize are features not commonly observed on a day-to-day basis. The most important is the inversion pattern and cold air at approximately 300 mb on the Lihue time section at 1200 GMT on the 20th. There is also a small moist pocket just below this inversion at about 350 mb. This moist area seems to correspond with the small cloud band seen moving over Hawaii on the satellite film loop and discussed in Section 4a of this study. This cloud band seems associated with a cold front emanating from a polar low well to the north. A similar inversion pattern moves over Hilo 12 h later. The moist area seen over Lihue is repeated over Hilo, although it is slightly drier than 5°C dew point depression, and is therefore not shown as a stippled area.

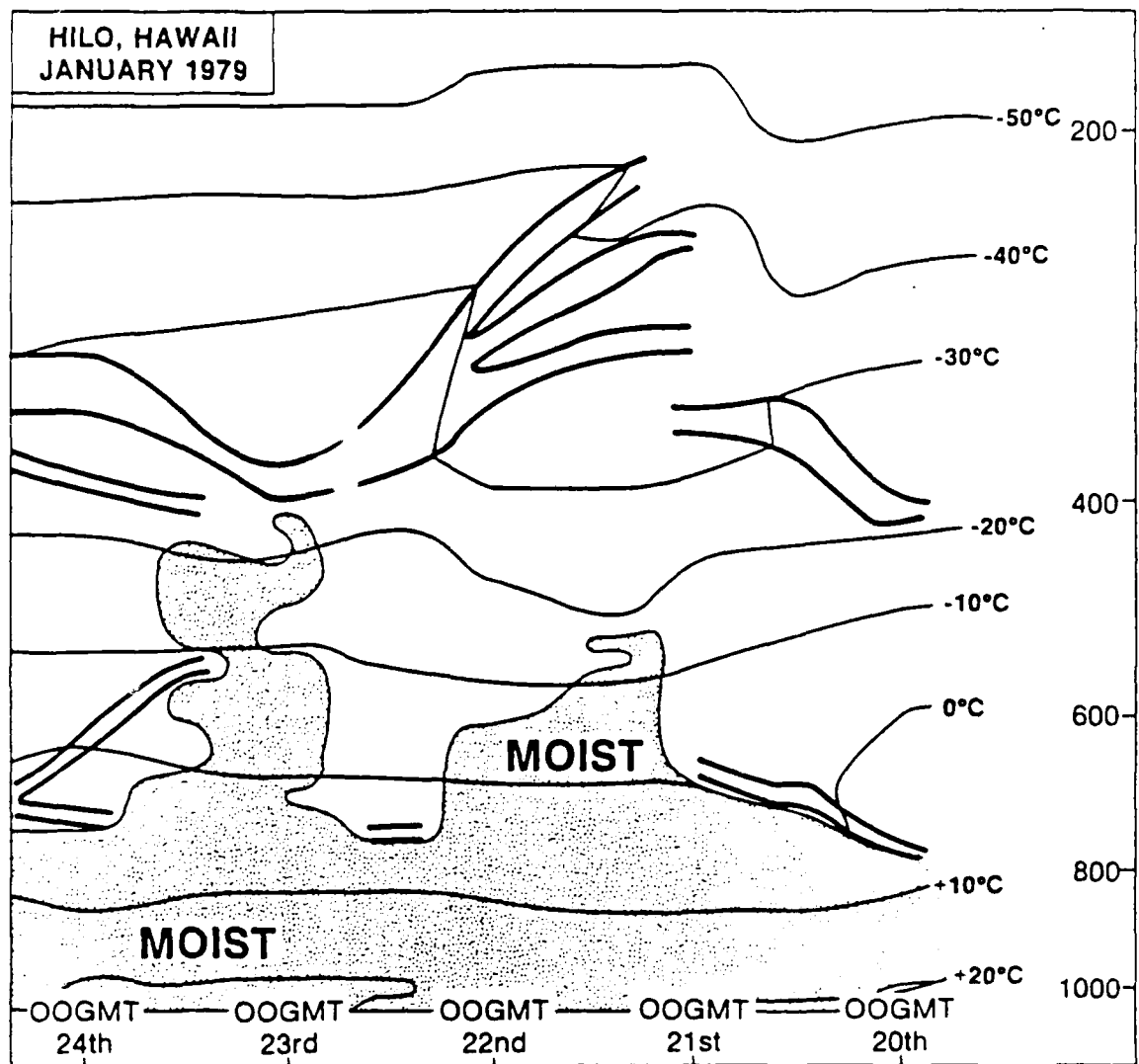


Fig. 74. Vertical time section for Hilo, Hawaii for the time period 0000 GMT 20 January to 0000 GMT 24 January 1979. Heavy lines are inversions and stable layers. Light lines are isotherms and areas of dew point depression less than 5°C are shaded.

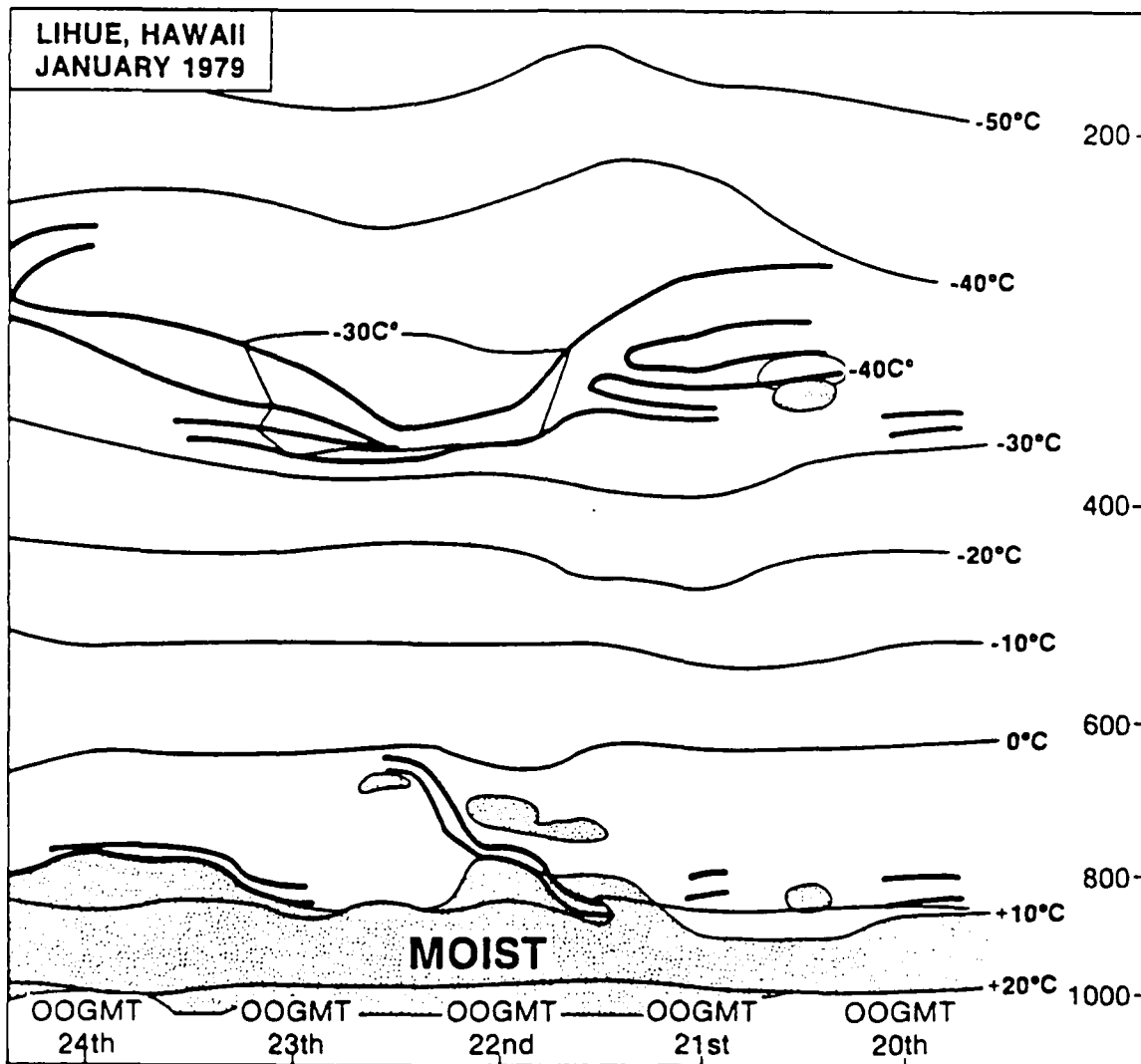


Fig. 75. As in Fig. 74 except for Lihue, Hawaii.

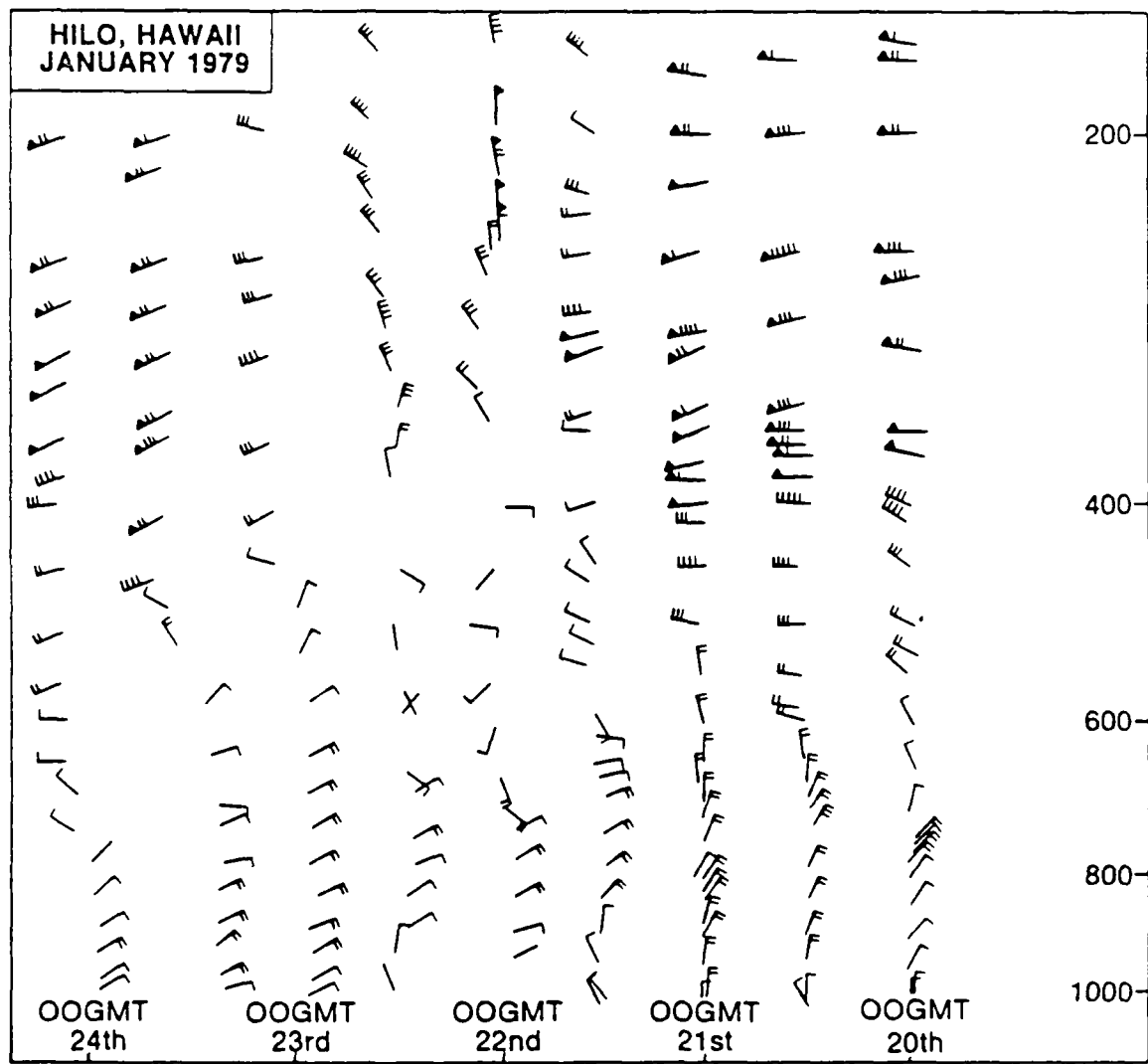


Fig. 76. Vertical time section for Hilo, Hawaii for 0000 GMT 20 January to 0000 GMT 24 January 1979. Full barbs represent 5 ms^{-1} and triangles represent 25 ms^{-1} .

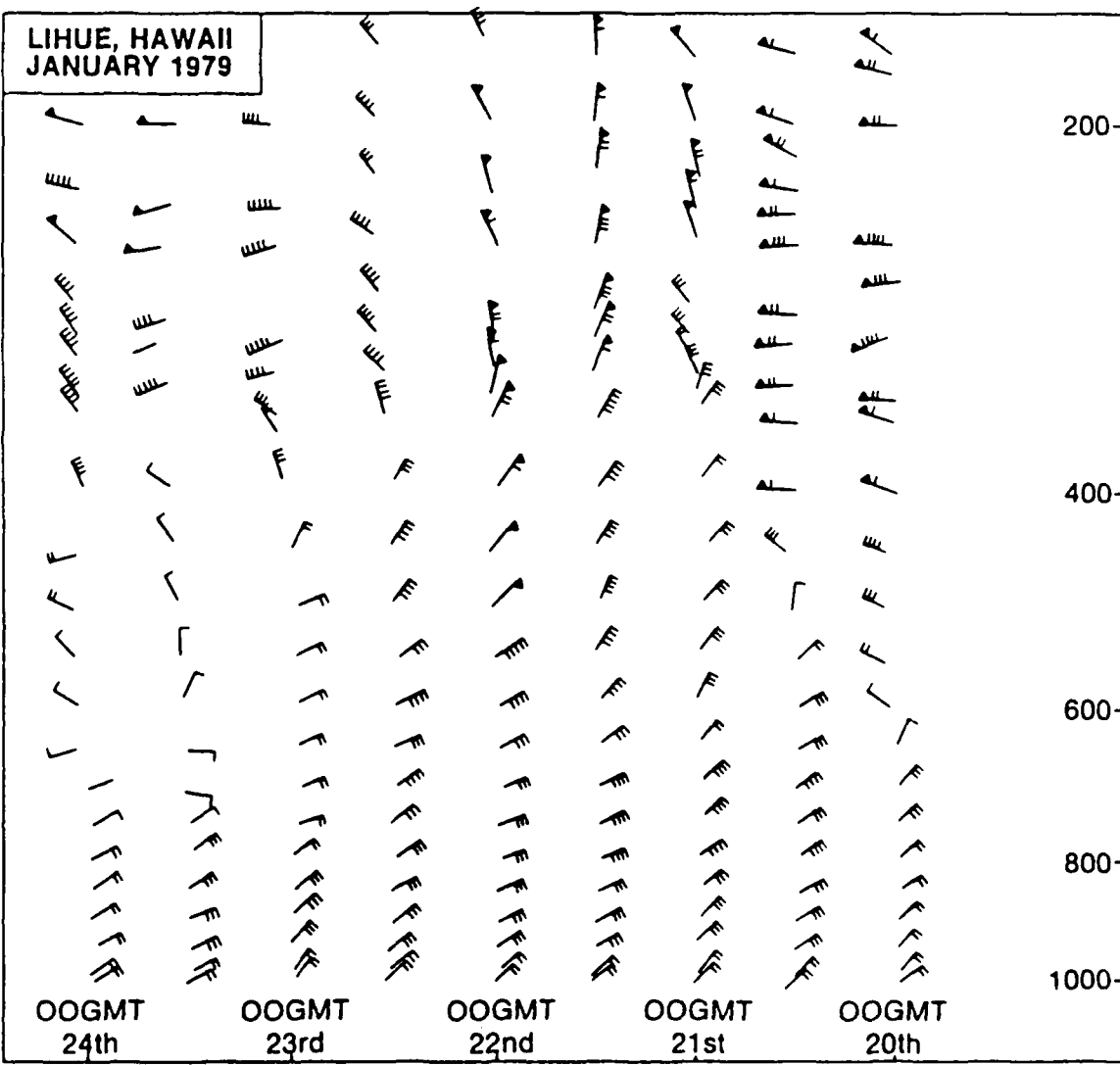


Fig. 77. As in Fig. 76 except for Lihue, Hawaii.

The cooling at Lihue near 300 mb is significant. At 320 mb the temperature cools by 8°C in the 12 h between 0000 GMT and 1200 GMT on the 20th; in the subsequent 12 h period, the temperature over Hilo cools by 7.2°C . During these same periods there is slight warming at both stations above 300 mb. By comparing the temperature time sections to the wind time sections it is found that the warming occurs above, and the cooling below, the level of maximum wind. This pattern is consistent with a cold front type phenomenon, although the cooling does not extend below 600 mb. The modification due to the warm ocean decreases any density difference across the front, and makes it difficult to detect a frontal pattern in the lower layers.

The theory of tropical cold fronts with extremely weak lower-level features has been known for some time. Atkinson (1971) refers to this phenomenon as a shear line, since there is no signal at the surface other than a possible wind shear. In this work it will be called a cold front, in that there is still cold air aloft associated with it. There is precedence for continuing to call it a cold front even after it is in the tropics (Henry, 1980).

The wind time sections show that above 600 mb there is a wind shift to northerlies behind the cold front. This wind shift is associated with the major trough crossing the Hawaiian islands as discussed in Section 4b.

It is interesting to note that, especially at Lihue, the height of the maximum wind is just above the height of the middle tropopause (the middle tropopause being the inversion around 300 mb (Byers, 1974; p 230)). This phenomenon agrees with the observation that jet streams are a tropopause phenomenon, and therefore the fluctuations in this inversion are related to, not only the upper-level cold fronts, but also to the subtropical jet stream.

After 0000 GMT on the 23rd. at both Lihue and Hilo, the winds become westerly once again as the trough moves eastward.

The only other significant event in the temperature time sections are the periods on the 22nd and 23rd when the low level moisture penetrates the trade wind inversion. This penetration is especially strong at Hilo on the 23rd. This seems to be due mainly to local convection as the satellite pictures and film loops show this convection virtually covering the islands but not anywhere else in the nearby region.

The upper level cold front if it continued to move southeast at the same speed would correspond with the area of rapid development of the cirrus discussed in Section 4a. Any further assumptions about the movement would be questionable. It weakened even between Lihue and Hilo and therefore it may have lost organization not long after passing over Hilo.

CHAPTER V

SYNTHESIS AND INTERPRETATION

To illustrate better the relationships between the various meteorological features previously discussed, schematic diagrams are drawn depicting the first few days of the first moisture burst.

The upper level panels show:

- 1) Clouds above 500 mb (as determined from color enhanced satellite photographs).
- 2) Areas of 500 mb FGGE IIIb RH greater than or equal to 70%.
- 3) 300 mb wind fields (FGGE IIIb winds, although adjusted to better reflect actual observations) which include streamlines, areas of wind speeds greater than or equal to 40 ms^{-1} , and associated trough lines.
- 4) Areas of 300 mb 12 h temperature change, showing cooling of 2°C or more.

The low level panels show:

- 1) Significant clouds at any level (due to inability to distinguish low cloud below the upper clouds).
- 2) Areas of 850 mb FGGE IIIb RH greater than or equal to 70%.
- 3) 850 mb wind fields as before, only without isotachs.

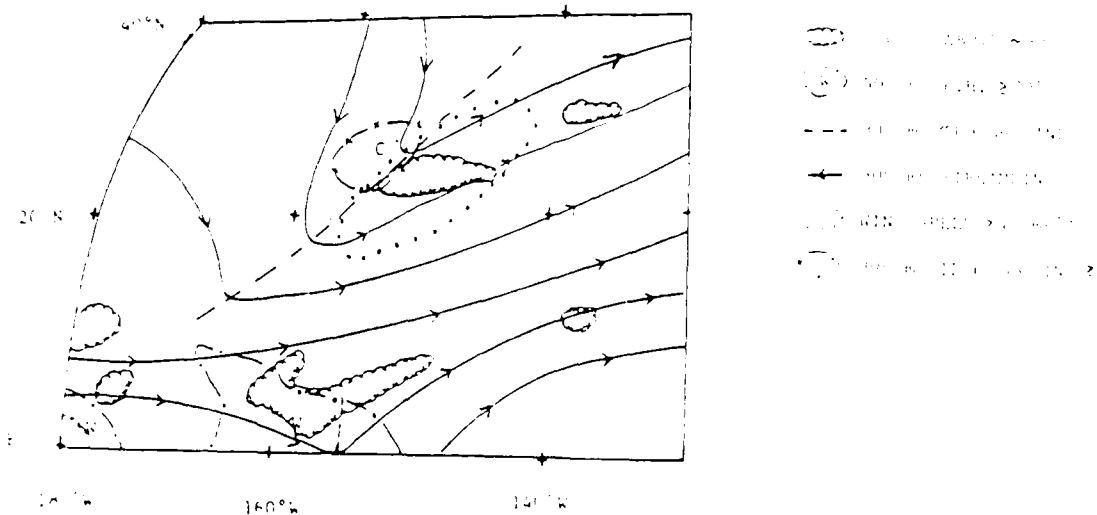
The major features of these drawings have been discussed previously in the individual sections. The overall significance is discussed further later in this section.

Fig. 78 shows the upper and lower levels for 0000 GMT on the 21st. The key features are:

- 1) The upper level trough with the area of cooling temperatures.

UPPER LEVEL

0000 GMT 21 January 1979



LOW LEVEL

0000 GMT 21 January 1979

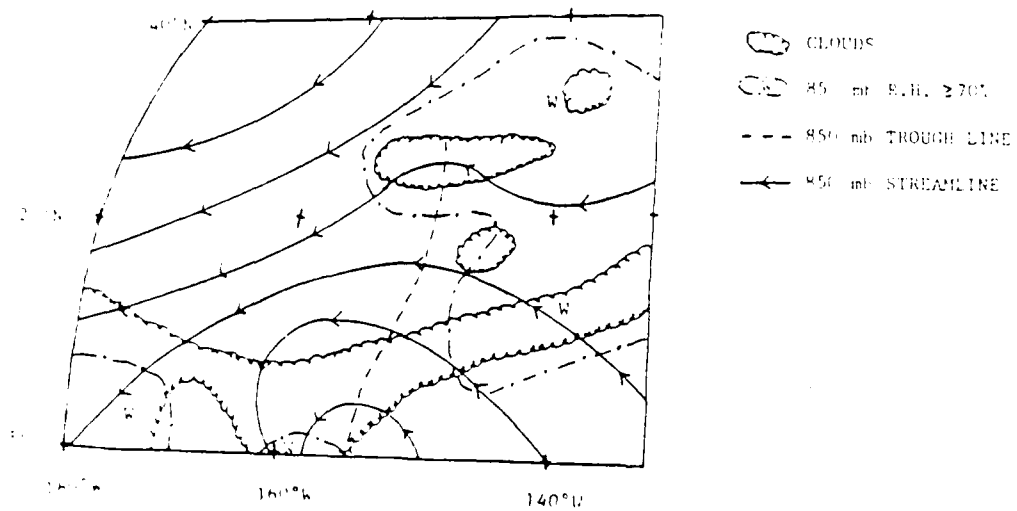


Fig. 78. Schematic depictions for upper and lower levels for 0000 GMT 21 January 1979. Note that upper level schematic extends farther east than low level schematic.

- 2) Wind speeds greater than 40 ms^{-1} on the east side of the trough.
- 3) The low level trough generally to the east of the upper trough, although in the northern portion it is directly below the upper trough in a cloudy region.
- 4) Significant low level moisture both along the equator and the eastern portion of the diagram.

Fig. 79 shows the two levels for 1200 GMT on the 21st.

The key features are:

- 1) Continuation and strengthening of the upper level trough.
- 2) An increasing area of strong winds aloft.
- 3) Upper level cooling covering a large part of the northern section of the burst.
- 4) An area of low level confluence within the burst associated with the trough.
- 5) A large area of low level moisture dominating the burst.

The drawings for 0000 GMT on the 22nd (Fig. 80) show:

- 1) The upper level trough extending to the equator with strong winds still on the east side.
- 2) A large meridional component to the upper level winds.
- 3) A low level trough in the center of the burst with a col point along the northern edge.

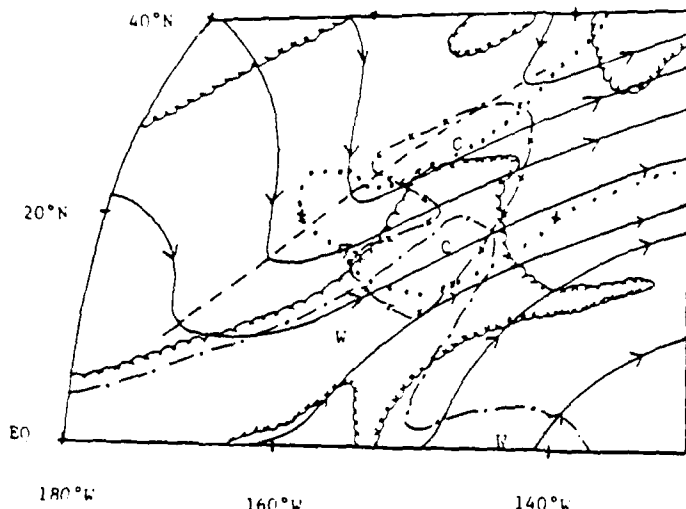
Fig. 81 for 1200 GMT on the 22nd shows:

- 1) Continuation of the strong upper level trough and wind speeds.
- 2) A new area of cooling moving in from the northwest.
- 3) A closed circulation in the low layer with a trough along the western edge of the burst.

Fig. 82 for 0000 GMT on the 23rd shows:

UPPER LEVEL

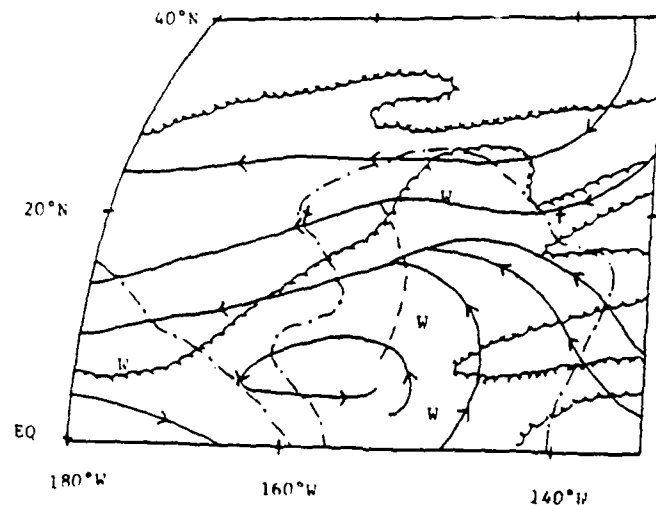
1200 GMT 21 January 1979



- CLOUDS ABOVE ~500 mb
- 500 mb R.H. $\geq 70\%$
- - - 300 mb TROUGH LINE
- ← 100 mb STREAMLINE
- WIND SPEED $\geq 40 \text{ ms}^{-1}$
- 300 mb 12 h COUNTING $\geq 2^\circ\text{C}$

LOW LEVEL

1200 GMT 21 January 1979

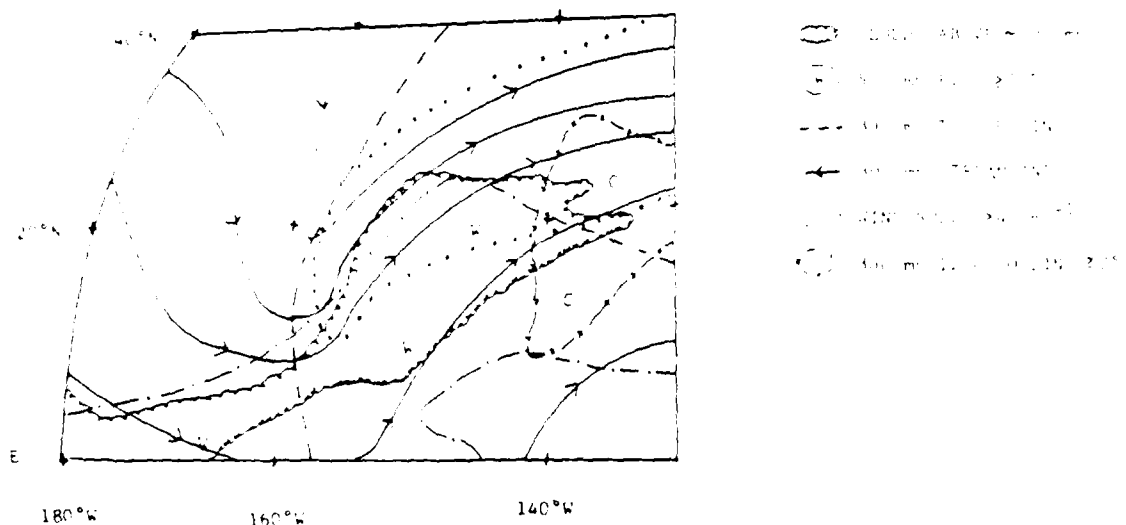


- CLOUDS
- 850 mb R.H. $\geq 70\%$
- - - 850 mb TROUGH LINE
- ← 850 mb STREAMLINE

Fig. 79. As in Fig. 78 except for 1200 GMT 21 January 1979.

UPPER LEVEL

0000 GMT 22 January 1979



LOW LEVEL

0000 GMT 22 January 1979

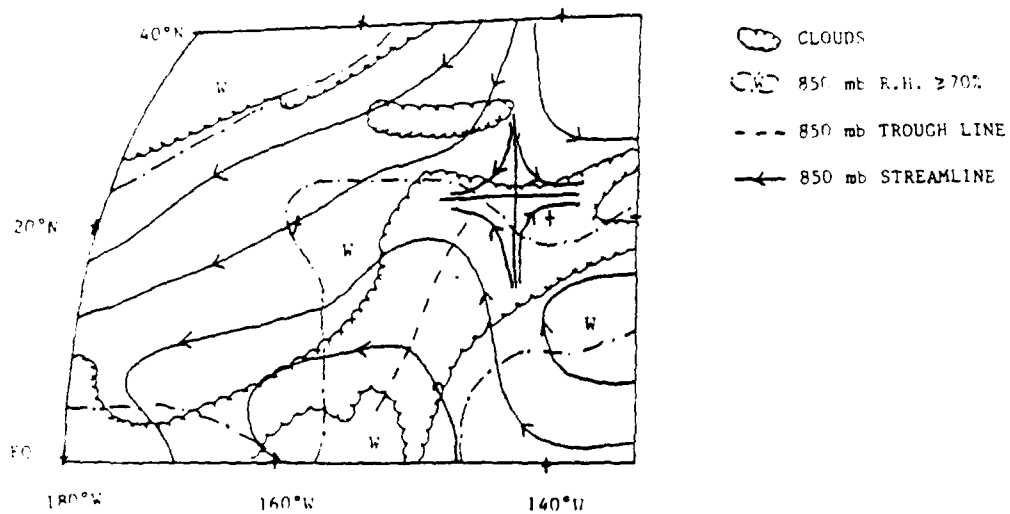
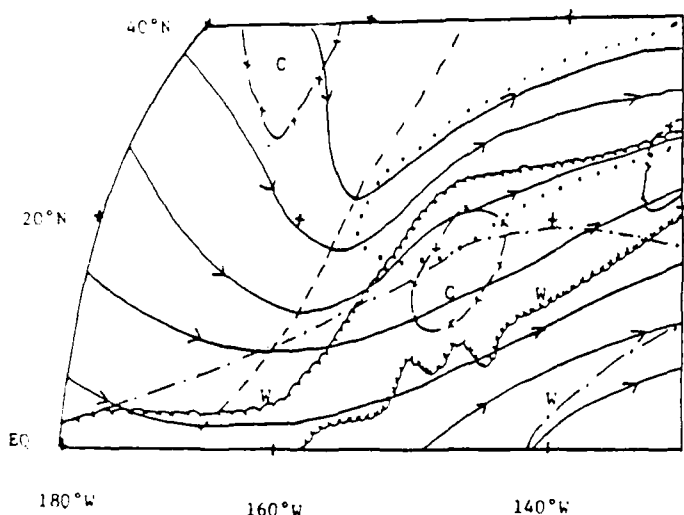


Fig. 80. As in Fig. 78 except for 0000 GMT 22 January 1979.

UPPER LEVEL

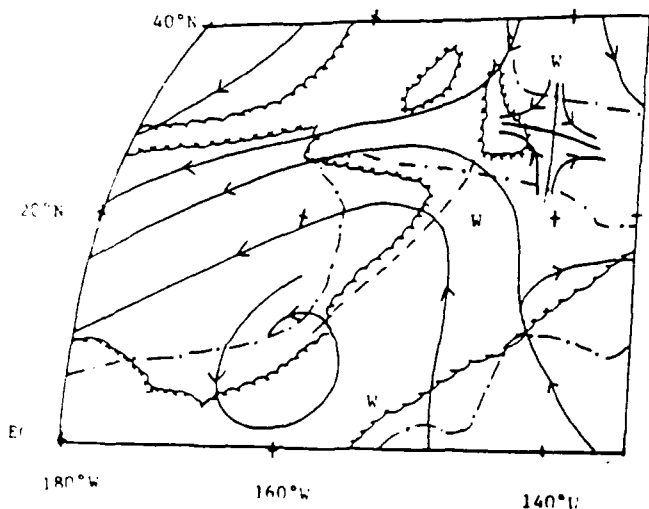
1200 GMT 22 January 1979



- CLOUDS ABOVE ~ 500 mb
- 500 mb R.H. $\geq 70\%$
- - - 300 mb TROUGH LINE
- ← 300 mb STREAMLINE
- ↑ WIND SPEED ≥ 40 ms^{-1}
- 300 mb 12 h COOLING $\geq 2^{\circ}C$

LOW LEVEL

1200 GMT 22 January 1979

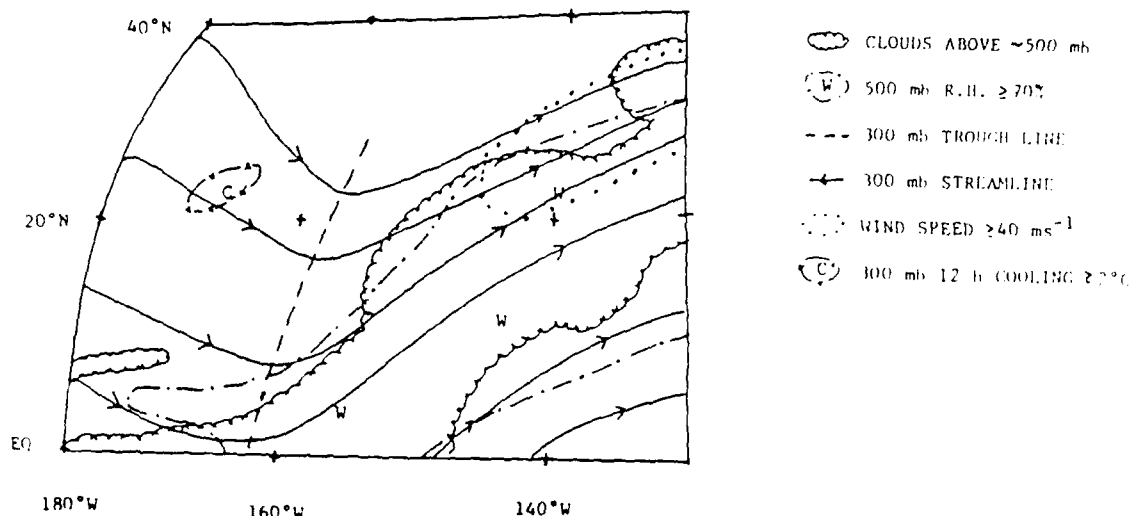


- CLOUDS
- 850 mb R.H. $\geq 70\%$
- - - 850 mb TROUGH LINE
- ← 850 mb STREAMLINE

Fig. 81. As in Fig. 78 except for 1200 GMT 22 January 1979.

UPPER LEVEL

0000 GMT 23 January 1979



LOW LEVEL

0000 GMT 23 January 1979

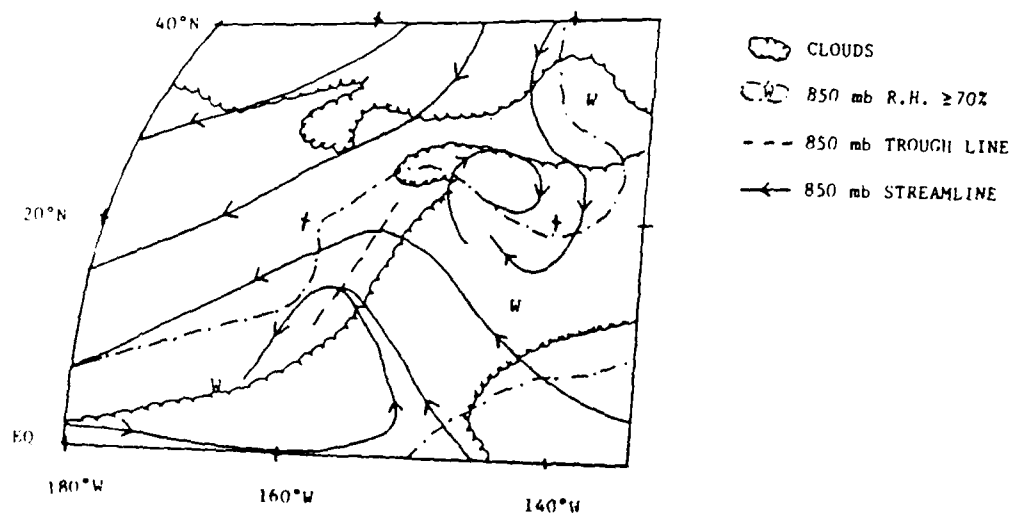


Fig. 82. As in Fig. 78 except for 0000 GMT 23 January 1979.

- 1) An upper level trough to the west of the burst.
- 2) The strong winds well east of the trough.
- 3) A small area of cooling still moving from the northwest.
- 4) A low level anticyclonic circulation feature at the northern edge of the burst.
- 5) A low level trough just to the west of the burst.

Smith et al. (1985) showed a climatological connection between upper-level troughs and moisture bursts. It has been shown that this same connection applies to the two bursts in this study. The analyses of FGGE IIIb winds, combined with the actual wind information (Section 4b) shows that, at the upper levels, a strong trough is associated with the first burst, and a weaker trough is linked to the second burst. The existence of these troughs associated with the first burst is also shown in the wind time sections for the two Hawaiian radiosonde stations (Section 4e).

Interpretation of the satellite photographs, both still and film loops, also shows the significant troughs associated with both of the moisture bursts. The sharp poleward edges of the upper-level clouds in the southeastern sector is indicative of a strong subtropical jet stream in the region of both bursts. The satellite photographs also point to a significant meridional wind component east of the trough axis in both cases.

The satellite film loops were the first step in further investigation of the nature of the troughs. The film loops, and associated still photographs, revealed a possible connection between the trough and a mid-latitude upper-level cold front (Section 4e). The satellite imagery shows a very weak broken cloud band along the forward edge of the upper-level trough continuing from the mid-latitude low to the tropics.

The Hawaiian radiosonde time sections showed a cold front in the upper levels, centered at about 300 mb, passing over the two Hawaiian stations (see Figs. 69 and 70). This temperature difference is also evident in the 300 mb 12 h temperature changes (Section 4c). The temperature change analyses show the cold front moving southeast from northwest of Hawaii and into the region of sudden burst development (Section 4a) at roughly the same time as the development. The time changes of temperature show a similar, although weaker pattern for the second burst as well.

It is likely that the FGGE IIIb wind analyses underestimate the wind speeds and meridional component of the subtropical jet stream in the region of the moisture burst. This underestimation is shown especially in the comparison of FGGE IIIb and IIb plotted winds (Section 4b). There is also an indication of this underestimation in the FGGE IIIb moisture depictions (Section 4d). The depictions show little upper-level advection of moisture in the northeast regions of the moisture bursts where advected cirrus are the dominant clouds during much of the period of the two bursts.

The FGGE IIIb model analyses, FGGE IIb data and satellite photographs all point to a strong subtropical jet stream all along the moisture bursts. They also show (especially the FGGE IIb data) a strong meridional component in the burst origin regions which becomes nearly zonal further to the northeast. In Section 4b it was shown that the jet stream speed increases as the moisture burst develops. Another possible reason for the increased jet stream speed is related to the decreased Coriolis parameter in the tropics. As the mid-latitude low pressure system moves southeast the unbalanced pressure gradient force could accelerate the winds roughly towards the lower pressure. As the jet stream winds move northward the conservation of angular momentum turns the winds eastward and maintains the high speed levels observed.

The increasing jet stream winds should result in upper-level divergence to the right of the jet in the entrance region (Whitney 1977). This increase is due to the positive vorticity advection to the right (equatorward) of the jet stream entrance region. In addition, the cold air aloft results in instability as the upper-level cold front passes. These factors point to significant vertical motion in the region of rapid development to the southeast of Hawaii and equatorward along the upwind side of the wind trough. Dynamically speaking, this region is also a region of favored upward vertical motion due to both vorticity and thermal advection.

The FGGE IIIb analysis contains probable upward vertical motion in the area to the northeast of the actual origin areas. In the first burst the FGGE IIIb moisture depictions (Figs. 68a and 68b) show a moist region (centered at approximately $16^{\circ}\text{N}/150^{\circ}\text{W}$) at least partially unconnected to the ITCZ and origin regions. This moist region is due probably to upward vertical motion in the model (and possibly the atmosphere) rather than pure advection since it is unconnected to the ITCZ.

Connecting all the analyses produces the impression that, while there are technically two moisture bursts during this time period, there may by only one major system producing them both. There are two moisture bursts only because the first burst weakens to the point of no longer being considered a burst by the strict burst definition. When the cloud band reintensifies, it becomes the second burst. There are currently no data available to check, but the possibility exists that the same upper-level cold front remains in the vicinity of the second burst (Section 4c).

It was planned to construct a composite schematic of both of the moisture bursts that occurred during this time period but the information for the second burst is even more sporadic than the first. The second burst does seem to show the same basic pattern as the first, only somewhat weaker. Intensity differences would seem to be due mostly to the relative intensities of the supporting synoptic patterns.

CHAPTER VI

CONCLUSIONS

It is impossible in a case study such as this to determine the weather elements that are necessary and sufficient for a particular phenomenon. What has been accomplished is an investigation into several parameters and mechanisms considered important in two moisture bursts.

A common element is a strong upper-level trough with significant northward meridional component east of the trough axis. The upper-level troughs indicate upward vertical velocity in the area that corresponds with the bursts. A low-level easterly wave type trough is found with the first burst and may have been present, but not proven, with the second burst.

It was shown that there is associated with the first burst (and possibly the second as well) an upper-level cold front. The exact role of the cold front was not found.

The FGGE IIIb model does not seem to generate the moisture burst merely as an extension of the ITCZ. The FGGE IIIb RH depictions show an area of high RH separate from the region of high RH associated with the ITCZ. This area expands and eventually connects with the ITCZ.

Further studies need to be accomplished to explain several of the questions that this study has raised, but not answered.

- 1) To understand more fully the moisture sources of the moisture burst, a moisture budget must be calculated and interpreted.
- 2) A calculation of the vorticity fields is needed to understand and confirm the vertical motions assumed to be present from the synoptic situation: this calculation should explain the observed jet accelerations.

3) A comparison of the FGGE IIIb RH depictions, with an improved FGGE III analysis, could confirm or deny the model vertical motion versus advection theories of this study. It is hoped that the new output will show more definitely areas of horizontal advection.

REFERENCES

- Anderson, R.H., J.P. Ashman, F. Bittner, G.H. Farr, E.W. Ferguson, V.J. Oliver, and A.H. Smith, 1969: Application of meteorological satellite data in analysis and forecasting. AWSTR 212, Scott Air Force Base, IL, 62225.
- _____, and V.J. Oliver, 1970: Some examples of the use of synchronous satellite pictures for studying changes in tropical cloudiness. Proceedings Symposium on Tropical Meteorology, Honolulu, Hawaii, June 2-11, 1970, E. XII 1-E. XII 6.
- Atkinson, G.D., 1971: Forecasters' Guide to Tropical Meteorology, AWS TR 240, Scott Air Force Base, IL, 62225.
- Byers, H.R., 1974: General Meteorology. McGraw-Hill, 461 pp.
- Davis, N.E., 1981: METEOSAT looks at the general circulation: III. Tropical-extratropical interaction. Weather, 36, 168-173.
- Fujita, T.T., K. Watanabe, and T. Izawa, 1969: Formation and structure of equatorial anticyclones caused by large-scale cross-equatorial flows determined by ATS-1 photographs. J. Appl. Meteor., 8, 649-667.
- Henry, W.K., 1980: Three late spring fronts in the Caribbean. Nat. Wea. Digest, 5, 18-24.
- Holland, J.Z., and E.M. Rasmusson, 1973: Measurements of the atmospheric mass, energy, and momentum budgets over a 500-kilometer square of tropical ocean. Mon. Wea. Rev., 101, 44-55.
- Hollingsworth, A., A.C. Lorenc, M.S. Tracton, K. Arpe, G. Cats, S. Uppala, and P. Kallberg, 1985: The response of numerical weather prediction systems to FGGE level IIb data. Part I: Analyses. Quart. J. Roy. Meteor. Soc., 111, 1-66.
- Huang, H., and D.G. Vincent, 1983: Major changes in circulation features over the South Pacific during FGGE, 10-27 January 1979. Mon. Wea. Rev., 111, 1611-1618.

- Julian, P.R.. 1980: Data assimilation for the FGGE tropical observing system. Seminar 1980 Data Assimilation Methods, ECMWF, Reading, U.K., Sept. 15-19, 1980, 375-398.
- _____, 1984: Objective analysis in the tropics: A proposed scheme. Mon. Wea. Rev., 112, 1752-1767.
- Kinenmonth, W.R.. 1981: Variability of rainfall over Northern Australia. Variations in the Global Water Budget, Eds. A. Street-Perrott, M. Beran, R. Ratcliffe, D. Reidel Publishing Co., 265-272.
- Lorenc, A.C., and R. Swinbank, 1984: On the accuracy of general circulation statistics calculated from FGGE data-A comparison of results from two sets of analyses. Quart. J. Roy. Meteor. Soc., 110, 915-942.
- McGuirk, J.P., A.H. Thompson, L.L. Anderson, Jr., and N.R. Smith, 1984: Reliability of circulation statistics over the tropical Pacific Ocean based on FGGE data. Proceedings, 8th Climate Diagnostics Workshop, Toronto, Oct. 12-16, 1983, 247-257.
- _____, and A.H. Thompson, 1984: Transient tropical disturbances within the Pacific Hadley Cell. Proceedings, 15th Technical Conference on Hurricanes and Tropical Meteorology, Amer. Meteor. Soc., Miami, FL, Jan. 9-13, 1984, 249-255.
- Phillips, N., L. McMillin, A. Gruber, and D. Wark, 1979: An evaluation of early operational temperature soundings from TIROS-N. Bull. Amer. Meteor. Soc., 60, 1188-1197.
- Riehl, H., T.C. Yeh, J.S. Malkus and N.E. LaSeur, 1951: The northeast trade of the Pacific Ocean. Quart. J. Roy. Meteor. Soc., 77, 598-626.
- Smith, N.R., A.H. Thompson and J.P. McGuirk, 1985: Moisture bursts over the tropical Pacific Ocean. Submitted to Mon. Wea. Rev.

- Staelin, D.H., A.L. Cassel, K.F. Kunzi, R.L. Pettyjohn, R.K.L. Pon, and P.W. Rosenkrany, 1975: Microwave atmospheric temperature sounding: effects of clouds on the Nimbus 5 satellite data. J. Atmos. Sci., 32, 1970-1976.
- Thepenier, R., and D. Cruette, 1981: Formation of cloud bands associated with the American subtropical jet stream and their interaction with mid-latitude synoptic disturbances reaching Europe. Mon. Wea. Rev., 109, 2209-2220.
- Thompson, A.H., J.P. McGuirk, L.L. Anderson Jr., and N.R. Smith, 1984: Analysis of tropical synoptic disturbances using satellite-derived soundings and radiance data from selected channels. Proceedings of the Conference of Satellite Meteorology-Remote Sensing and Applications, Amer. Met. Soc., Clearwater Beach, FL, June 25-29, 1984, 137-142.
- Vincent, D.G., 1982: Circulation features over the South Pacific during 10-18 January 1979. Mon. Wea. Rev., 110, 981-993.
- Whitney, L.F., Jr., 1977: Relationship of the subtropical jet stream to severe local storms. Mon. Wea. Rev., 105, 398-412.

VITA

James Royal Schaefer was born on 7 April 1954 in Racine Wisconsin to Mr. and Mrs. Royal W. Schaefer. He graduated in June 1972 from South Milwaukee High School. He graduated in August 1977 with a B.S. in Physics from University of Wisconsin at Eau Claire. After several jobs he joined the U.S. Air Force in March 1979 and after attending Officer Training School was commissioned in June 1979. He attended the University of Utah under the Air Force Institute of Technology, and received a B.S. in Meteorology in May 1980. He was then stationed at Barksdale Air Force Base Louisiana as a weather forecaster and weather staff officer.

He left Barksdale in August 1983 and since has been attending Texas A&M University under the Air Force Institute of Technology.

The authors permanent mailing address is;

510 Williams Ave.,

South Milwaukee, Wisconsin, 53172.

F

M

D

D

T

C

9

-

86